MULTIPLE THIN FILM SCINTILLATOR
DETECTION SYSTEM FOR THE IDENTIFICATION
AND ANALYSIS OF HEAVY IONS

BY

DAVID MIKO

ACKNOWLEDGMENTS

TABLE OF CONTENTS

iii

iv

MULTIPLE THIN FILM SCINTILLATOR
DETECTION SYSTEM FOR THE IDENTIFICATION
AND ANALYSIS OF HEAVY IONS

By

David Miko

August, 1997

Chairman: William Ellis
Cochaiman: Luis Muga
Major Department: Nuclear and Radiological Engineering

The scope of this work is the design, construction,
calibration, and testing of a multiple thin film detection
system. The fission fragments from the spontaneous fission
of ^{252}Cf are used as a source of energetic heavy ions. The
spectrum from this source yields a wide range of masses
(roughly 85 - 165 amu) and initial energies (60 - 120 MeV)
useful in the calibration and testing of the system. The
double-peaked distribution of the fission fragment also
provides a measure of system resolution through the spec-
trum's peak-to-valley ratio.

The light output of two types of scintillator films,
NE-102 and para-terphenyl, are compared. It is found that
the luminescence of NE-102 (which contains 2 - 3 % para-
terphenyl) is much higher than that of pure para-terphenyl.

The construction of the system entails the incorporation of the electronics into a PC-based data acquisition system. The various parameters are acquired, digitized, and stored on the PC hard drive for future analysis.

Initially, the primary parameters (luminescence, time-of-flight, and residual energy) are calibrated. Then, empirical relationships between them are determined. All this information is then used to develop a procedure for the determination of the fission fragment nuclear charge (Z), yielding an overall charge resolution of 2.1 charge units. This differs from previous work in that nuclear charge is determined, as opposed to particle mass.

Finally, the system is used to investigate the charge state of fission fragments passing through a conductor (nickel foil) vs. an insulator (plastic film). The luminescence output of the thin film scintillators is dependent on the charge state of the ion. Therefore, by comparing particles of the same nuclear charge and energy entering the scintillator, a difference in luminescence indicates a difference in charge state. The scintillator light output is higher from the ions after passing through the plastic than the nickel. This is evidence of a higher ionic charge state in the ions after passing through the plastic.

CHAPTER 1

BACKGROUND

The multiple thin film scintillator detection system is a compact, inexpensive, and easily manufactured system for the measurement of charged particles. The ability of this setup for the identification of nuclear charge is determined. The utility of the detector system is then proven by finding a difference in charge state after particles pass through different media.

This section will investigate various types of charged particle detectors. Then, previous work on thin film scintillator detectors will be examined. Finally, systems utilizing thin film scintillators will be examined.

Charged Particle Detectors

Various methods have been used for the detection of high energy charged nuclei. Among these are track detectors, gas ionization detectors, solid state detectors, secondary electron emission detectors, and scintillation detectors. A brief description of each of these systems will be presented in the following pages.

Track Detectors

The principal method of track detection uses nuclear photographic emulsion. In this method, an emulsion of silver halide grains, suspended in a gelatinous matrix, is sensitized by the passage of ionizing radiation [1]. These sensitized grains remain until they are converted to metallic silver in the developing process. After developing, the remaining silver halide grains are dissolved away and then the entire film is washed to remove the processing solution. What remains is metallic silver showing a permanent record of the radiation interaction paths. The length and density of the paths give particle range and dE/dx information which can be correlated to known data to yield particle type and energy [2].

Advantages of this method are that no associated electronic equipment is needed, a permanent record of the tracks exist, and various emulsions can be used to fit certain requirements. Disadvantages are that the film must be examined carefully under a microscope, a tedious and time-consuming process. In addition, the film is sensitive to light and must be kept under dark-room conditions until developed. Also, heat and prolonged exposure to air can cause some deterioration. Finally, it is not always possible to resolve particles close in mass or charge, and there is no record of the time of the interaction.

One application for nuclear emulsion is for long-term satellite or high-altitude balloon measurements of cosmic-ray fluence, an integration detector.

Another type of track detector is the etchable solid state nuclear track detector (SSNTD) [3]. Heavily ionizing particles passing through crystals leave a trail of damage in the lattice structure roughly 3 - 10 nm in diameter. Certain reagents dissolve these regions at a much faster rate than the undamaged lattice. Continued etching will increase the diameter of the hole until it is visible under a microscope.

In order to create sufficient ionization resulting in lattice damage, a threshold atomic charge of about $Z = 20$ is required. As a result, SSNTD's have only specialized applications. One example would be the detection of heavy ions in an environment of high background of light ions or gamma radiation.

Gas Ionization Detectors

Ionization chambers operate by collecting the charged particles created by the interaction of radiation with the gas medium. An applied field in the detector volume attracts the electrons and ionized gas particles to the anode and cathode, respectively. If the electric field is high enough electron-ion recombination is negligible, and virtually all the charge is collected at the electrodes. By

increasing the electric field, charge multiplication occurs around the anode, with the resulting signal being proportional to the initial, or primary, ionization. A detector in this mode is called a proportional counter. However, some energy resolution is lost in the multiplication process.

Gas ionization detectors can operate as dE/dx detectors by simply having anodes smaller than the path length of the incoming ions and collimating the ions so that they travel parallel to the anode. As a result, the energy loss per anode length is measured. The residual energy can be determined either by a separate detector (e.g. solid state) or by having another anode long enough so that the particles stop within its length. An example of this second type is described below.

A 500 mm long chamber is positioned so that the heavy ion beam is collimated down the central axis of the detector. The gas pressure in the chamber is varied so that all the particles are stopped within the system. Three anodes are located along the path of the particles. The first two are each 100 mm in length, while the third is 300 mm. In this way, the first two are ΔE detectors while the third is an E_r detector [4].

A common gas chamber with heavy ion applications is the multi-wire proportional counter. In this system, wire anodes are placed parallel to each other in a planar geometry, usually only a few mm apart. In this geometry,

the system is a position detector, with its positional resolution determined by the distance between anodes. These detectors are utilized in determining the particle's direction, which is very important in large systems where the incident particles do not necessarily travel parallel to the anode. Some detectors increase the positional resolution along the direction of the anode by measuring the charge collected on each end. The position of the interaction is proportional to the ratio of the charge collected on either side to the total charge collected.

An ionization chamber may serve as a good general purpose heavy ion detector. It can be made much larger than any of the other systems to cover a greater solid angle. The energy resolution is good and these detectors do not exhibit a degradation due to radiation damage. Since the charge collection time is dependent on the drift velocity of the electron (typically 10^4 - 10^5 m/s), these detectors tend to be slow in response and have poor time resolution. Also, to avoid a buildup of positive charge, the positive ions should be collected before another particle interacts. Since the ion drift velocity is around 1/1000 that of the electron, this will severely limit the count rate that can be achieved with good energy resolution.

Semiconductor Detectors

Semiconductor detectors have become widely used in heavy ion research because of their combination of fast timing and good energy resolution. There are a wide variety of solid state detectors; however, they all work on the same principles. The charge produced in a semiconductor by ionizing radiation exciting electrons into the conduction band and creating holes in the valence band, is collected.

In a semiconductor, there is an intrinsic number of "free" charges, conduction band electrons and valence band holes. Ionizing radiation passing through semiconductors will create electron-hole pairs. By applying a voltage across the electrodes, the charge in the semiconductor can be collected. If the charge produced from the ionizing radiation is much larger than the intrinsic charge, a signal with good resolution can be obtained. In order to reduce the intrinsic charge (and increase the resolution), the semiconductor should be operated at very low temperatures. An example of this is the high purity germanium detector.

Also, regions within these materials can be made with an excess of electrons or holes by doping with an n-type or a p-type material, respectively. Semiconductor materials are classified as n or p-type according to whether their excess impurities are electron donors or acceptors. Donor impurities, such as valence 5 atoms, residing in the crystal lattice structure of valence 4 silicon have an excess

electron that can easily be ionized into the conduction band
as a "free" electron. This leaves behind a "positive" fixed
lattice site. Acceptor impurities, such as valence 3 atoms
in a silicon lattice, readily capture an electron from the
lattice. This results in a "negative" fixed lattice site
while producing a mobile "positive hole" that can move
freely throughout the lattice until it can recombine with a
free electron. Examples of n and p-type dopants are
phosphorous and boron, respectively.

Along boundaries of n-type and p-type regions,
diffusion across the boundary of free electrons and holes
results in recombination and charge neutralization.
Electrons are absorbed in the p-type material and holes are
absorbed in the n-type material. As a result, there is a
fixed negative charge in the p-side, and a fixed positive
charge in the n-side. These species comprise a positive and
negative space charge thereby constituting a voltage
difference across the junction, or an electric field within
the junction region. As a result, in this region there are
very few free charges that have not recombined. This area
is called the depletion region. This is a way of reducing
the intrinsic charge in the region. This process is shown
in the Figure 1-1 [1].

A positive hole produced within the depletion region
will move toward the negatively charged p-side while the
electron will move toward the positive charge of the n-side.
By applying a potential with the positive electrode attached

to the n-side, the depletion region is widened, and charge collection is enhanced. Ionizing radiation passing through this region will create electron-hole pairs that are then collected. Integration of this charge across the output impedance yields a signal proportional to the amount of energy lost in the depletion region. For surface-barrier detectors, the depletion region extends to the surface of the semiconductor. Thus, the ionizing particle must only pass through the thin electrode before interacting with the depletion region.

Since only about 3 eV are required to produce an electron-hole pair in a semiconductor and roughly 30 eV are required in gas, energy peak resolution, defined as the full-width-at-half-maximum (FWHM) is generally much better with semiconductors, and given by:

$$FWHM = \sqrt{\epsilon E F}$$

ϵ = Average energy to create electron/hole pair.
E = Particle energy
F = Fano factor

Since ϵ(semiconductor) = 1/10 * ϵ(ion chamber), and
    F(semiconductor) = 1/2 * F(ion chamber),
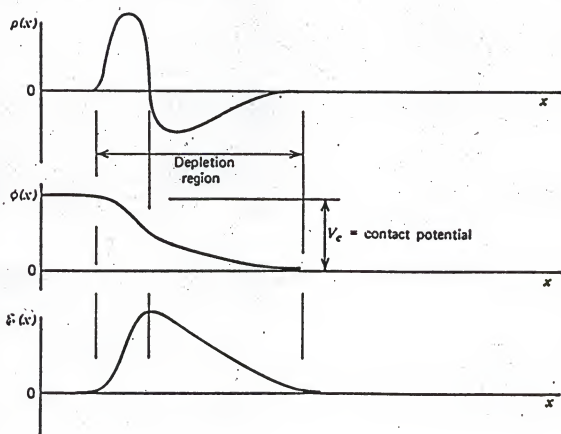
Figure 1-1: Effects of carrier diffusion at an n-p junction.
Top: Space charge plot. Middle: Potential field.
Bottom: Electric field [1].

the FWHM should be roughly the square root of 20 better than that of an ion chamber. Also, the signal collection time is much shorter for semiconductors, than gas systems, yielding better time resolution. This is due to much shorter distance (typically less than 0.1 mm) that the ions and electrons travel before collection. However, solid state detectors are prone to radiation damage resulting in long term deterioration. Ionizing radiation damages the localized lattice structure of the semiconductor crystal. This damage results in defects that can trap holes or electrons, thus reducing the collection efficiency. This results in deterioration after long-term exposure to radiation. This effect can be reduced by an annealing process. In addition, semiconductors contain a "dead" layer at the surface where incomplete charge collection takes place. This is caused by the particle having to pass through the electrode on the surface of the semiconductor and also surface effects. This results in an energy loss that does not contribute to the signal.

The two principal types of solid state detectors with heavy ion applications are totally depleted detectors and surface barrier detectors (SBD). These are used as transmission detectors and residual energy detectors, respectively.

For totally depleted detectors, the applied voltage is high enough so that the entire semiconductor becomes depleted. If they are made thin enough, the particles will

pass through the semiconductor and a dE/dx signal will result. These solid state detectors are commercially available in 50 - 1000 μm thicknesses. However, when these are used as transmission detectors, dead layers on both the front and back sides must be taken into account. Typically, these layers are less than 100 nm [1].

With surface barrier detectors, the dead layer is made as thin as possible to minimize the energy lost in this region. This is usually done by etching the surface, controlled oxidation followed by evaporation of a thin gold (or other metal) layer for protection of the surface and electrical contact [1]. The dead layers are less than 100 nm thick. The depletion region is thick enough so that all the particles are stopped within this zone. The thickness can be controlled by the applied bias, as shown in the nomogram in Figure 1-2 [5]. For a specific resistance of 4500 ohm-cm (n-type), to achieve a depletion layer of 300 μm, a bias of 65 volts must be used. This thickness would be sufficient to stop a 23 MeV alpha particle, 5.9 MeV proton, or a 0.25 MeV electron. For the current work, the SBD is n-type of nominal resistivity of 468 ohm-cm. The applied voltage is 34 V. Connecting these points yields a depletion layer of 70 um, or thick enough to stop a 10 MeV alpha particle.
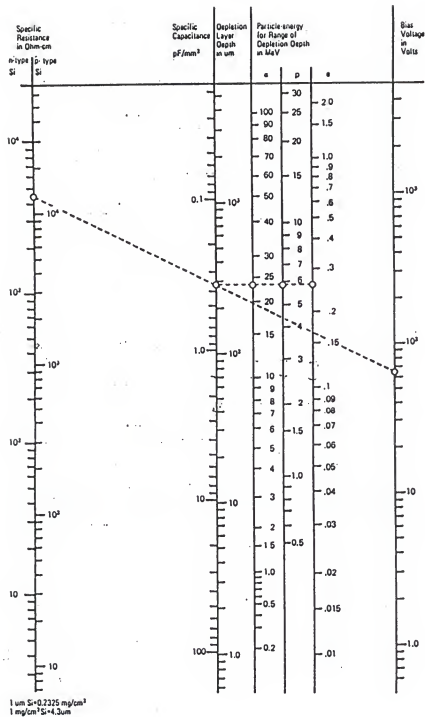
Figure 1-2: Nomogram for a silicon surface-barrier detector [5].

Secondary Electron Emission Detector

Secondary electron emission occurs when an ion passing through matter causes electrons to be ejected from the material. If this material consists of a very thin foil (usually carbon), the electrons emitted near the back of the foil will escape and can be detected. The detectors based on this process tend to have excellent time resolution (100's of ps) and are used principally as start or stop detectors, that is there signal is used to start or stop a time-of-flight measurement. However, they do not give off enough electrons to be of much use in energy or particle measurements.

Because typically only 10 - 100 electrons will be emitted from the foil, it is necessary to collect as many as possible in order to register an event. The emitted electrons can be collected in a number of ways. The most common method is through the use of microchannel plates (MCP). MCPs consist of an array of very small tubes (10 - 100 μm in diameter) about 1 mm long. Each MCP acts as an independent electron multiplier. A potential of about 1 kV is maintained between the two ends. When an electron enters the MCP, avalanching occurs, and the resulting multiplication factor is roughly 10^4 [6].

Scintillation Detectors

Scintillation detectors have found use in heavy ion detection as transmission detectors. As a thin film, scintillation detectors can be made much thinner (around 0.2 μm) [7] than semiconductors. As a result, less energy is deposited in the scintillators.

Scintillators operate by converting energy, deposited by transiting energetic particles, into light. Some of the deposited energy goes toward exciting electrons into energy states 3 - 4 eV higher than the ground state. As these electrons decay back into the ground state, radiation in the form of visible light is emitted. This light is transmitted through the optically clear scintillator and a portion strikes the photocathode of an adjacent photomultiplier tube. Some scintillators contain a wave-shifter which absorbs the initial emitted light and re-emits at a longer wavelength. Wave-shifters are usually used if self-absorbance of the photons at the original frequency range is a problem. Photons striking the photocathode of a photomultiplier (PM) tube cause the emission of electrons which are then accelerated toward the dynodes of the photomultiplier. The dynodes multiply the charge into a usable signal.

Because of the many steps involved, with a statistical loss of resolution in each step, the energy resolution for scintillators is below that of semiconductors. As a result,

scintillators are not used for residual energy measurements of heavy ions. However, several factors make them attractive as transmission detectors (dE/dx). First, their thin sensitive region leads to a smaller energy loss. Second, their time resolution is better than that of semiconductors and gas-ionization detectors. This is very important in time-of-flight measurements. Since the time resolution is dependent mainly on the decay constant of the higher energy states (and not the electron drift velocity), scintillator timing is a function of the scintillator material. Thin film scintillator materials are chosen for their time resolution and luminescence efficiency. In addition, the detected luminescence may yield information on particle type, in contrast to carbon foils. Also, because thin film plastic scintillators are generally not crystalline, they tend to be more resistant to radiation damage than solid state systems. Disadvantages are that the energy loss and light output are not proportional to the incident energy. These parameters must be determined from calibration curves or from other measurements. In addition, the energy (or signal) resolution is not as good as that of semiconductors.

Descriptions of specific thin-film, charged particle detectors will be included in the section on previous thin film research.

Previous Thin Film Scintillator Research

Previous research into thin film scintillation detectors is divided into two categories. The first subsection consists of measurements of various thin film properties (detector responses, efficiencies, etc). The second subsection details different thin film scintillator detection systems and their results.

Measurement of Thin Film Scintillator Properties

Previous research on thin film scintillators has measured various properties of these detectors [7-20]. Some of the parameters investigated were detector response versus incident particle energy for various nuclei, energy resolution versus film thickness and energy loss, timing resolution, and energy loss vs. incident particle energy. The detection system generally used for these measurements was a thin-film scintillator - surface barrier detector (TFD-SBD) system. A brief summary of some of this work is given in the following pages.

Luminescence response for various nuclei

The thin film scintillation detector responses for various incident nuclei were measured for accelerated atoms from ^{1}H to ^{127}I and also for ^{252}Cf and ^{235}U fission

fragments. Maximum energies of the incident particles were
below 4 MeV/amu (except for ^{40}Ar, which was around 7
MeV/amu). Curves for several different nuclei showing
scintillator response are shown in Figure 1-3 [7,12]. The
thin film response increases until it peaks with an incident
energy of about E/m = 2.0 - 3.0 MeV/amu, then levels off
and slowly decreases. This behavior is independent of
nuclei. Since a certain luminescence reading might result
from a particle energy above or below the maximum,
luminescence measurements alone are not sufficient for
determining incident particle energy, even for a known
particle. However, the scintillation response can determine
the particle type if the incident energy is high enough.
Beyond the peaks in Figure 1-3, the luminescence varies
slowly with energy. In this region, the separation between
neighboring atoms is sufficiently large to enable particle
resolution.

Luminescence resolution vs film thickness

As the plastic scintillator (NE 102) film thickness is
increased, detector luminescence resolution improves. This
is primarily due to the larger signal resulting from more
energy deposited in the film. A larger signal, for a random
process, yields a statistically better value [12]. ^{40}Ar
atoms were accelerated through thin film detectors of

18
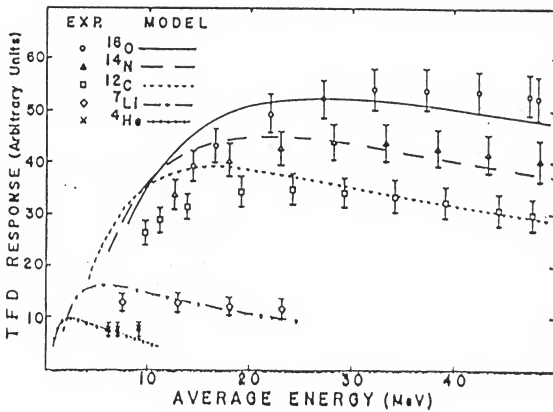
Figures 1-3: Thin film response for various incident nuclei [7].

thicknesses 0.1 mg/cm^2 and 0.4 mg/cm^2. The argon atoms were accelerated to 138 MeV and 125 MeV for the 0.1 mg/cm^2 and 0.4 mg/cm^2 films, respectively (the energy difference should have little effect on the signal). With the TFD responses normalized to the same pulse height, the fwhm/signal for the 0.4 mg/cm^2 film was about half that of the 0.1 mg/cm^2 film (roughly 0.16 vs 0.33). Therefore, thicker films should be used in this research as long as the energy loss is not too great.

Energy loss vs incident energy

The energy loss vs. incident energy curves show a Bragg curve like behavior. At high energies, the ions are in contact with the films for a shorter period of time. Therefore, they lose energy at a rate inversely proportional to the velocity. However, at energies below several MeV/amu, the ions start picking up electrons from the material. This lowers the ionic charge of the atom, thus reducing the effect from the electric field and thus energy loss. This is shown in Figure 1-4 [12].

Timing characteristics

The time-of-flight (TOF) resolution was measured using a TOF-SBD system [21]. A TFD was used as the start detector. For ^{16}O atoms, accelerated into the system, the
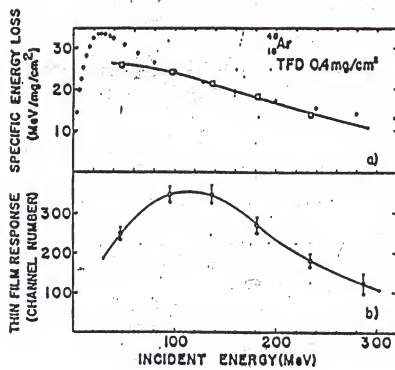
Figure 1-4: Thin film response and energy loss vs. incident
energy for ^{40}Ar nuclei [12].

fwhm was measured for NE 102 films. Increasing the ^{16}O
energy resulted in an increased time resolution (smaller
fwhm). This can be attributed to the statistical effects
from a larger signal, which reduces the uncertainty in the
start signal.

However, an unusual effect was shown by increasing the
film thickness. The decay constant actually increased with
increasing thickness [10].   Since this parameter is a
function of the scintillator material, it should remain
constant. Below film thicknesses of roughly 1 um, the
emitted primary light does not interact with enough of the
wave-shifter to affect the signal. Above roughly 10 um, the
scintillator acts like a ternary system. Between 1 um and
10 um, there is a transition from a binary to a ternary
system. As a result, the standard deviation of the signal
increases from roughly 370 ns ,below 1 um, to 600 ns, above
10 um. This time difference has no effect on this research.

**Charged Particle Detection Systems Employing Thin Film
Detectors**

This section will examine various charged particle
detection systems employing thin film scintillators. Most
of the systems take advantage of the timing characteristics
of the thin film scintillators for time-of-flight
measurements. Others also take advantage of the
luminescence signal for particle detection and measurement.

These systems will be classified according to the data used for ion identification (tof, ΔL, L, and E).

ΔL - L system

While ΔE - E detector telescopes are commonly used for charged particle detection, this system utilizes a Δ - L arrangement for the identification of various particles [22]. A fast scintillator (NE 102A) is used for the Δ signal while a slow scintillator (NE 115) is used for the L component. The difference in decay times allows for the separation of the two signals.

In order to take advantage of the simplicity of the system, the scintillators and photomultiplier (PM) are combined. The two scintillators (0.1 mm NE 102A and 10 mm NE 115) are heat-pressed together so that there is no dead layer of glue or optical grease along the flight path of the particle. The scintillators are then glued to the PM tube with optical cement. Aluminized mylar is then wrapped around the sides for reflection and to prevent any stray light from entering the scintillator. A series of 16 detectors, with a diameter of 20 mm each, was used to increase the solid angle for the system.

The anode signal consists of a large pulse of short duration (ΔL) superimposed on a lower amplitude pulse of long duration. The signals were amplified and split into two analog-to-digital converters. Separate gates split the

signal into the fast and slow components. The primary decay
time for NE 102A is 2.4 ns. After taking the time
broadening from the circuits into account, a charge
integration time of 25 ns was used for the Δ signal. NE
115 has a decay time of roughly 225 ns. Therefore, an
integration time of 200 ns was chosen, going from t = 150 ns
to t = 350 ns. This would avoid the non-exponential decay
component of the fast signal (100 ns), avoid any reflection
from the fast signal, and sufficiently bracket the slow
signal for good energy resolution.

This system was used to detect the particles emitted
from the acceleration of various isotopes into several
targets. 54 MeV α particles, 53 MeV ^{6}Li ions, and 106 MeV
^{12}C ions were accelerated onto ^{27}Al, ^{122}Sn, and ^{197}Au
targets. For all cases, there was a sufficiently large
separation between the light atoms (Z <6) to differentiate
between adjacent elements.

The primary advantages of this system are it's
simplicity and high geometric efficiency (since multiple
detectors can be used). However, film uniformity could be a
problem for detecting higher LET radiation like fission
fragments. A much thinner ΔL detector than 0.1 mm would be
required since all fission fragments would be stopped in a
0.1 mm ΔL detector.

Time-of-Flight -- E detection systems

Thin film scintillators have proven useful in time-of-flight systems. Their excellent timing characteristics along with their thin size yields an excellent signal with very little energy loss. Typically, a TFD is used as a "start" signal while an SBD is used as a "stop" signal and residual energy detector. Usually, the luminescence is also measured because it would add another parameter to the system with very little additional equipment. However, several systems did not utilize this capability. One of these systems will be examined below [21].

This experiment was designed to measure the timing properties and to optimize the time resolution of the system. Therefore, two different scintillators were tested and other parameters varied in order to investigate the various effects.

The detection system consists of a thin film scintillator and an SBD. The thin film is surrounded on one side by a reflecting hemisphere and on the other side by a photocathode. In this way the geometric efficiency (fraction of light emitted by the scintillator hitting the photocathode) can be made to approach 1.

The first experiment involved testing two different types of scintillator films for timing resolution (NE 111 and NE 102). The source was a 50 MeV ^{16}O beam. In order to minimize the time spread from unequal energy loss in the

film or unequal initial ion energy, the SBD was adjusted to be 5 cm from the film. The resulting Δt's (fwhm) were 480 ps for NE 111 and 635 ps for NE 102A for energy losses of 375 and 425 keV, respectively. Therefore, for the rest of the experiments, NE 111 was used.

Next, the time resolution vs. particle energy loss in the scintillator was investigated. Films producing energy losses from 375 keV to 3.0 MeV were tested. Also tested was the effect of rotating the film from an angle of 45° (relative to the beam) to 90° (normal to the beam).

The resolution improves steadily as the film thicknesses were increased. The resolution improved from roughly 480 ps for $\Delta E = 375$ keV to 200 ps for $E = 3,000$ keV. The resolution also improves slightly for a film position normal to the ion beam. With the film at an angle to the beam, any spread in the beam width will cause the ions to strike the film at different times. This results in an additional loss of resolution.

Finally, this system was used to measure the reaction products of 50 MeV ^{16}O ions accelerated into two targets. These targets consisted of: **1.** ^{7}Li and ^{12}C and **2.** ^{40}Ca and ^{42}Ca on a ^{12}C backing. A film thickness corresponding to an energy loss of 1.37 MeV (for 50 MeV ^{16}O ions) was used with a flight path of 1.5 m. By measuring the energy and time (with a known flight path), the mass is given by:

$$m = 2E/v^2 \qquad (v=d/t)$$

Excellent mass separation was given for both targets.
Nuclei between A = 12 to 24 were easily distinguished for
target 1, while nuclei between A = 16 to 42 were separated
for target 2.

While NE 111 has better timing characteristics than NE
102A, its lower light output results in poorer luminescence
resolution. Therefore, NE102 is preferable for certain
situations.

This system gives very good mass resolution for low
mass ions at specific energies of several MeV/amu. However,
it begins to break down for higher mass ions (A>40) at lower
specific energies. The overlap between adjacent elements
becomes too severe for particle separation.

ΔL - Residual energy

This is the most common of the thin film scintillator
systems. This method consists of a thin film in series with
a semiconductor detector. This system is popular because of
its simplicity and portability. Few electronic components
are needed. One representative system will be examined and
the results summarized.

This experiment [11] investigated proton-induced
fission of ^{232}Th, and compared it to proton-induced fission
of ^{235}U, ^{238}U and ^{252}Cf spontaneous fission. Protons were
accelerated into a nickel foil onto which an oxide of
thorium or uranium had been deposited. The detection system

was placed off-beam to avoid the direct proton beam. This setup, along with the associated electronics is shown in Figures 1-5.

This experiment used the ΔL-E system to investigate the effects of varying the incident proton energy on the fission process. Accelerated protons were incrementally increased in energy from 10.0 to 17.5 MeV. The fission fragments resulting from this beam were detected and various parameters studied. Among these were the light and heavy fragment locations for the TFD and SBD, and the peak-to-valley ratios for the TFD and the SBD.

From the peak location data, the identity of the fissioning isotope could be established. This is shown in the contour plots of Figure 1-6. Varying the proton energy had little effect on the overall fission fragment energies.

This experiment shows how a simple system utilizing luminescence and energy data can be used to identify charged particles. With this experiment, no attempt was made at peak mass or energy identification and the overall system did not provide enough data to enable any detailed fission fragment identification.

ΔL - Time-of-Flight - Residual energy

This system is similar to the ΔL-E system previously described, except that it also measures the time-of-flight between the film and the SBD. This experiment was performed
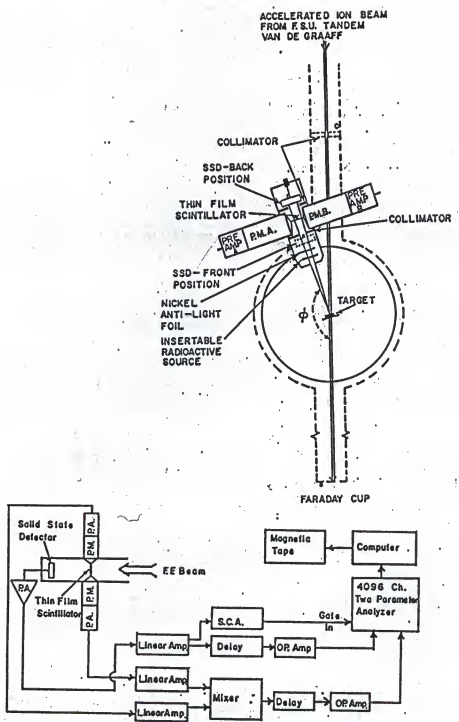
Figure 1-5: Mechanical and electrical setup for proton-
induced fission studies of ^{232}Th, ^{238}U, ^{235}U, and
spontaneous fission of ^{252}Cf [11].
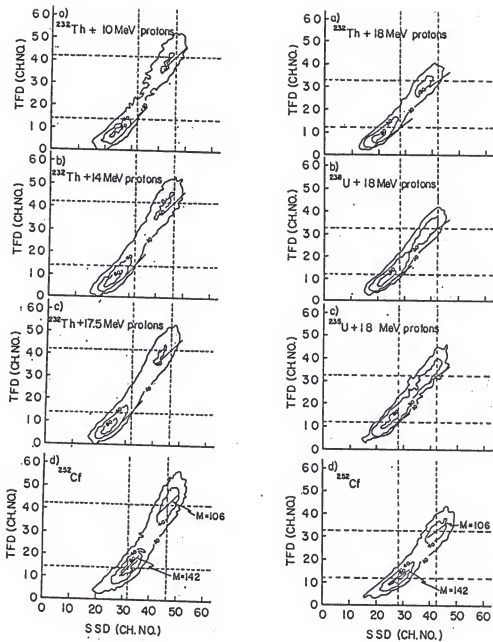
Figure 1-6: Contour plots for proton-induced fission of ^{232}Th, ^{238}U, ^{235}U, and spontaneous fission of ^{252}Cf [11].

to determine the applicability of such a system for detecting very low levels of spontaneous fission activity, such as from superheavy nuclei [23]. For this experiment, an accurate mass and energy determination for both fragments is attempted. The experimental arrangement would therefore need two separate ΔL-tof-E systems opposite each other. However, for this preliminary setup, only one system was used. This is shown in Figure 1-7.

The SBD could be moved as close as 10 cm from the source to aid in the calibration of the tof. Three-dimensional contour graphs give the number of counts (Z-axis) vs the luminescence (X) and the SBD signal (Y). These plots give clearly defined peaks.

3TFD - Time-of-Flight system

The 3TFD-tof system was designed to determine the effectiveness of multiple films for particle identification [24]. Two experiments were performed. In the first, various germanium and selenium isotopes were accelerated into a gold foil resulting in scattered Ge and Se atoms of various energies. The isotope energies ranged from 48 to 153 MeV incident on the detection system. In the second, ^{252}Cf fission fragments were detected. For this system, a Ge(Li) detector was placed opposite the films for the detection of gamma rays. This enabled coincident
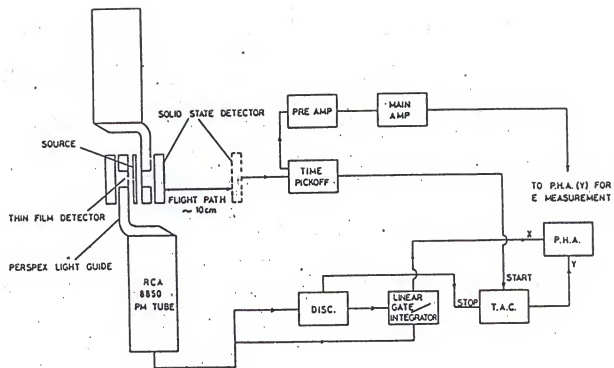
Figure 1-7: Block diagram for ΔL-tof-E system [23].

measurements with the prompt gamma rays from fission fragments.

In the first set of experiments, film response was measured for various Ge and Se isotopes and energies. The luminescence responses were followed through the three films for each isotope. TOF measurements were also taken between the films. This enabled the luminescence to be plotted vs the velocity. The results obtained were similar to previous single TFD-SBD experiments for other atoms. The utility of the multiple film system was shown, however, by following particles of different ionic charge. By tracking accelerated atoms of different charge states, it was discovered that the TFD response slowly converged. This corresponded to the isotopes reaching an equilibrium charge state as the particles passed through the films. This would not have been evident with a single film.

The second experiment investigated coincidence measurements of Cf^{252} fission fragment prompt gamma rays and TFD signals. This setup is shown in Figure 1-8.

The gamma spectrum and TFD signals were collected. When a gamma ray corresponding to a certain isotope's prompt gamma was detected, the TFD signals were counted. When operated in this mode, ^{106}Mo and ^{148}Ce prompt gammas were used as the trigger. Although the background levels were high, a ^{106}Mo peak was evident in the first case. For the ^{148}Ce gamma, a zirconium peak was evident (zirconium is the complementary fission fragment for cerium).
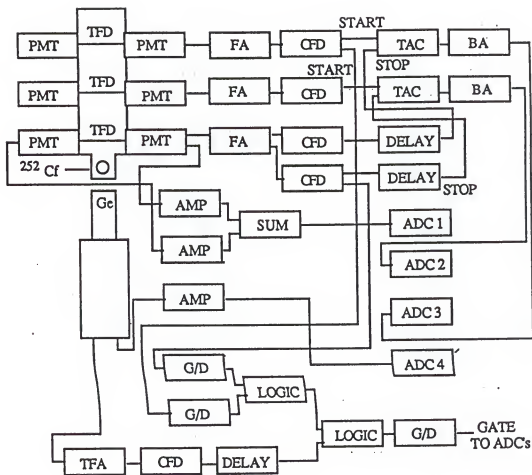
Figure 1-8: Block diagram of experimental equipment used in ^{252}Cf fission fragment coincident measurements with prompt gammas [25].

The 3TFD system is virtually the same as that being used in the current research, with the addition of an SBD. Little use was made of the multiple luminescence measurements. Only in the charge state analysis was the 2nd or 3rd film needed. However, these experiments did show the utility of having multiple films in that the luminescence responses could be followed through the system to see the effects (on the signals) of degrading the particle energy.

CHAPTER 2

THIN FILM FORMATION AND TESTING

This section examines the different experimental setups used in the manufacture and testing of the scintillator films. The primary areas are thin-film formation and the single TFD-SBD system.

Thin Film Formation

Two types of films, NE-102 and VYNS (a strong, thin plastic used for support), were produced using the same method. The method used is described below. NE-102 is a commercial plastic scintillator with an excellent combination of high light output and fast decay time. VYNS is a strong, and essentially non-scintillating, plastic used for support.

A plastic solution is formed by dissolving NE-102 or VYNS in a suitable hydrophilic solvent. For these plastics: 12 g of NE-102 shavings are dissolved in a mixture of 50 mL ethyl acetate and 2.2 mL amyl acetate, and 4.0 g of VYNS (polyvinyl-acetate polyvinyl-chloride copolymer) powder is

dissolved in 50 mL of cyclohexanone. The solution is then
allowed to sit (with an occasional stirring) until a
completely homogenous mixture results. This typically takes
a day.

The films are formed using a common technique as
described by Muga [25]. A porcelain developing pan is
partially filled with de-ionized water. De-ionized water is
used to reduce the amount of impurities that might come in
contact with the film. A glass plate is placed in the water
such that it leans against the side of the pan, with the
lower end of the plate resting in the water, as seen in
Figure 2-1. The plate should make about a 30° angle with
the water. Using a Pasteur pipette, a small drop of
solution is placed on the glass above the water and allowed
to slide down the plate. When the drop reaches the water, a
thin plastic film quickly spreads out over the surface,
while the hydrophilic solvent is absorbed by the water. A
uniform section of film (as determined by interference color
patterns), free of blemishes is lifted off the water using a
wire ring roughly 8 cm in diameter, as seen in Figure 2-2.
Better adhesion to the wire ring can be achieved by wrapping
previous films around the metal ring, thus creating a
plastic-plastic contact. The film is then mounted on a
square support frame 2.8 cm on a side with a square 2.0 cm
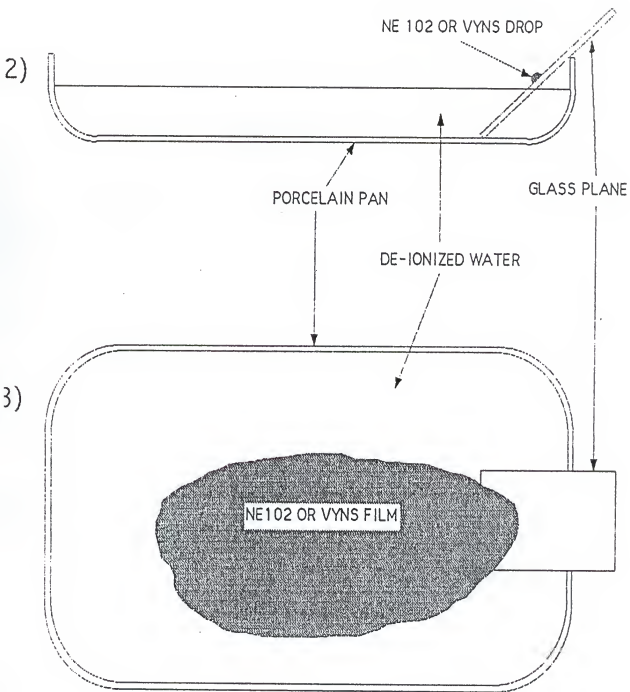
Figure 2-1: Developing pan arrangement for thin film
formation.

NE102 OR VYNS FILM

WIRE RING

SUPPORT FRAME
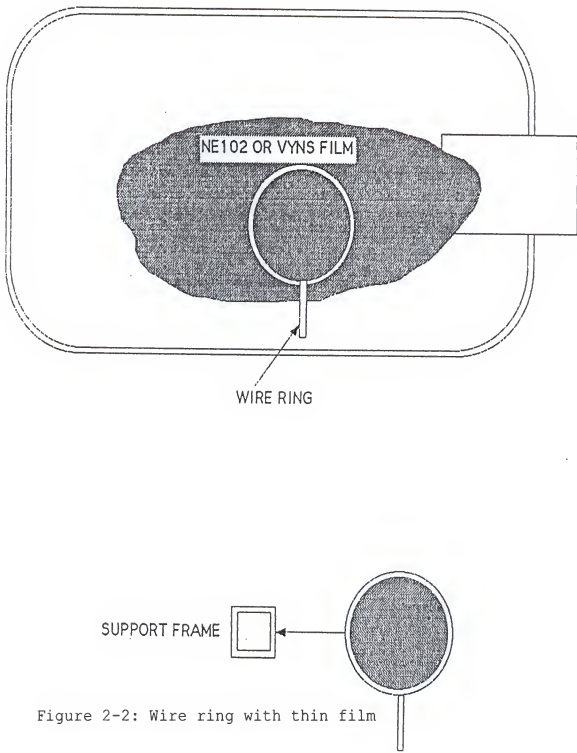
Figure 2-2: Wire ring with thin film

hole cut out of the middle. To form a good film-frame seal, a thin coating of vacuum grease is spread over the frame before the film is placed on it.

Using this procedure, NE-102 films of roughly 0.3 um thickness are produced while VYNS films of roughly 0.1 um are produced. Desired film thickness can be achieved by placing successive film layers on the support frame. Since NE-102 tends to be very brittle and can easily tear, the NE-102 films are sandwiched between two VYNS films. Although this will add roughly 0.2 um of non-scintillating material to each film, it is necessary to avoid breaking the delicate films.

Commercial plastic scintillators (like NE-102) typically contain 2-3 % primary scintillator (para-terphenyl) and a small amount of wave shifter (0.2 - 0.3 % POPOP) mixed in a support matrix (polyvinyltoluene). Since commercial scintillators have such a low percentage of primary scintillator, it was theorized that by depositing pure primary scintillator onto an ultrathin support film, greater light output could be achieved for a given energy loss. Therefore, by depositing pure para-terphenyl onto a VYNS film, this hypothesis could be tested.

Para-terphenyl is a plastic that forms small flakes in its pure form. In its pure form, it cannot be formed into a film, so another method of depositing it onto a VYNS film was needed. Dissolving the p-terphenyl and then evaporating the solution on the VYNS film was tried. However, as the

solvent evaporated, the resulting p-terphenyl tended to form flakes roughly 0.1 mm in size. This is several orders of magnitude larger than what is required for a uniform deposition. Para-terphenyl sublimates under high temperatures and low pressures. Therefore, using vapor deposition, a uniform layer could be deposited.

Using the setup shown in Figure 2-3, roughly 10 mg of para-terphenyl is placed in a tantalum container which is then covered except for a pin hole on the top. The tantalum container is connected to two electrodes. A VYNS film is held about 10 cm above the container by a stand. A bell jar is placed above the film and container assembly and vacuum sealed. The bell jar is evacuated to below 100 μm Hg. A 10-20 A current is passed through the electrodes and container from a high-current transformer. The ohmic heating of the tantalum, along with the low pressure causes the para-terphenyl to sublimate. The scintillator vapor exits through the pin hole and is aimed toward the VYNS film. A portion of the vapor solidifies on the cold film, leaving a thin layer of para-terphenyl micro-crystals. The thickness of this layer can be controlled by changing the amount of para-terphenyl initially placed in the container, or by successive depositions. Since p-terphenyl is not clear, only the light emitted near the surface will not be

BELL JAR

TANTALUM
CONTAINER

VACUUM
PUMP

HIGH CURRENT
TRANSFORMER

ULTRA-THIN
VYNS PLASTIC FILM

PARA-TERPHENYL
VAPOR

TANTALUM
CONTAINER

ELECTRODES
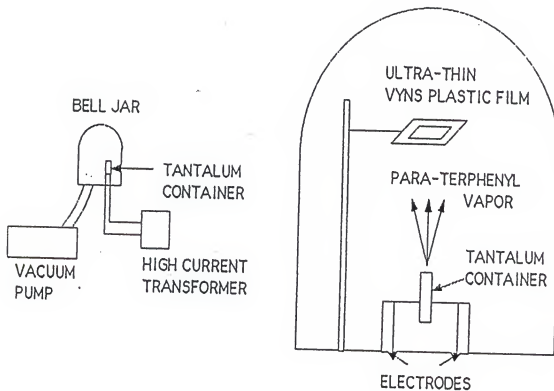
Figure 2-3: Vapor deposition setup

re-absorbed. Therefore, thicker layers may not result in an increase in luminescence.

Thin Film Testing: Single Film System

This system will test each film independently to determine its detection characteristics. Among the factors to be measured are film uniformity, energy loss, and luminescence. A diagram of the mechanical setup is shown in Figure 2-4. A ^{252}Cf source will provide the heavy ions (fission fragments). This isotope has been studied extensively and its fission fragments are well characterized [26-32].

Film uniformity is critical in acquiring a thin film signal with good resolution and also in maintaining a relatively constant energy loss. An indication of this parameter can be determined in several ways: first, by visually inspecting the films, diffraction patterns immediately indicate a difference in film thickness, second, by measuring the thin film scintillator spectrum, the peak-to-valley ratios of the two californium peaks give a measure of the uniformity of the luminescence signals. However, this parameter is also affected by film thickness. Finally, by measuring the residual energy spectrum from the semiconductor, and comparing it to the spectrum without the
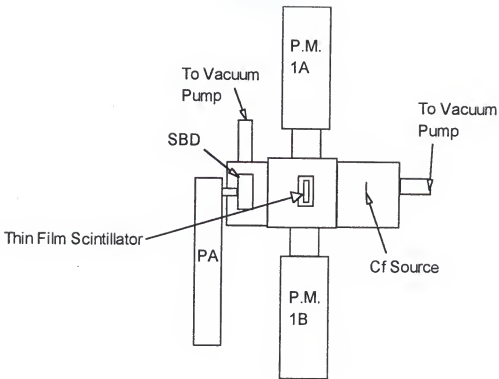
P.M. = Photomultiplier Tube and Base
S.B.D. = Surface Barrier Detector
PA = Preamp
Cf = Californium-252 Source

Figure 2-4: Mechanical setup of single thin film system.

film, the broadening can be noted. This procedure will also determine the energy lost in the film. By measuring the peaks of the light and heavy fission fragments with and without the film, average energy deposited can be determined. These values can then be correlated with calibrated data and scintillator thickness can be verified.

Luminescence measurements from the scintillator should be as large as possible for a given film thickness without a loss of resolution. This can be achieved mainly by careful preparation of the thin films. Some of the factors that may trap or scatter light causing a decrease in luminescence are: dust, air or water bubbles, and cracks in the film. All of these are visible to the eye.

Two scintillator films, NE-102 and p-terphenyl, will be tested with this system to determine their suitability for further study. The light output vs. energy loss will be plotted for each and compared.

Since the same detection system will be used for both types of films, the light collection efficiency for each film will be examined. The emission spectrum of a scintillator is a function of the chemical components of that scintillator. Although the primary scintillator for NE-102 is p-terphenyl, it's spectrum will be closer to that of it's wave-shifter. Therefore, the spectrum for NE-102 will be shifted to a higher wavelength. The spectra for NE-102 and p-terphenyl are shown in Figures 2-5 and 2-6
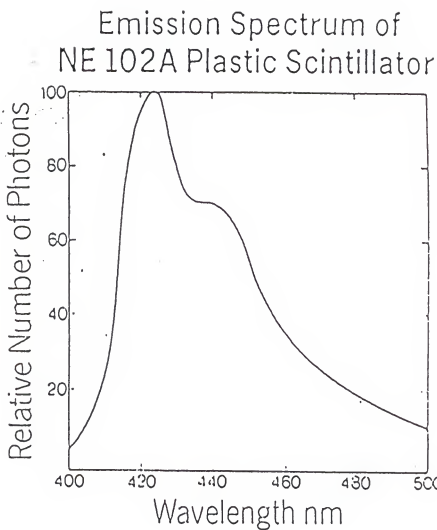
Figure 2-5: NE-102 emission spectrum [33].
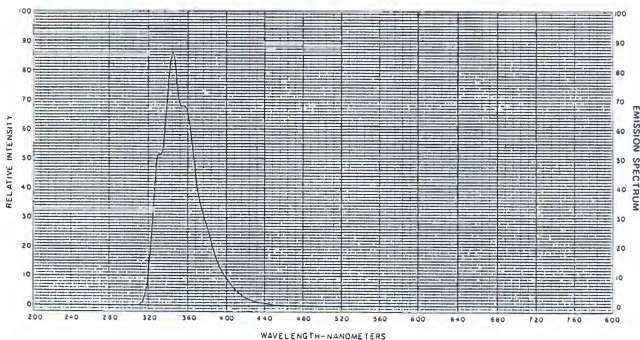
Figure 2-6: Para-terphenyl emission spectrum [34].

[33,34], respectively. It is not clear whether the NE-102 films, of thicknesses used in this work, will exhibit a binary or ternary behavior. For this analysis, it is assumed that they will behave like a ternary system.

The emitted light is then absorbed by the photocathode of the photomultiplier. Therefore, for this experiment to be valid, the photocathode must have a similar absorption efficiency over both emission ranges, or the difference must be taken into account. The photocathode absorption efficiency spectrum is shown in Figure 2-7 [35]. The photocathode is fairly efficient over the wavelengths associated with the p-terphenyl and NE-102 light emission. Also, the response is similar over the ranges of both spectra. Therefore, no adjustments are required.

NE-102 films with thicknesses resulting in light fragment peak energy losses of 5 to 60 MeV were tested. A plot of the luminescence output vs energy loss is shown in Figure 2-8.

Para-terphenyl films were tested that resulted in energy losses from roughly 8 MeV to over 80 MeV. A graph of luminescence vs. energy loss is shown in Figure 2-9.

Comparing the two graphs, it is clear that NE-102 gives a considerably higher specific luminescence. The NE-102 luminescence is almost double that of the p-terphenyl. Also, at higher energy losses (above 60 MeV), there seems to
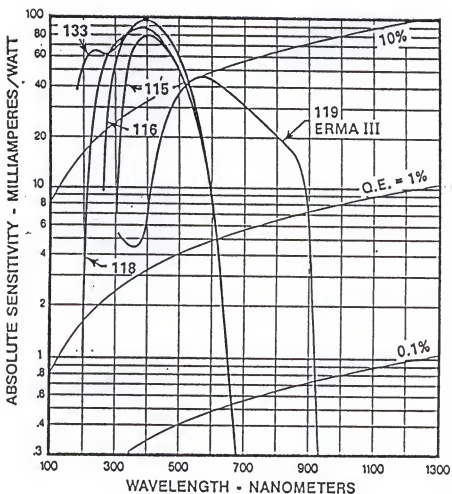
Typical Photocathode Spectral Response Characteristics

Figure 2-7: Photocathode absorbance efficiency spectrum, photocathode used corresponds to number 116 [35].
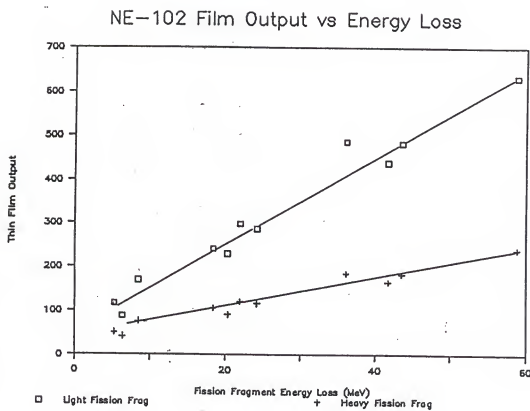
Figure 2-8: NE-102 luminescence output vs energy loss (MeV).
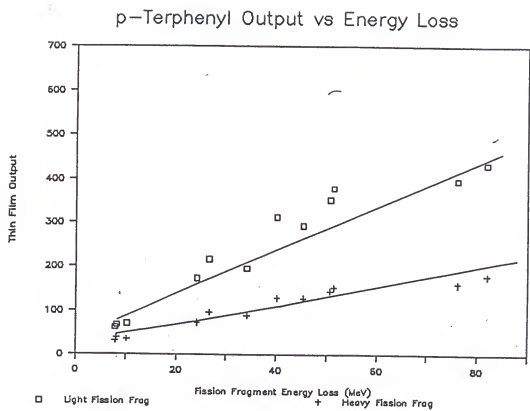
Figure 2-9: Para-terphenyl luminescence output vs energy loss (MeV).

be a tailing off of the luminescence possibly resulting from an approach to an "infinite" thickness for luminescence emission. The most probable reason why the output for p-terphenyl was significantly lower than that of NE-102 is self-absorption. A large portion of the light produced is immediately re-absorbed before it can "escape" the film. In the NE-102 film, the waveshifter (POPOP) absorbs the initial luminescent light and re-emits it at a longer wavelength. At this wavelength, NE-102 does not absorb.

From the NE-102 data, a film thickness must be chosen for multiple film experiments. Since the light fragments initially have about 104 MeV, the energy loss should be kept below about 30 MeV for each film to enable sufficient residual energy for a 3-film system. The films that resulted in an energy loss of below 10 MeV had poor resolution. Therefore, for this work, films were produced that resulted in an energy loss of roughly 20 MeV.

CHAPTER 3

MULTIPLE THIN FILM SYSTEM

A multiple thin film system was constructed in order to simultaneously measure several signals resulting from the passage of fission fragments. The use of multiple films would take advantage of several factors. Among these are: time-of-flight signals between films, increased luminescence resolution from the use of multiple thin films, and ease of energy calibration by the use of different thickness films.

Utilizing the multiple parameters available, a method for the determination of nuclear charge (Z) will be formulated. Using this method, other parameters can be investigated as a function of Z (particle mass has typically been used).

Multiple Thin Film Detector Setup

The mechanical assembly used is shown in Figure 3-1. It consists of a source chamber, four thin film detector (TFD) cells (one used as a spacer between films 1 and 2), a chamber with two large wheels used for fragment energy attenuation, and an end piece with the surface barrier
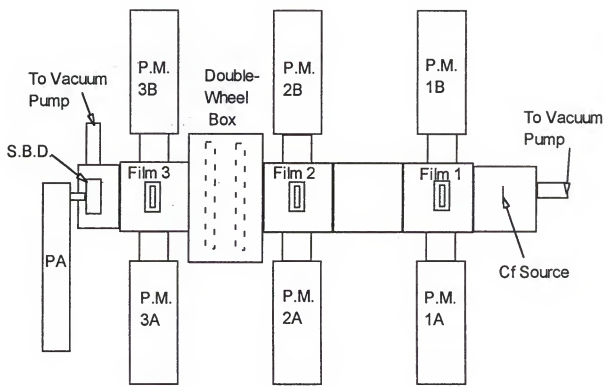
P.M. = Photomultiplier Tube and Base
S.B.D. = Surface Barrier Detector
PA = Preamp
Cf = Californium-252 Source

Figure 3-1: Mechanical assembly of 3-TFD system.

detector. The assembly is operated under vacuum conditions. The films had thicknesses of 1.14 μm, 1.72 μm, and 2.04 μm for films 1, 2, and 3, respectively.

The source consists of a ^{252}Cf spontaneous fission source deposited on a thin metal backing. This is contained in the source chamber which can be isolated with a valve from the rest of the assembly. This enables the source to be under vacuum conditions at all times, even when the rest of the system is open. When the detector assembly is not collecting data, closing this valve also prevents the fission fragments from striking the SBD, thereby lessening any long-term detector deterioration.

The detector chamber consists of the thin film chambers, a dual-wheel chamber allowing for multiple combinations of energy-attenuating films, and a surface barrier detector end assembly. A diagram of one thin film chamber is shown in Figure 3-2. The film can be retracted out of the ion path without loss of vacuum.

A diagram of the dual-wheel assembly is shown in Figure 3-3. Each wheel can be moved independently. By inserting films of various thicknesses into the locations provided, multiple combinations of total film thicknesses can be achieved. This was used primarily in attenuating the fission fragments while calibrating the SBD. Since there are no connections for photomultipliers, no scintillator
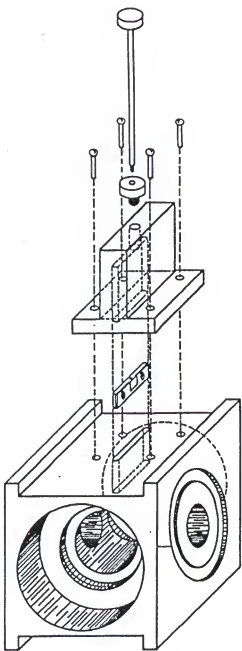
Figure 3-2: Thin film chamber [25].
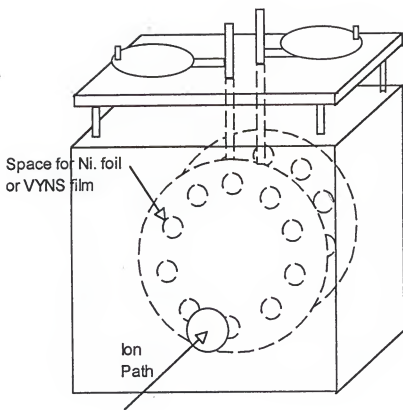
Figure 3-3: Dual-wheel chamber.

signals are possible. Therefore, the more durable VYNS films (a weak scintillator) were used instead of NE-102.

The SBD is contained in the end chamber. The SBD screws into a terminal which provides the necessary support, signal, and voltage connections. The valve connecting the detector chamber to the vacuum pump is also contained in this chamber.

The electronic configuration is shown in Figure 3-4. All channel data are saved separately to facilitate computation (paired TFD signals are not summed). The system is triggered by a fast coincidence signal from the anodes of PM tubes 1A and 3A. A software verification is then made on the digitized SBD signal. If it is above a certain preset level (chosen to be well above the alpha energies, but well below the fission fragment spectrum), then the signal is determined to be from a fission fragment and the data is saved. A more detailed description of the electronics, timing, and triggering mechanism is given in Appendix C.

System Calibration

Before any Z identification can be attempted, the various parameters must be calibrated. The SBD signal must give the correct residual energy, the time-of-flight must give the true time, and the TFD signals must be adjusted so
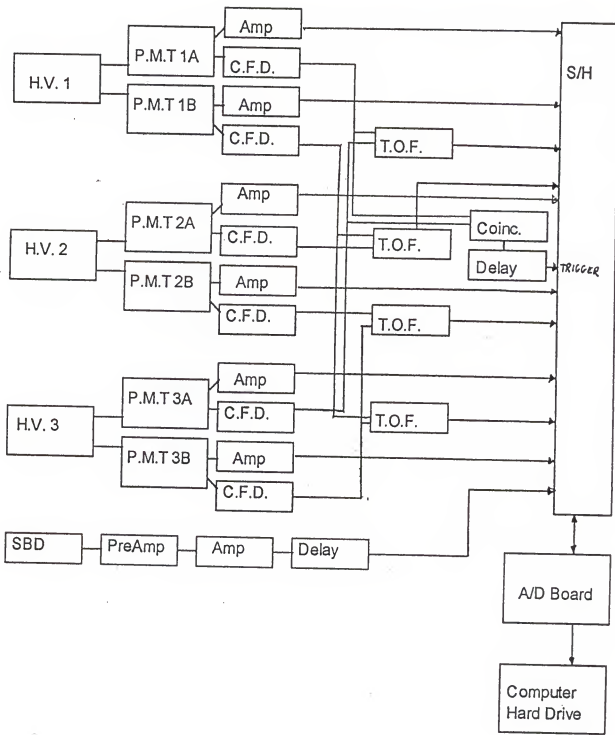
Figure 3-4: Electronic configuration of 3-TFD system.

that the signals from the paired PM tubes match and the summed pairs also match.

While calibrating the TOF measurements for the three film system, it was discovered that the TOF spectra between films 1 - 2 and 2 - 3 gave poor resolution. This can be seen in Figures 3-5 and 3-6. The resolution for TOF 1-3, shown in Figure 3-7, was very good. However, since this measurement consists of the times resulting from two different velocities, it was of minimal use in subsequent calculations. By withdrawing the second film, a TOF 1-3 measurement could be made that could be used directly in velocity and energy calculations. However, this would also result in the loss of the luminescence signal from the second film. The total luminescence (summed luminescence signals from all films) for the 3 and 2 film systems are shown in Figures 3-8 and 3-9. As seen in these figures, the loss in TFD resolution is small compared to the improvement in TOF resolution. Therefore, a 2 film system was employed.

Surface Barrier Detector Energy Calibration

In the measurement of heavy ions with a surface barrier detector, a small but significant portion of the ion's energy is not collected by the detector. Therefore, the resulting signal is not a direct representation of the ion's energy. In order to determine particle energies, the SBD must be calibrated for heavy ions. Two methods will be examined and compared.
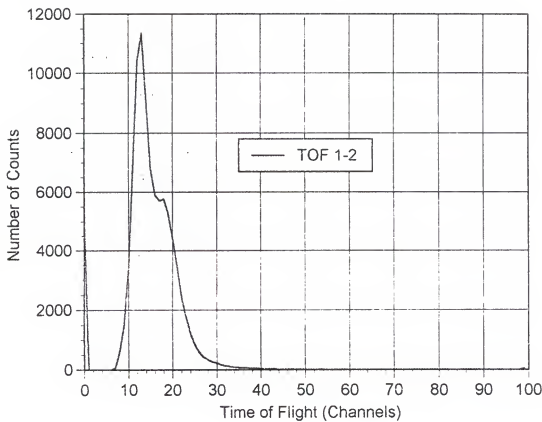
Figure 3-5: TOF spectrum for films 1-2 for the 3 TFD system.
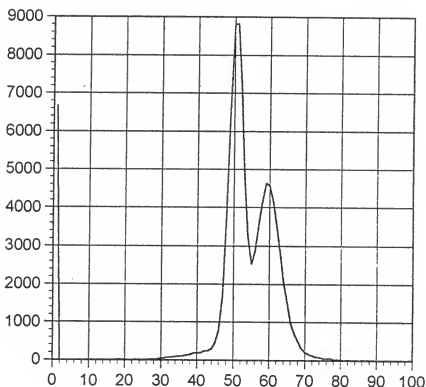
Figure 3-6: TOF 2-3 spectrum for the 3 TFD system.
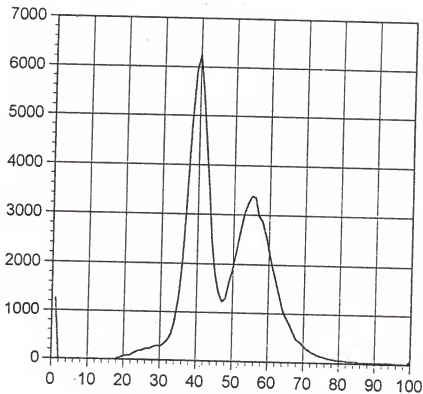
Figure 3-7: TOF 1-3 spectrum for the 3 TFD system.
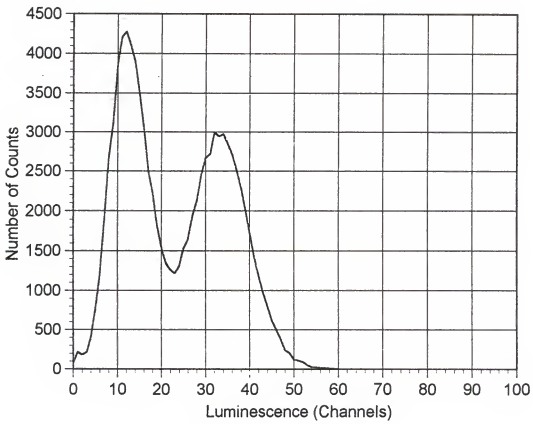
Figure 3-8: Total luminescence signal from 3 TFD system.
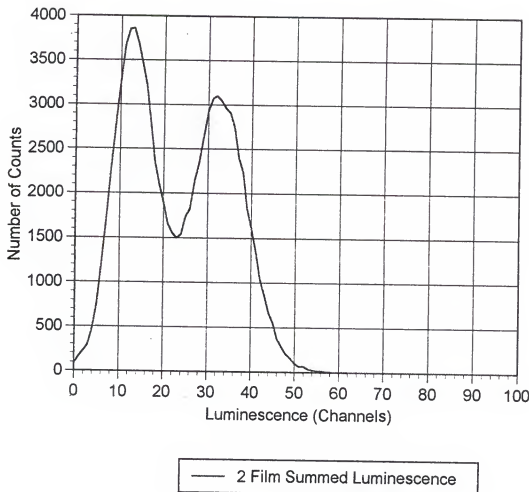
Figure 3-9: Total luminescence signal from 2 TFD system.

The first is a direct correlation between SBD signal and ^{252}Cf fission fragment energy developed by Schmitt [42]. This method uses peak information from an unattenuated source and fragment mass to estimate the energies.

The second method involves calibrating the SBD to give the energy signal resulting from the charge collected by the electrodes (a fraction is not collected due to energy loss in the detector window and recombination). Then, an estimate of the energy "lost" by other processes is made. By adding these values the total particle energy is produced.

The SBD spectra are broken up into 11 groups as shown below. The third and ninth group contain the mean heavy and light fragment peaks respectively, while the sixth group contains the valley segment. The other regions are each split up into two groups. All calculations are performed separately for each group. Below is the listing of approximate group mean atomic numbers and masses, along with the data ranges (% of integrated data) used for each group.

Group	Atomic Number	Atomic Mass	Data Range (%)
1	60	152	0 - 7
2	58	146	7 - 18
3	56	142	18 - 31
4	54	138	31 - 40
5	53	134	40 - 46
6	49	124	46 - 54
7	45	114	54 - 60
8	44	110	60 - 69
9	42	106	69 - 82
10	40	102	82 - 93
11	38	96	93 - 100
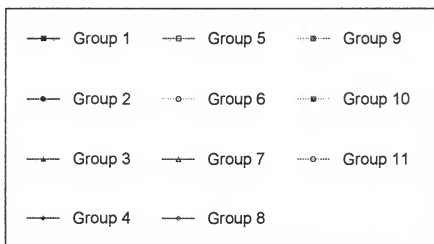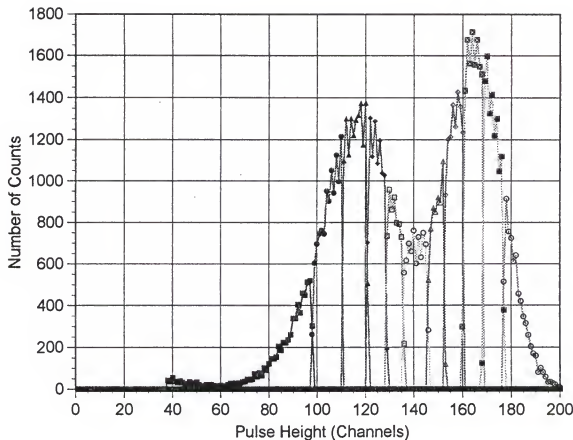
Figure 3-10: 11 Group ^{252}Cf spectrum.

Direct correlation between SBD signal and ^{252}Cf energy

The basic principle behind the method developed by Schmitt [36] is that the signal from heavy ions in SBD's follows the general relationship given below (a more detailed description and derivation is given in Appendix B):

1) $E(Ch,M) = (a + a'M)Ch + b + b'M$

where   Ch = Channel number of signal

M = Ion mass (amu)

a, a', b, b' = Constants dependent on the detector

Schmitt discovered that for a Cf^{252} spectrum incident on an SBD; a, a', b, and b' depended primarily on the peak channels, and fit the data according to the following formulas:

1a) $a = 24.0203/(P_1 - P_h)$ (MeV/Ch)

1b) $a' = 0.03574/(P_1 - P_h)$ (MeV/Ch*amu)

1c) $b = 89.6083 - a*P_1$ (MeV)

1d) $b' = 0.1370 - a'*P_1$ (MeV/amu)

where P_h = Center of the Full Width at 3/4 Maximum of the Heavy Fragments for an Unattenuated Spectrum

P_1 = Center of the Full Width at 3/4 Maximum of the Light Fragments for an Unattenuated Spectrum

Using the previous 11 group masses and experimentally
determined $P_1 = 169.1$ and $P_h = 121.4$, the approximate
unattenuated 11 group corrected mean energies are given
below:

Combining the terms in Equation 1 yields:

2) $E(Ch,M) = (a + a'M)Ch + (89.6083 + 0.1370*M) -$
            $P_1(a + a'M)$

and,

3) $E(Ch,M) = (Ch - P_1)(a + a'M) + 89.6083 + 0.1370*M$

Group	Corrected Energy (MeV)
1	64.7
2	73.4
3	80.0
4	84.8
5	89.2
6	92.8
7	95.7
8	100.5
9	104.1
10	108.7
11	114.8

substituting Equations 1a and 1b, yields:

4) $E(Ch,M) = [(Ch - P_l)/(P_l - P_h)]*(24.0203 + 0.03574*M) +$
             $89.6083 + 0.1370*M$

Among the results from Equation 4 is that for a given
channel number, the particle energy is a linear function of
the mass. Also, that the mass of the ion is the critical
variable, as opposed to the charge.

Plugging the group masses and peak channel data into
Equation 4 yields the linear formula:

5) $E_{Grp}(Ch) = m*Ch + b$

Group	m	b
1	0.6175	6.02
2	0.6130	5.96
3	0.6100	5.92
4	0.6070	5.88
5	0.6040	5.83
6	0.5965	5.73
7	0.5890	5.63
8	0.5860	5.59
9	0.5830	5.55
10	0.5800	5.51
11	0.5755	5.44

The 11 group formulas yield the following data for
total film thicknesses. This is graphically represented in
Figure 3-11. The data was taken over a wide energy range
covering the entire energy region used in this work.

Table 3-1: 11 Group Residual Energy Data vs Film Thickness

Group Energy

| Dx (um)	1	2	3	4	5	6	7	8	9	10	11
0	64.68	73.47	79.95	64.60	89.19	92.82	95.72	100.7	104.1	108.6	114.8
2.03	51.09	59.90	64.15	68.89	73.49	77.91	81.76	85.43	89.23	93.26	98.10
2.42	47.39	54.75	60.19	64.64	68.48	72.84	77.64	81.83	85.44	89.50	94.36
2.79	45.23	52.60	57.57	62.04	66.24	70.39	75.11	79.15	83.11	87.18	92.06
3.17	42.45	49.54	54.70	58.89	62.19	67.17	71.58	75.86	80.19	84.57	89.47
3.56	39.98	47.08	51.96	55.98	59.90	64.37	68.93	72.93	77.10	81.56	86.59
3.75	39.98	46.47	51.22	55.98	50.89	63.59	67.17	72.10	76.28	80.52	85.44
3.93	38.75	44.93	59.00	54.04	59.00	62.40	66.69	70.75	74.94	79.07	84.29
4.14	37.51	43.71	48.42	52.34	56.39	60.91	65.10	69.17	73.19	77.91	82.56
4.51	36.28	42.36	46.77	50.71	54.58	59.00	63.16	66.82	71.27	75.42	80.26
4.89	34.42	40.33	44.64	48.59	52.53	56.85	60.68	64.47	68.53	72.87	77.96
5.28	32.57	38.31	42.50	46.16	49.93	54.05	57.86	61.36	65.32	69.80	75.08
5.65	31.34	36.04	40.06	43.43	46.91	50.89	54.79	58.43	62.70	67.19	72.78
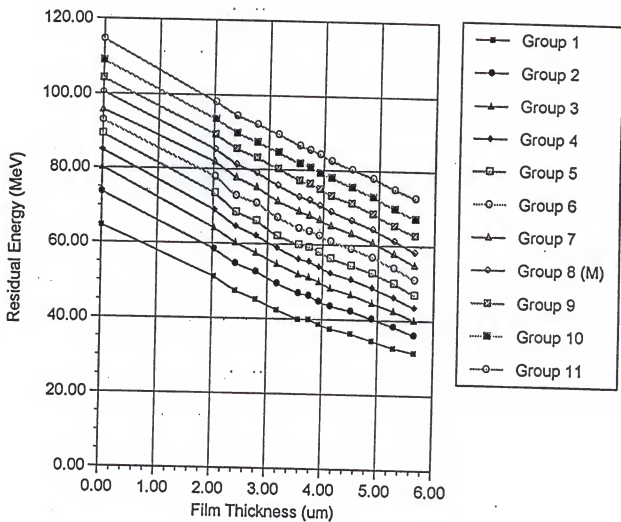
Figure 3-11: 11-group residual energy as a function of film
thickness (Schmitt's formula). The line connecting the
points is used as a visual aid.

Conversion of Schmitt formula to charge dependence

For this work, the nuclear charge is considered the primary factor in luminescence signal and energy loss. It would be very useful to have Equation 4 as a function of charge and not atomic mass. Therefore, another analysis will modify Equation 4 to make it a function of charge, and the results compared with the standard Schmitt method.

^{252}Cf fission fragments have a fairly constant charge-to-mass ratio (Z/M) over the entire range of fission fragment masses. Plotting the 11-group charge-versus-mass data and fitting it linearly, yields the following equation, graphically shown in Figure 3-12:

6) $M = 2.545*Z - 0.514$

Combining Equations 6 and 4 yields a modified Schmitt equation:

7) $E(Ch, Z) = [(Ch - P_1)/(P_1 - P_h)]*(23.9960 + 0.09096*Z) +$
$89.5153 + 0.3487*Z$

Using this formula for the previous 11-group data, yields the following energies.
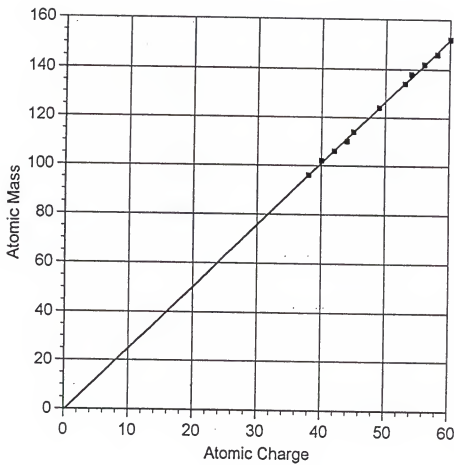
Figure 3-12: Cf^{252} fission fragment charge vs. mass.

Table 3-2: Residual energy data vs film thickness for

Z-dependent Schmitt formula.

Group Energy

Dx (um)	1	2	3	4	5	6	7	8	9	10	11
0	64.68	73.55	80.17	84.78	89.18	92.82	95.74	100.5	104.1	108.7	114.5
2.03	51.09	58.49	64.17	69.00	73.48	77.91	81.78	85.28	89.21	93.37	98.10
2.42	47.39	54.69	60.20	64.75	68.47	72.84	77.66	81.18	95.42	89.60	94.36
2.79	45.23	52.54	57.58	62.14	66.23	70.63	75.13	79.01	83.08	87.28	92.56
3.17	42.45	49.48	54.71	58.99	62.19	67.17	81.66	75.73	63.17	84.67	89.47
3.56	39.98	47.03	51.97	56.07	59.89	64.37	68.94	78.00	78.00	81.66	86.59
3.75	39.98	46.41	51.24	55.47	59.29	63.59	67.88	71.89	76.26	80.61	85.44
3.93	38.75	44.88	50.02	54.13	58.99	62.40	66.71	70.63	74.92	79.16	80.26
4.14	37.51	03.00	48.43	52.34	56.39	60.19	65.12	69.05	73.17	78.00	82.56
4.51	36.28	42.31	46.78	50.79	50.99	59.09	63.17	66.71	71.25	75.51	80.26
4.89	34.42	40.28	44.65	48.67	52.52	56.85	60.70	64.36	68.51	72.96	77.96
5.28	32.57	38.26	42.52	46.24	49.92	54.05	57.87	61.26	65.30	69.88	75.08
5.65	31.34	35.99	40.08	43.51	46.90	50.89	54.81	58.33	62.68	67.27	72.78

These values are virtually identical to the mass-dependent data. For a graphical comparison, both group 8

data sets were plotted. This group was chosen because it had the largest variation between the two methods. The lines are almost indistinguishable as shown in Figure 3-13.

SBD direct energy calibration

For reasons of clarity, the following terms are defined:

Corrected Energy: Actual fission fragment energy (true energy)

Apparent Energy: Energy signal from SBD

Pulse Height Defect: Difference between true and apparent energy

Several steps are needed in order to calibrate the SBD signal to the actual fission fragment energy. First, the SBD channel data must be converted into the apparent energy of the fragments. Then, the pulse height defect (PHD) must be quantified. By adding the PHD to the apparent energy, the corrected particle energy is obtained.

The SBD signal represents the apparent energy of the particles. By calibrating the SBD (either by use of alpha particles or another method), the signal yields the energy collected by the electrodes in terms of ion-hole pairs. The uncollected, or "lost" ions account for the PHD. There are several methods used to calibrate the SBD. Typically, the signals from two or more different energy alpha particles
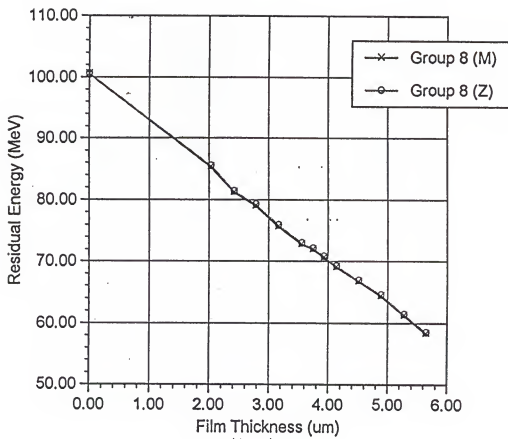
Figure 3-13: Comparison of results using Schmitt's method
and modified Schmitt's method for Group 8 data.

are used. However, since alpha particles are usually only 3 - 6 MeV, extrapolating this out beyond 100 MeV could lead to large errors. Accelerated light nuclei could also be used, but this is not practical in this work. The method used employed Schmitt's formula.

Calibration of the SBD channel data into apparent energy

The steps used are given below:

I. Using the scheme developed by Schmitt et al [36], determine the actual energies of the 11 groups for the unattenuated source (no films).

II. Subtract the PHD for each group for the unattenuated spectrum. This yields the apparent energy for the unattenuated spectrum.

III. Perform a linear fit on the data to yield the formula for E(apparent) as a function of channel data.

$$E_a(Ch) = m*Ch + b,$$

Where m is the slope and b is a constant.

I. This procedure was given in the previous section. For convenience, the 11 group unattenuated spectrum results are summarized below:

Group   Corrected Energy (MeV)

1	64.7
2	73.4
3	80.0
4	84.8
5	89.2
6	92.8
7	95.7
8	100.5
9	104.1
10	108.7
11	114.8

II. In order for this to be related to the SBD signal, these values must be converted into apparent energies. This is done by subtracting the PHD. The 11 group PHD data [37-40] for an unattenuated spectrum, along with the subsequent apparent energies are given below:

Group	PHD (MeV)	Apparent Energy
1	8.0	56.7
2	7.8	65.6
3	8.1	71.9
4	8.0	76.8
5	7.8	81.4
6	7.0	85.8
7	6.2	89.5
8	5.8	94.7
9	5.4	98.7
10	5.0	103.7
11	4.2	110.6

III. A linear fit to this data yields the final apparent energy relationship for the detector:

2) $E_a(Ch) = 0.5614*Ch + 3.76$ (MeV)

Pulse height defect quantification

The PHD for heavy ions is defined as the difference in signal between a heavy ion and a light ion (alpha particle) of equivalent energy. The PHD of light ions is small and assumed to be negligible. There are several factors

contributing to the PHD. Among these factors are: loss of
energy in the detector window, nuclear collisions (primarily
at the end of the particle track), and ion-hole
recombination in the semiconductor. These different factors
will be briefly examined below.

Loss of Energy in the Detector Window. In order to
create the electric field necessary for the operation of the
semiconductor, a layer of conductor (gold in this case) is
deposited on the entrance window. This layer is kept as
thin as possible to avoid significant energy degradation of
the particles. For the SBD used, the gold layer was about
20 nm thick [41]. The energy loss in this layer is fairly
small and for fission fragments will be roughly 0.5 MeV.

Nuclear Collisions. Nuclear collisions are nucleus-
nucleus interactions involving the fission fragment and
target atom. This typically displaces the target atom from
the semiconductor matrix. In a semiconductor, this results
in several energy loss mechanisms causing a loss of SBD
signal. First, the initial energy used in displacing the
atom from the matrix is not used directly to raise atoms
into the conduction band (although there is a secondary
effect from the target atom energizing the electrons).
Second, the void left in the matrix can "trap" an electron
or hole thus reducing the signal. Third, the target atom
eventually locates in another area of the semiconductor.

This creates another site for an electron or hole to become trapped.

Nuclear collisions are prominent at the end of the fragment range. For fission fragments at full energy, this accounts for less than 1 % of the energy loss. This percentage increases as the fragment energy is degraded. Below several MeV, it becomes the dominant source of energy loss.

Since the effect of nuclear collisions at higher energies is very small, the overall effect in the semiconductor can be considered to be independent of incoming particle energy. This will be the case unless the incoming particle is severely degraded in energy (down to several MeV).

The overall effect of nuclear collisions is difficult to quantify theoretically. This is because most of the energy transferred to the target atoms will raise electrons into the conduction band, thus contributing to the signal. However, the resulting defects in the semiconductor matrix will create electron-hole recombination sites, thus reducing the signal. Experimental measurements have estimated that the PHD from nuclear collisions is roughly 1.5 - 2.5 MeV [37].

Charge Recombination. Charge recombination occurs in a semiconductor when an electron fills a hole before it reaches the electrode. This is much more prevalent with heavy ions because of the higher density of electrons and holes created. Another factor is the strength of the electric field in the semiconductor. This determines the drift velocity and thus the time that the electrons and holes are in "contact" in the semiconductor.

Measurements have been made for a similar detector using various accelerated charged particles (in the mass range of fission fragments). This effect is considerably larger than the other two and can result in a defect of up to 5 MeV [38].

These three factors will be combined into an overall PHD. The PHD data will be interpolated from previous research [37-40]. This amount will then be added to the SBD signal to obtain the "true" residual energy measurement.

Equation 2 yields the apparent energy for the SBD. This is independent of group, the thickness of film that the particles pass through, or the type of ion. However, the information that is needed is the corrected, or actual energy of the particles. To get this, the PHD must be added to the apparent energy. Therefore, the PHD as a function of group and energy is required.

The PHD for each of the 11 groups was approximated linearly over the energy range of interest for each group according to Equation 3. The data is given below:

3) $PHD_{GRP}(E_a) = m*E_a + b$

Group	m	b (MeV)
1	0.0615	3.6
2	0.0556	3.6
3	0.0551	3.5
4	0.0537	3.4
5	0.0523	3.2
6	0.0466	2.8
7	0.0358	2.8
8	0.0275	3.0
9	0.0212	3.1
10	0.0165	3.1
11	0.0108	2.9

Because the corrected energy is the sum of the apparent energy and the PHD, adding E_a to equation 3 yields the corrected energy.

4) $E_c = (1 + m)E_a + b$

By combining Equation 4 and Equation 2, the result is the SBD energy calibration:

5) $E_c = (1 + m)(0.5614*Ch + 3.76) + b$

Combining the constants yields:

6) $E_c = m'*Ch + b'$

The 11 group m' and b' constants are given below:

Group	m'	b'
1	0.5959	7.6
2	0.5926	7.6
3	0.5923	7.5
4	0.5915	7.4
5	0.5908	7.2
6	0.5876	6.7
7	0.5815	6.7
8	0.5768	6.9
9	0.5733	6.9
10	0.5707	6.9
11	0.5675	6.7

Plots of the 11 group apparent energy vs corrected energy are given in Figures 3-14 to 3-17. The curve for alpha particles (no PHD) is shown also. The difference between the 11 group lines and the alpha particle line is the PHD.

The plot of the 11-group corrected energy vs the film thickness is shown in Figure 3-18. These values are very close to the data resulting from Schmitt's method, mostly within a few tenths of an MeV. Plots showing the corrected energy vs the film thickness for both methods for groups 3 and 9 (heavy and light fragment peaks) are shown in Figure 3-19. The similarity leads to the conclusion that either method is valid. Since Schmitt's method is a formula that can readily be used in an analysis program, it is the preferable method. However, since the fission fragment energy loss and luminescence signal tend to be Z-dependent, the modified Schmitt method will be used.

Time-of-Flight Calibration

Using the results from the SBD calibration, estimates of the energies of the various groups are made. Using the approximate group masses, the group velocities and time-of-flights for the 2 film system are given below (30.2 cm flight path).
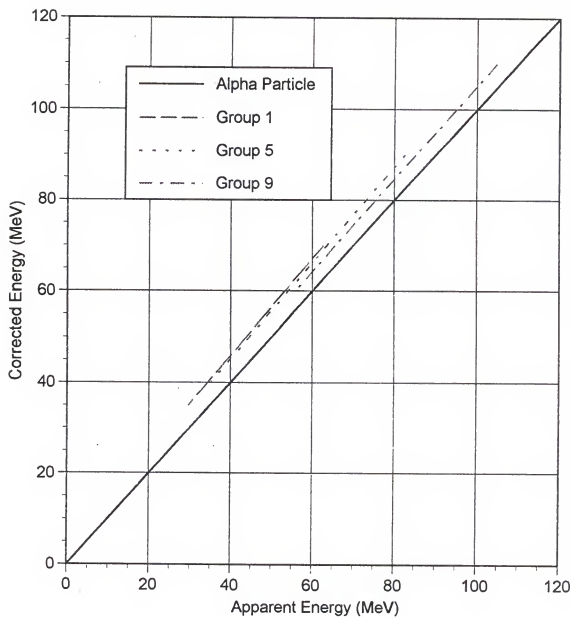
Figure 3-14: Corrected vs. apparent energy for Groups 1, 5, and 9.
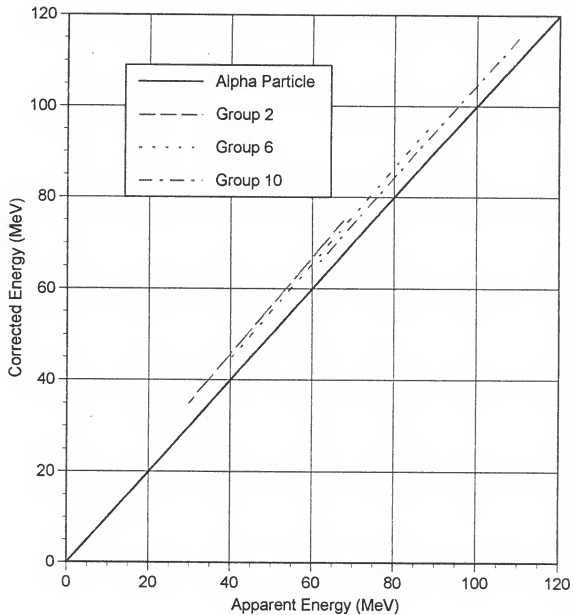
Figure 3-15: Corrected vs. apparent energy for groups 2, 6, and 10.
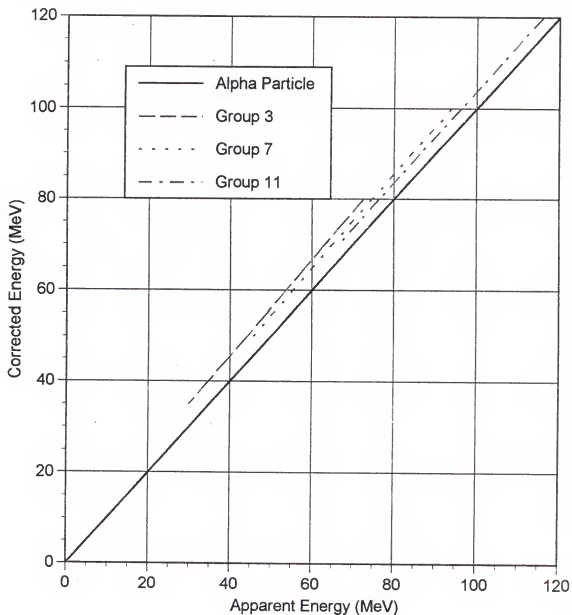
Figure 3-16: Corrected vs. apparent energy for groups 3, 7, and 11.
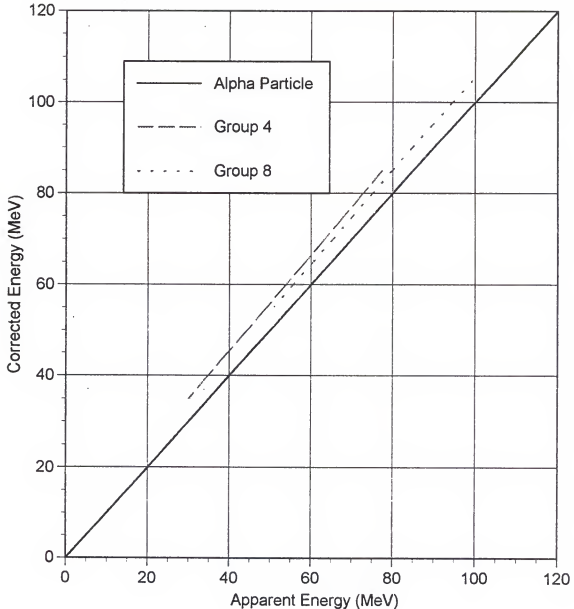
Figure 3-17: Corrected vs. apparent energy for group 4 and group 8.
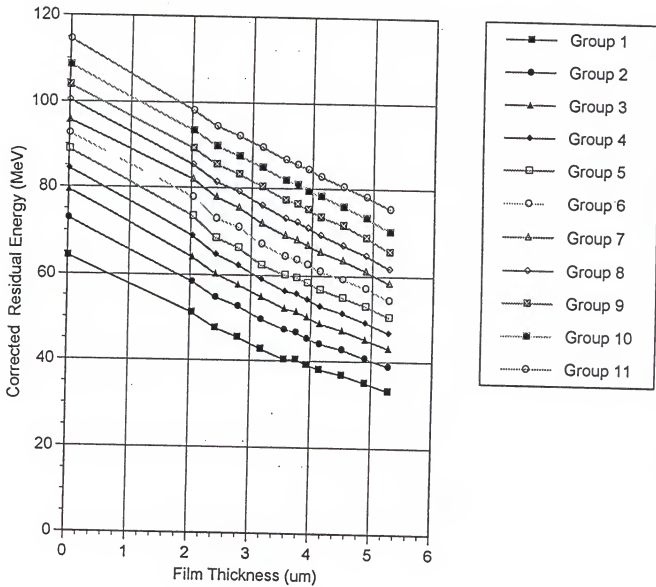
Figure 3-18: 11-Group residual energy vs. film thickness.
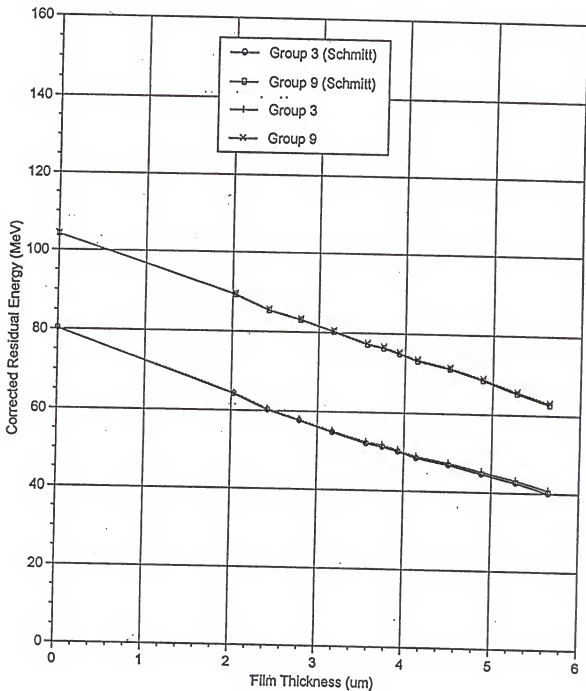
Figure 3-19: Comparison of corrected residual energy vs.
film thickness using Schmitt's method and calculation.

Group	Velocity (cm/ns)	Time-of-Flight (ns)
1	0.797	37.9
2	0.873	34.6
3	0.926	32.6
4	0.974	29.6
5	1.02	29.6
6	1.09	27.7
7	1.17	25.9
8	1.22	24.8
9	1.27	23.8
10	1.32	22.8
11	1.40	21.5

Fitting this to the TOF raw data, yields the graphs in Figures 3-20 and 3-21 for the TOF 1A-3A and TOF 1B-3B spectra, respectively.

A measure of the uncertainty in the time signals can be found by viewing the difference between TOF 1A-3A spectrum and TOF 1B-3B spectrum (TOF-A is offset) seen in Figure 3-22 (each measurement is independent of the other). This shows a region, or wing, beyond the normal distribution. This is due to electronic noise in the 1B timing signal causing a slight delay in the start signal for some events. To eliminate these data points, and also to eliminate data for which there was no time signal, all data for which the TOF's deviated by more than 20 % were not included in the
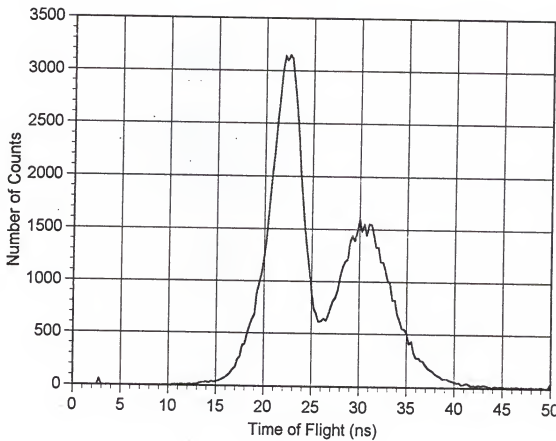
Figure 3-20: TOF 1A-3A Spectrum for 2 TFD system.
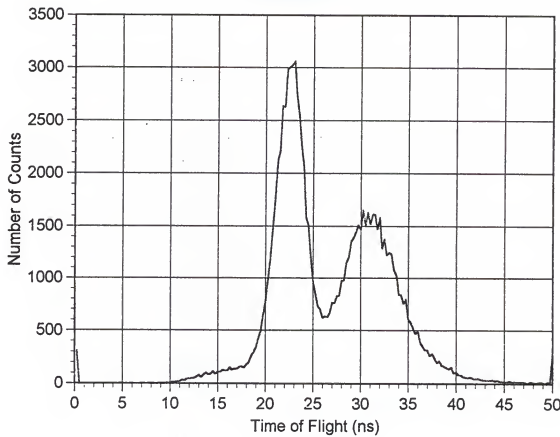
Figure 3-21: TOF 1B-3B Spectrum for 2 TFD system.
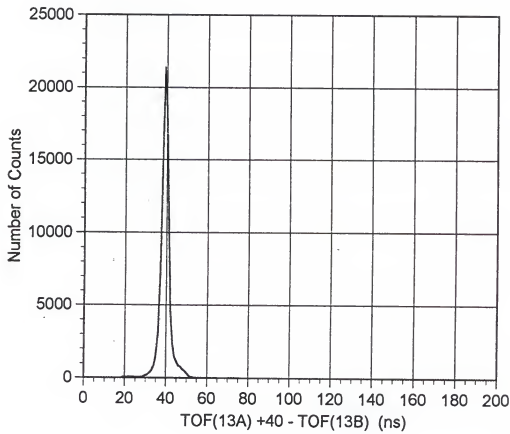
Figure 3-22: Spectrum for TOF 1A-3A minus TOF 1B-3B for 2 TFD system.

calculations. This level was well beyond the data spread expected from a normal distribution. In order to increase the time resolution, the remaining TOF signals were averaged. This produced the final calibrated data shown in Figure 3-23.

Thin Film Detector Calibration

Calibrating the thin film detectors is a two-step process. First, the output from each pair of photomultipliers for each film had to be matched (film 1A should equal film 1B, etc). Since the individual channel data is saved on the computer, any offset or gain can be added after the data has been collected. Then, the summed signal for the first film must be normalized to match that of the third film. The outputs for each of the individual PMT's are shown in Figures 3-24 to 3-27, followed by the summed outputs in Figure 3-28 and 3-29. The summed outputs include a geometric correction factor, described below:

Geometric Correction. The luminescence signals have been modified to account for the geometric efficiency. Using the Monte Carlo program MCNP, a mockup of the thin film and photocathode geometry was made. An isotropic point source was placed at the center of the film (X = 0) and efficiency calculations
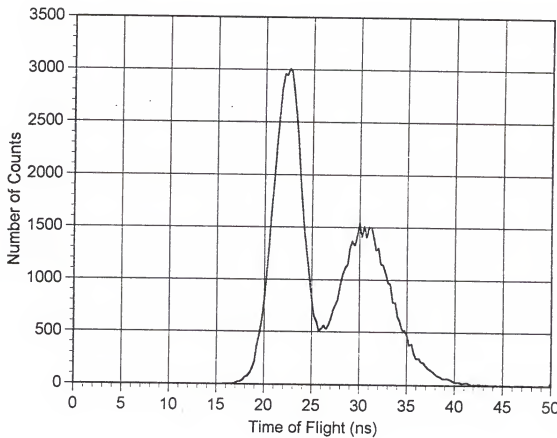
Figure 3-23: Averaged TOF 1-3 Spevtrum for 2 TFD system.
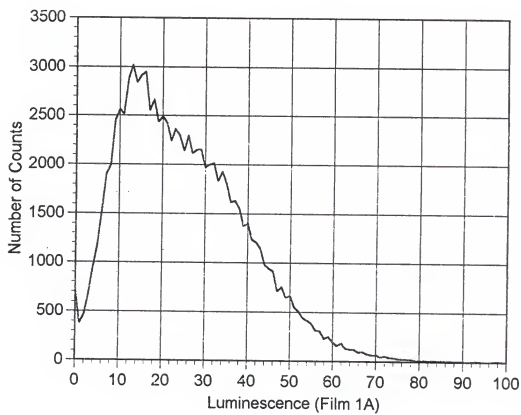
Figure 3-24: Film 1A Output for 2 TFD system.
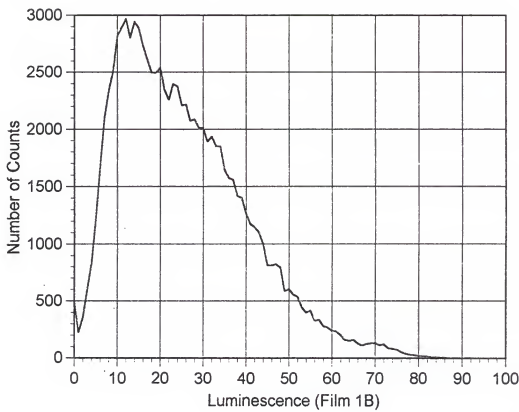
Figure 3-25: Film 1B Output for 2 TFD system.
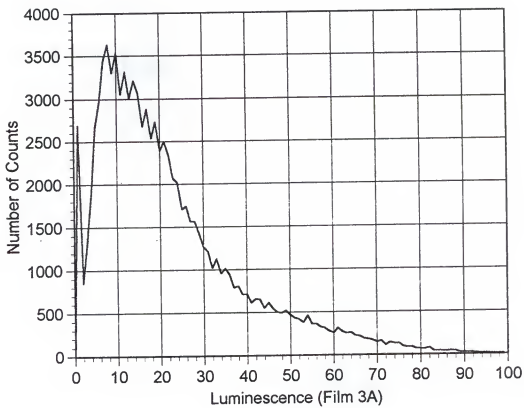
Figure 3-26: Film 3A Output for 2 TFD system.
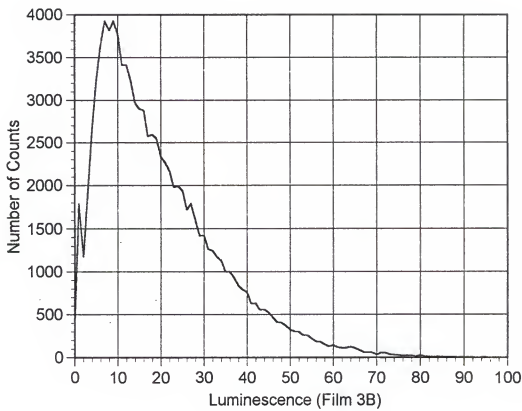
Figure 3-27: Film 3B Output for 2 TFD system.
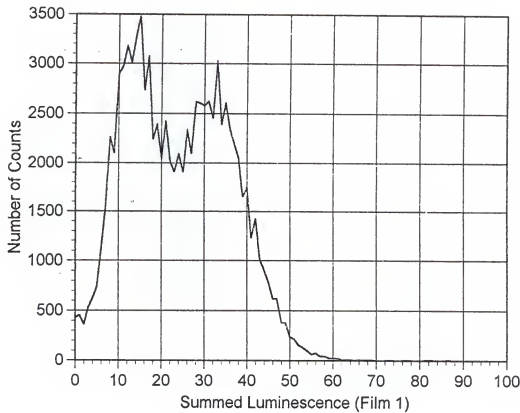
Figure 3-28: Film 1 Summed Output for 2 TFD system.
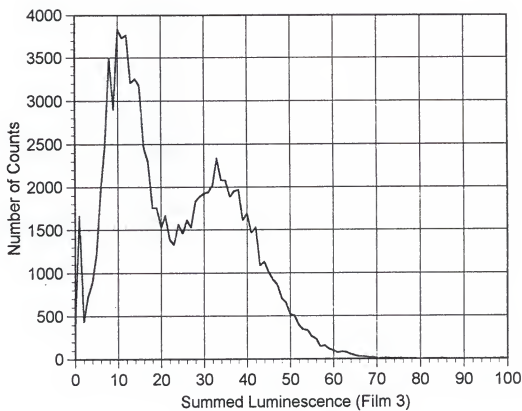
Figure 3-29: Film 3 Summed Output for 2 TFD system.

(fraction of particles striking each photocathode surface) were made. This was repeated as the source was moved toward photocathode 1A. By adding the efficiencies, ($\epsilon(x) = \epsilon 1A(x) + \epsilon 1B(x)$) the overall geometric efficiency vs position is obtained. This can also be expressed in terms of the ratio of the efficiencies $R(x) = \epsilon 1B(x)/\epsilon 1A(x)$ (with $R(x) < 1$), which is equivalent to the ratios of the luminescences, since:

$$L1A(x) = \epsilon 1A(x) * Lo \quad (Lo = \text{Total Luminescence})$$

$$\frac{L1B(x)}{L1A(x)} = \frac{\epsilon 1B(x) * Lo}{\epsilon 1A(x) * Lo} = \frac{\epsilon 1B(x)}{\epsilon 1A(x)} = R(x)$$

Therefore, by taking the ratio of the luminescence signals for each film, an estimate of the efficiency ratio $R(x)$ can be made. By inverting this formula, $x(R)$ is found, and an estimate of the interaction position x is determined. With an estimate of x, the efficiency can be calculated using the previously determined $\epsilon(x)$. By multiplying the summed film luminescence by the ratio $\epsilon(0)/\epsilon(x)$, the signal is "corrected" to account for different geometric efficiencies. All these steps have been combined into one formula to determine the geometric correction value VL with the variable being the ratio of the signals ($R < 1$). Therefore, L1(geom. corrected) = [L1A + L1B] * VL1. The formula is given below:

$$VL = 0.22302 + 3.6672 * R - 8.2209 * R^2 + 10.608 * R^3$$
$$- 7.3836 * R^4 + 2.107 * R^5$$

In summary, the VL(R) function is a ratio of the geometric efficiency at the center of the film divided by the geometric efficiency at the interaction position. The interaction position is determined by the ratio of the luminescences from each photomultiplier. By multiplying the summed luminescence by VL, the output is corrected for the different geometric efficiency resulting from the interaction position. A plot of this function is shown in Figure 3-30. The overall effect on the summed luminescences results in a decrease in the signal of roughly 3 percent.

Nuclear Charge Determination

Using the previous calibrated data, a method for the determination of fission fragment nuclear charge (Z) is found.

Initial Charge Estimate

Of the three parameters (luminescence, TOF, and residual energy), the nuclear charge has the largest impact on the luminescence. Therefore, a direct correlation between the TFD signal and Z will be made. This will serve as a starting point for the Z calculation. Using the
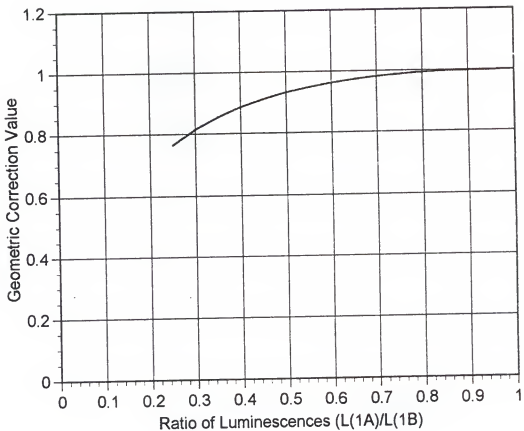
Figure 3-30: Plot of VL function vs. ratio of luminescence signals (R).

knowledge that the most probable Z values for ^{252}Cf fission are 42 and 56 with a valley at Z = 49, the luminescence plot is converted into a Z plot. This is shown in Figure 3-31.

Analysis of Initial Charge Uncertainty

To determine the degree to which this data represents the actual nuclear charge, a series of analyses were made. First, a "slice" of data was taken for Z = 42, 49, and 56 (using the approximate Z's obtained from the luminescence plots). This is shown in Figure 3-32. Then, the E_r plots for these slices of data were obtained. These plots were then split up into three regions approximately equal in size consisting of a lower, middle and upper energy area, as shown in Figures 3-33 to 3-35. Then, the TOF data was obtained for each of these regions, and plotted. The plots are shown in Figures 3-36 to 3-38.

In any distribution, there will be a normal spread in the data. If the spread in the E_r graphs was the result of a statistically random distribution, then the data at the upper end of the energy plot would be just as likely to give a high TOF as the data in the lower end of the energy spectrum. Therefore, the three resulting TOF plots for each Z should show little discrepancy. However, if the spread in the Z plot is not mainly the result of statistical variation, then there may be a large portion of the original Z from particles several charge units away. If this is the
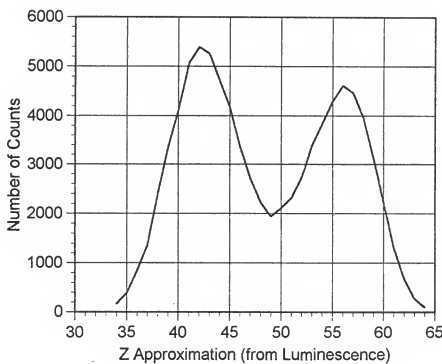
Figure 3-31: Luminescence plot converted into Z plot
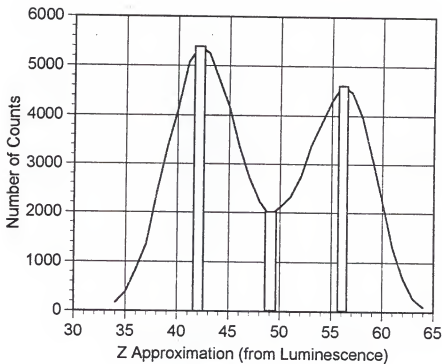
Figure 3-32: Z = 42, 49, and 56 slices of data used for analyses.
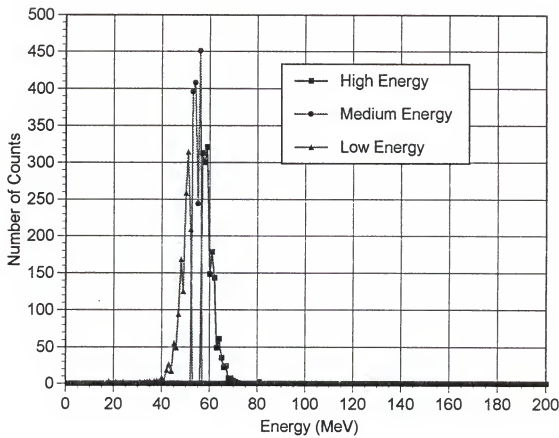
Figure 3-33: E_r data for Z = 56.
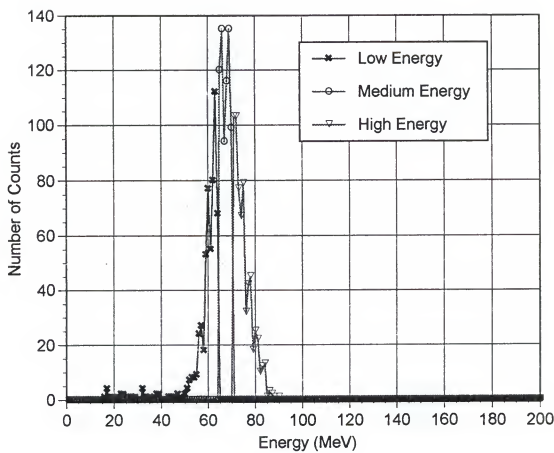
Figure 3-34: E_r data for Z = 49.
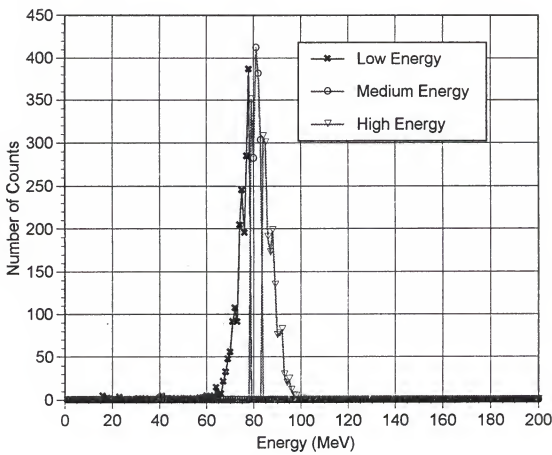
Figure 3-35: E_r data for Z = 42.

case, then there would be a large shift in the TOF graphs.
This is seen in Figures 3-36 to 3-38.

Quantification of Parameter Uncertainties

Using the luminescence data as a starting point (Z_o),
modifications will be made to take into account the E_r and
TOF data. In order to do this a measure of resolution
(full-width-half-maximum, FWHM) for individual particles
must be made for the E_r and TOF data. Using the ^{252}Cf data
by taking a "slice" of one variable and looking at the FWHM
of another variable would incorporate the FWHM of two
parameters into the measurement. Since a source of
monoenergetic heavy ions (accelerator) was not available,
another method must be used.

An approximation of the energies and times of each Z
are made. Using the estimated yields for the different
nuclear charges [32], a normal distribution is assumed for
each Z. The distributions are then summed to give a fission
spectrum. The FWHM for the various charges are then varied
until the resulting graph approximated the measured data.
The Z locations, along with the estimated yields are shown
in Figures 3-39 and 3-40. The resulting spectra are shown
in Figures 3-41 and 3-42. Since the parameter used was the
deviation from the average, the appropriate measure is the
half-width-at-half-maximum (HWHM). The HWHM for the E_r plot
was a constant at +/- 5 channels, while for the TOF data it
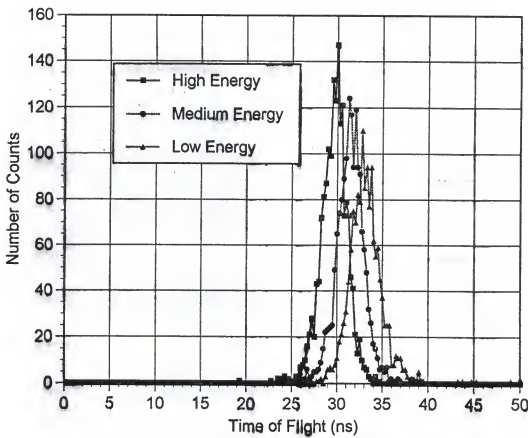
Figure 3-36: TOF data for the different energy regions for
Z = 56.
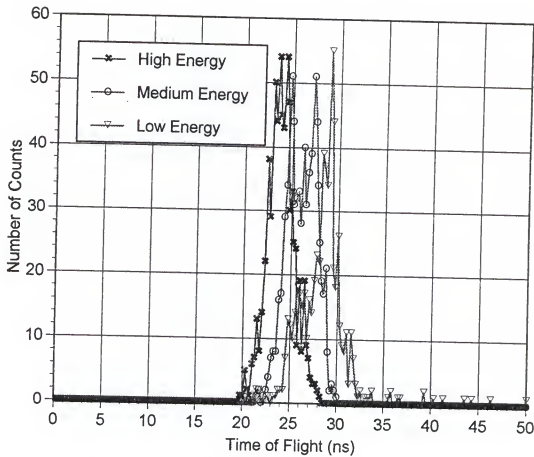
Figure 3-37: TOF data for the different energy regions for Z = 49.
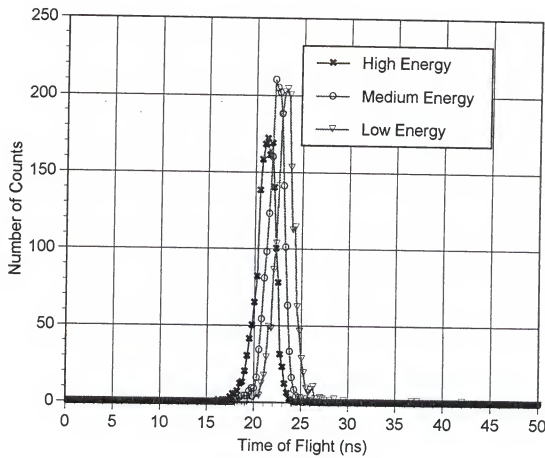
Figure 3-38: TOF data for the different energy regions for
Z = 42.
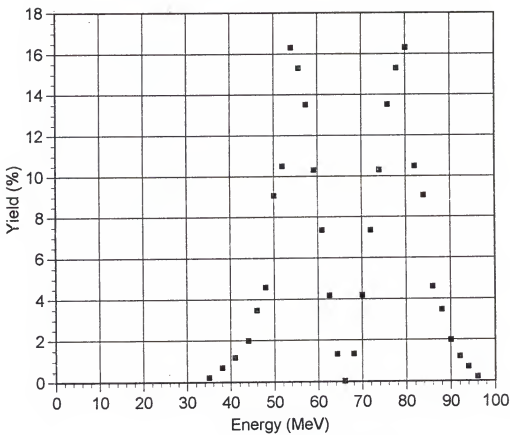
Figure 3-39: Estimated Z location and yield for E_r.
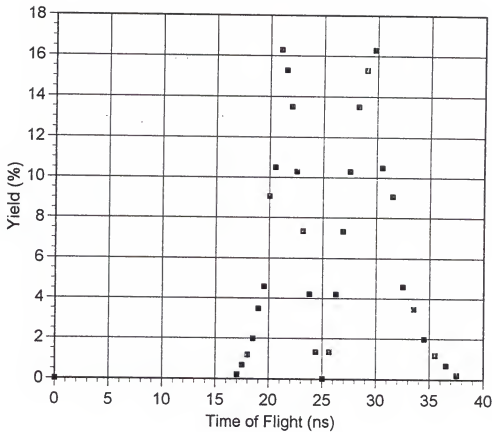
Figure 3-40: Estimated Z location and yield for TOF graph.
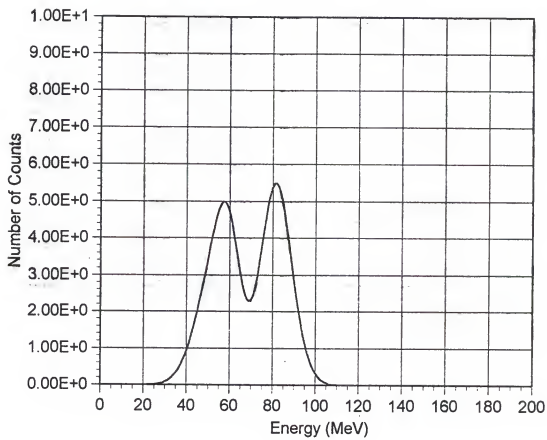
Figure 3-41: Residual energy graph resulting from the
estimated uncertainties.
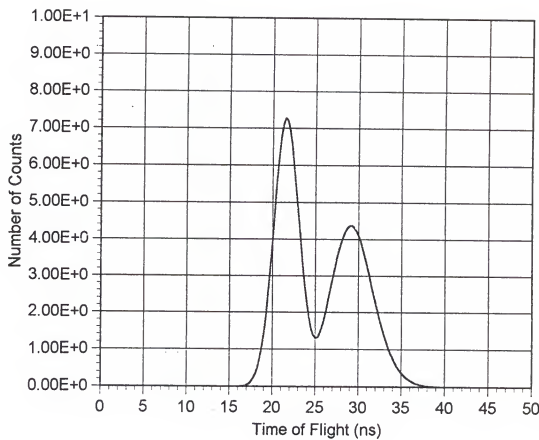
Figure 3-42: Time-of-Flight graph resulting from the estimated uncertainties.

was a constant fraction of the signal at +/- 0.05*(channel number).

Charge Determination Algorithm

In order to make "corrections" to the Z_o data, correlations between the nuclear charge and E_r and TOF are needed. Contour plots of E_r vs Z_o and TOF vs Z_o are shown in Figures 3-43 and 3-44 along with a line connecting the ridge of the graphs. Using this line as a conversion factor, the functions $E_r(Z_o)$ and $TOF(Z_o)$ are found. Using these functions, an energy and time based on the luminescence signal is determined. Using the difference between the predicted and measured E_r and TOF, "corrections" are made in the nuclear charge of an amount equal to the difference between the predicted and measured value divided by the signal HWHM. This is accomplished as follows:

1) Using the luminescence signal, estimate Z_o.

2) Estimate $E_r(Z_o)$.

3) $\Delta Z_1 = [E_r(Z_o) - E_r(measured)] / Uncert.(E_r)]$

4) $Z' = Z_o + \Delta Z_1$

5) Estimate $TOF(Z')$

6) $\Delta Z_2 = [TOF(measured) - TOF(Z_o) / Uncert.(TOF)]$

7) $Z'' = Z' + \Delta Z_2$
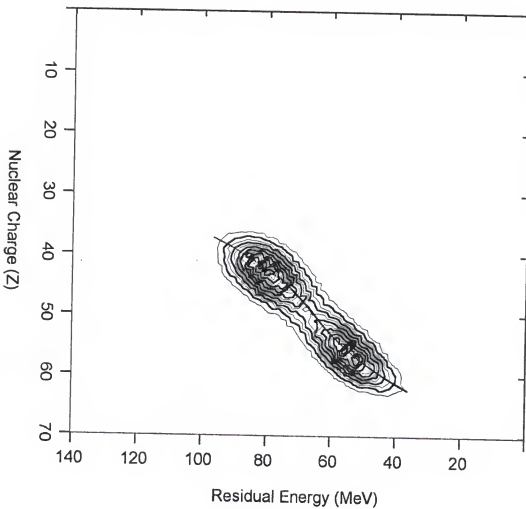
Figure 3-43: Contour plot of E_r vs. Z. A line has been drawn across the ridge for a visual aid.
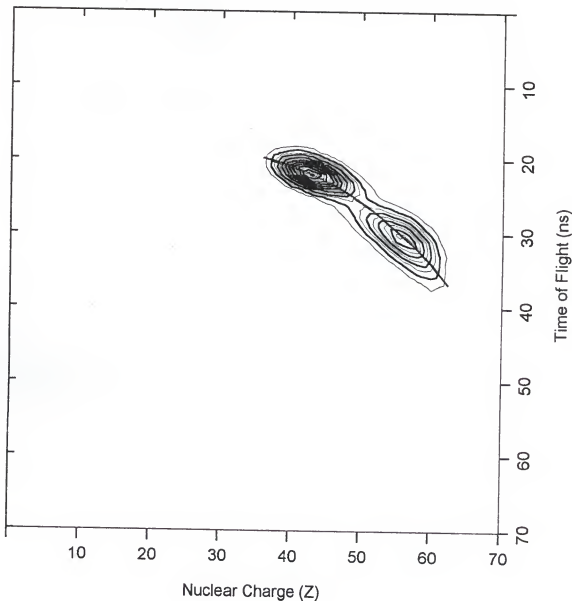
Figure 3-44: Contour plot of TOF vs. Z. A line has been drawn across the ridge for a visual aid.

Analysis of Corrected Charge Uncertainty

Plotting Z_o, Z', and Z'' shows an increase in the charge resolution as evident in the peak-to-valley ratios in Figure 3-45. Repeating the previous set of graphs (Figures 3-31 to 3-37), slices of data were taken for $Z'' = 42$, 49, and 56, as shown in Figure 3-46. The residual energy was plotted for each of these slices and divided up into three regions shown in Figures 3-47 to 3-49. Plotting the TOF for each region results in graphs that show virtually no discrepancy among each region. This is shown in Figures 3-50 to 3-52. This is a very good indication that the spread in the data is due to normal variation. Using the previous method to estimate an uncertainty, the HWHM for the charge calculation is 2.1. Plotting the luminescence, E_r, and TOF data for each charge unit yields the graphs in Figures 3-53 to 3-58.
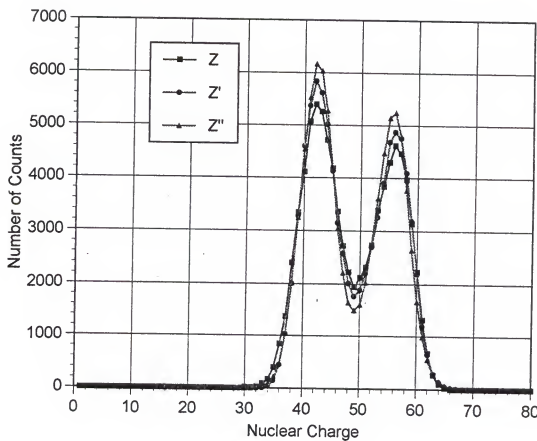
Figure 3-45: Nuclear charge estimates Z, Z', and Z".
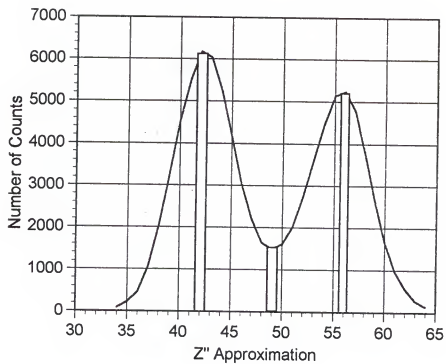
Figure 3-46: Slices of data taken for Z" = 42, 49, and 56.
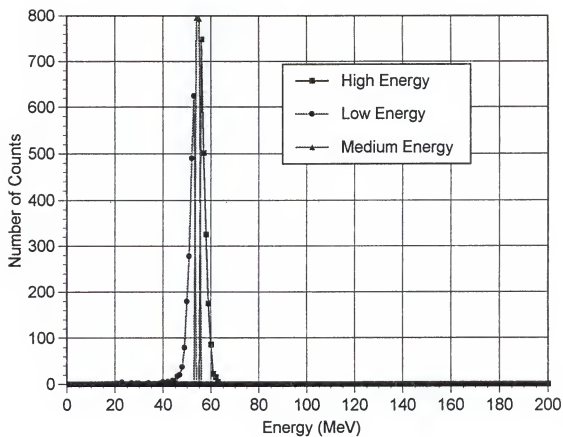
Figure 3-47: Three regions for the E_r plot for $Z" = 56$.
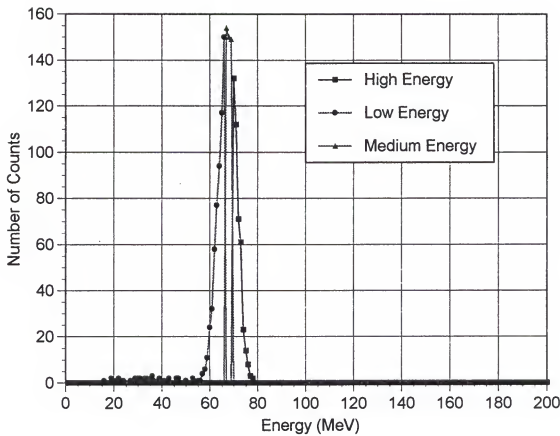
Figure 3-48: Three regions for the E_r plot for $Z'' = 49$.
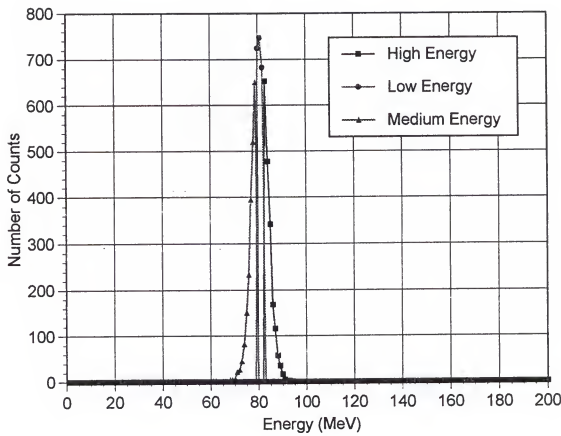
Figure 3-49: Three regions for the E_r plot for $Z'' = 42$.
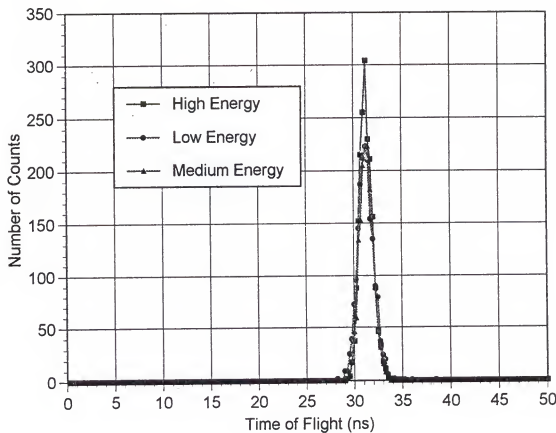
Figure 3-50: TOF data for the E_r regions for Z" = 56.
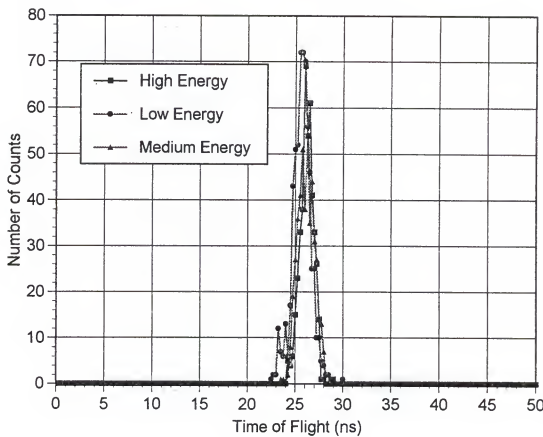
Figure 3-51: TOF data for the E_r regions for $Z'' = 49$.
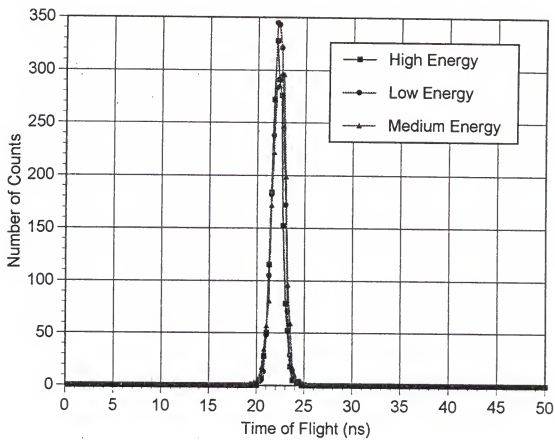
Figure 3-52: TOF data for the E_r regions for $Z'' = 42$.
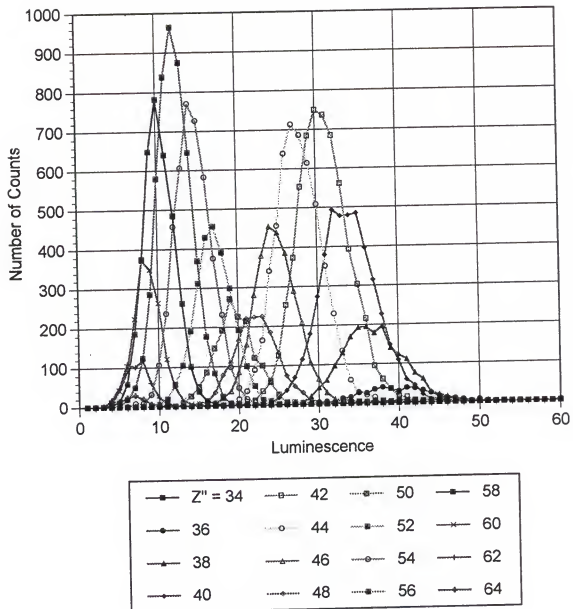
Figure 3-53: Luminescence plots for even Z" elements.
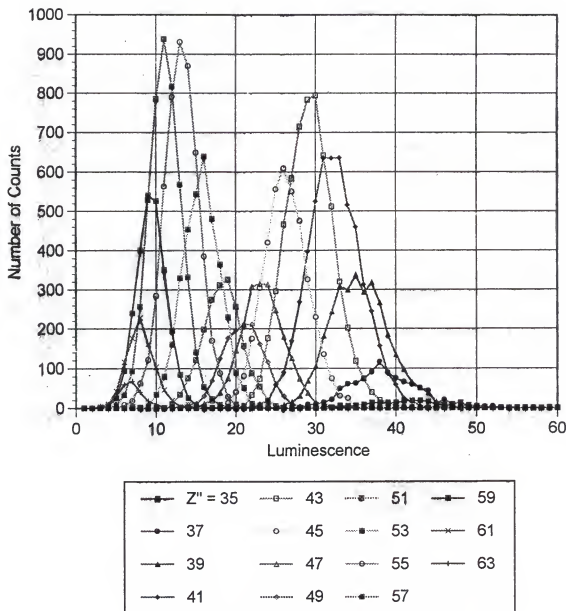
Figure 3-54: Luminescence plots for odd Z" elements.
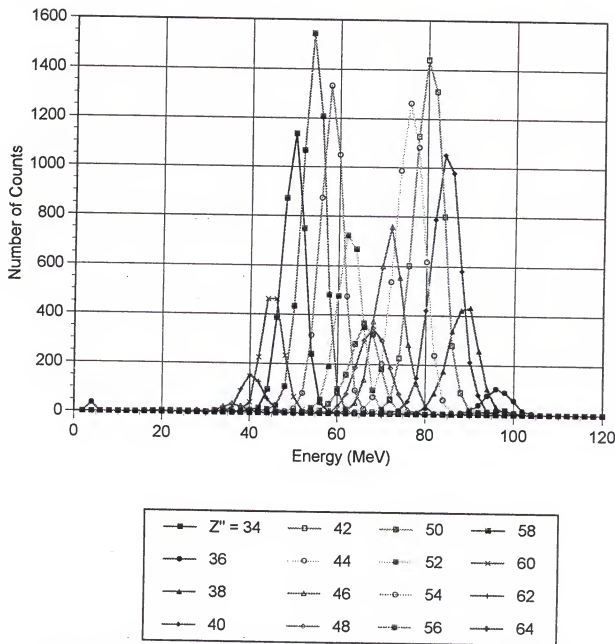
Figure 3-55: Residual energy plots for even Z" elements.
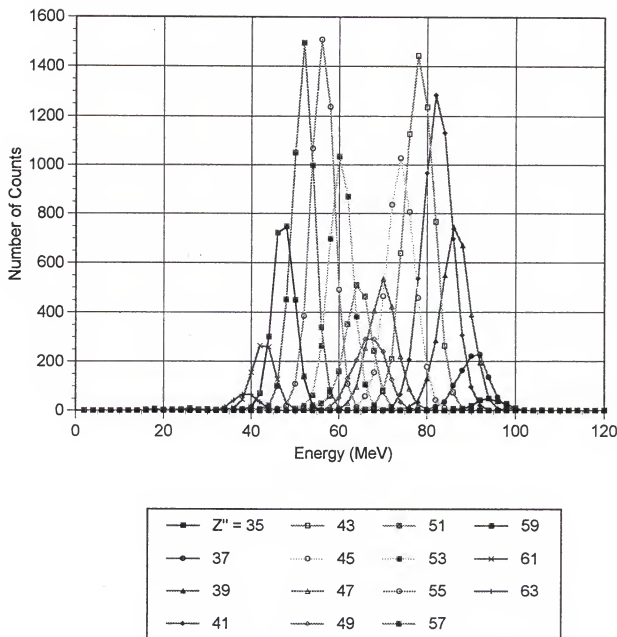
Figure 3-56: Residual energy plots for odd Z" elements.
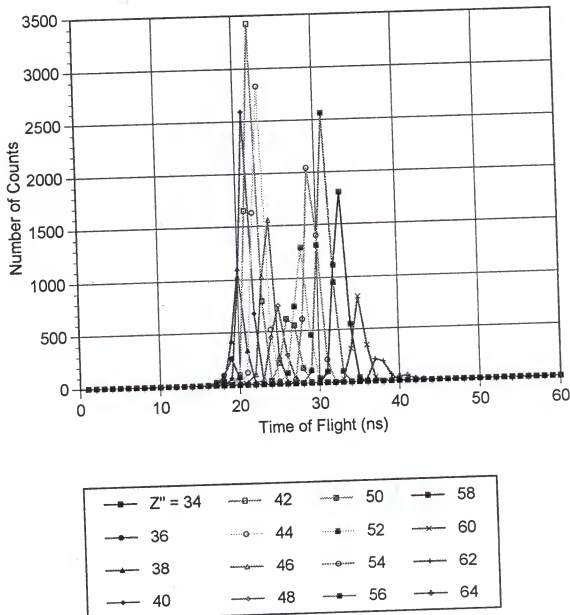
Figure 3-57: Time-of-flight plots for even Z" elements.
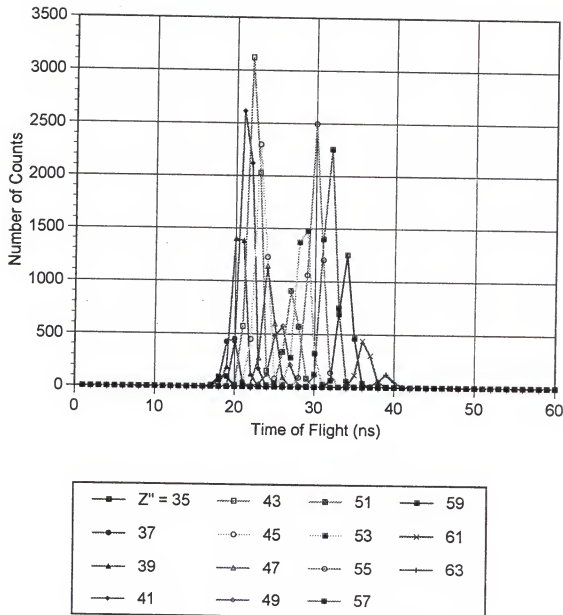
Figure 3-58: Time-of-flight plots for odd Z" elements.

CHAPTER 4
CHARGE STATE EQUILIBRIUM EFFECTS

Background/Theory

When heavy ions, such as fission fragments, pass
through material, there is a continual gain and loss of
electrons. Electrons are captured by the ion by Coulomb or
radiative capture, and are lost to the target via excitation
to the target continuum. After passing through a certain
amount of material, less than the thickness of the films
used in this work [42], a charge state equilibrium develops.
At this point, the ionic charge of the incoming ion is
irrelevant to the final charge state.

Originally, charge state equilibrium values were mod-
elled as a function of the ion's Z and energy. Two empiri-
cal formulas for the fractional charge state of ions passing
through carbon foils are given below:

$$q/Z = (1 + X^{-5/3})^{-3/5} \qquad 0.3 < q/Z < 0.7 \qquad [43]$$
$$q/Z = 1 - \exp(-1.25 + 0.32*X - 0.11*X^2) \qquad [44]$$

$$X = v/(v'Z^{0.45}) \qquad\qquad v' = 3.6 \times 10^8 \text{ cm/s}$$

These tended to reproduce the data fairly well within the framework of the experimental conditions (primarily passage through a carbon foil). Numerous experiments [42,43,45-59] have shown that charge states for ions passing through various metal foils are generally independent of the target material (for a constant Z and energy).

A series of experiments [52] demonstrated a significant (as much as 20 %) difference in stopping power between solid and gaseous targets of adjacent Z. This has been attributed to different charge state equilibria for the two different media. This can be explained as follows. In a collision, some of the inner shell electrons of the transiting ion will not be ionized, but will merely be raised to an excited energy state. In a solid, the ion's next collision will most likely occur before the electron has been able to de-excite. However, in a gas, there is a longer time between collisions, and the electron may relax back into the inner shell of the ion before the next collision. Thus, ions traversing a solid tend to have a higher ionic charge state than ions traversing a gas.

In addition to the solid/gas effect, it has been theorized that there is also a conductor/insulator effect for solids. That is, the conductivity of the target medium will have an effect on the charge state equilibrium. Electrons in the conduction band of a metal have a lower ionization potential than the outer shell electrons of a plastic insulator (NE-102). It is theorized that the electrons in

140

the conductor will be acquired more easily by the transiting ion. This would translate into a lower charge state for ions passing through a conducting media.

Experimental Setup

The system used will be the multiple TFD system previously described. Some of the slots of the dual-wheel chamber were filled with nickel foils, others were filled with VYNS films, and one slot of each was left empty. In this way, nickel, plastic, or no film could be placed in the ion beam without opening up the vacuum chamber.

With the first two TFD's raised, the Ni foil would be inserted. This results in the ion traversing, in order: Ni foil, TFD-3, and stopping in the SBD. By repeating this run with TFD-3 raised, the residual energy measurement would also be the energy of the particles entering TFD-3. Then an appropriate combination of TFD-1, TFD-2, and VYNS films would be substituted for the Ni foil to try and match the residual energy spectrum. Diagrams of these setups are shown in Figures 4-1 and 4-2. By matching the energy spectra of the two systems without TFD-3, this would show that the energies of the particles entering TFD-3 are the same. Then another run is made with TFD-3 inserted. Since luminescence output is dependent on the particles ionic charge [24], comparing the luminescences from TFD-3 would indicate a difference in the charge state equilibrium.
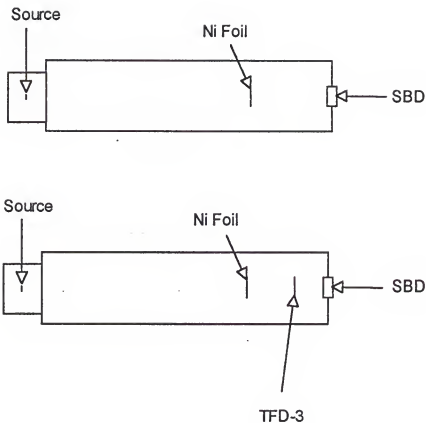
Figure 4-1: Setup for Ni film system.
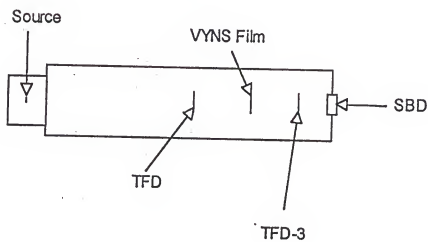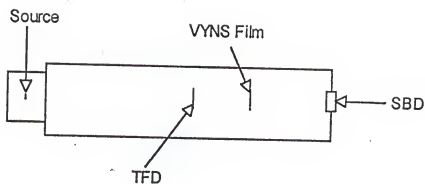
Figure 4-2: Setup for plastic film system.

The various runs previously described were made. For reference, the unattenuated spectrum (no plastic or Ni films) is shown in Figure 4-3. After the first set of nickel and plastic runs were made, it was discovered that for the same average energy loss, the ^{252}Cf peaks were closer together after the fission fragments passed through the Ni as opposed to the plastic films. As a result, matching the entire residual energy spectrum was not possible. Therefore, additional runs were made to try and match the energy loss of the light and heavy mass fragment peaks individually. A thinner plastic film is needed to match the light mass peak than to match the heavy mass peak. The appropriate films will be labelled Pl$_{thin}$ and Pl$_{thick}$ for the light mass and heavy mass peak respectively.

The energy spectra entering TFD-3 are shown in Figures 4-4 and 4-5. Figure 4-4 shows the energy spectra after the Ni and Pl$_{thin}$ films while Figure 4-5 shows the energy spectra after the Ni and Pl$_{thick}$ films. The energy separation between the light and heavy fragment peaks is about 2.5 MeV less in the Ni foil than in the plastic films.

The energy spectra exiting TFD-3 are shown in Figure 4-6 and 4-7. Once again, Figure 4-6 shows the energy spectra of the Ni and Pl$_{thin}$ film while Figure 4-7 shows the energy
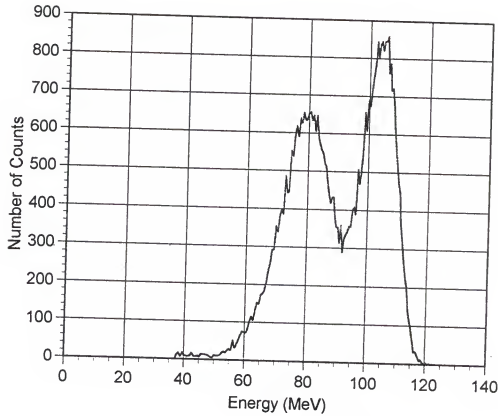
Figure 4-3: Unattenuated ^{252}Cf fission fragment spectrum.
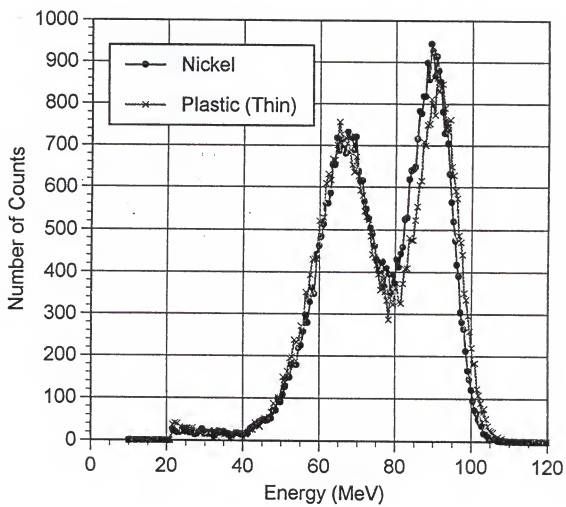
Figure 4-4: Energy spectra entering TFD-3 for Ni and Plastic$_{thin}$ films.
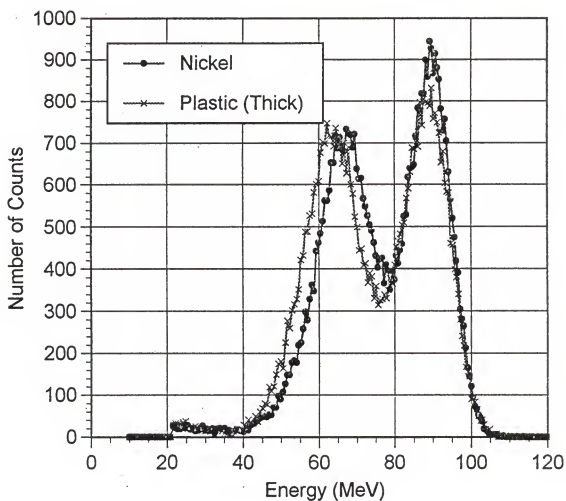
Figure 4-5: Energy spectra for particles entering TFD-3 for
Ni foil and Plastic$_{thick}$ film.
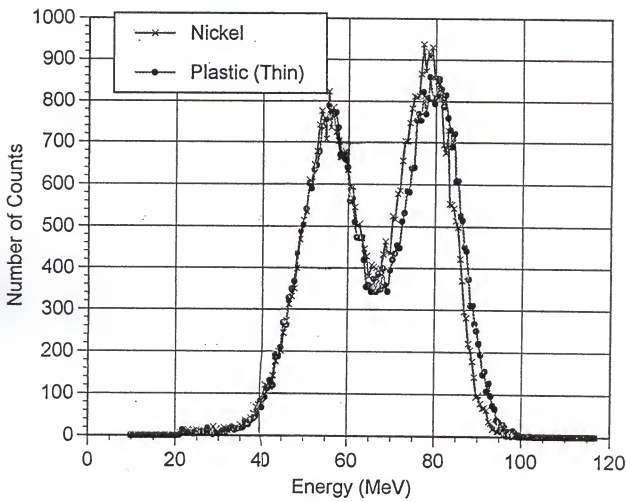
Figure 4-6: Energy spectra for particles exiting TFD-3 for
Ni foil and Plastic$_{thin}$ film.
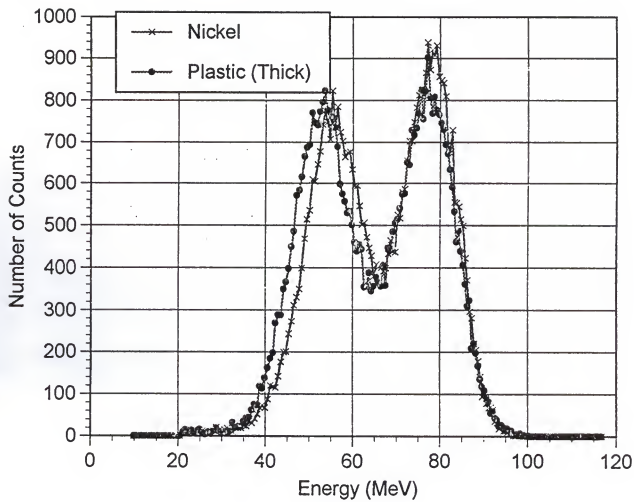
Figure 4-7: Energy spectra for particles exiting TFD-3 for Ni foil and Plastic$_{thick}$ film.

spectra from the Ni foil and Pl_{thick} film. The energy separation between the light and heavy mass fragments is 2.0 MeV smaller for the Ni foil as it is for the Pl_{thick} foil.

The luminescence graphs for the above runs are shown in Figures 4-8 and 4-9. Figure 4-8 gives the luminescence for the Ni foil and Pl_{thin} film while Figure 4-9 gives the luminescence for the Ni foil and Pl_{thick} film.

Charge State Equilibrium Discussion

Comparing the energy and luminescence graphs does appear to show a difference in the charge state equilibria between the Ni foil and plastic film. This is especially evident in the case of the low energy, heavy mass (M_H) peak.

The M_H peak energies entering TFD-3 were 67.1 and 66.4 MeV for the Ni and Pl_{thin} films, respectively (energies were determined using a normal fit to the peaks). The energies leaving TFD-3 were 55.7 and 55.6 MeV for the Ni and Pl_{thin} films, respectively. Therefore, the energies were almost identical for the low energy (M_H) peak. The luminescence output was significantly higher for the Pl_{thin} film (channel numbers 25.4 and 23.7 for the Pl_{thin} film and Ni foil, respectively).

Comparing the Ni foil and Pl_{thick} film yields similar results. The M_H peak energies entering TFD-3 were 67.1 and
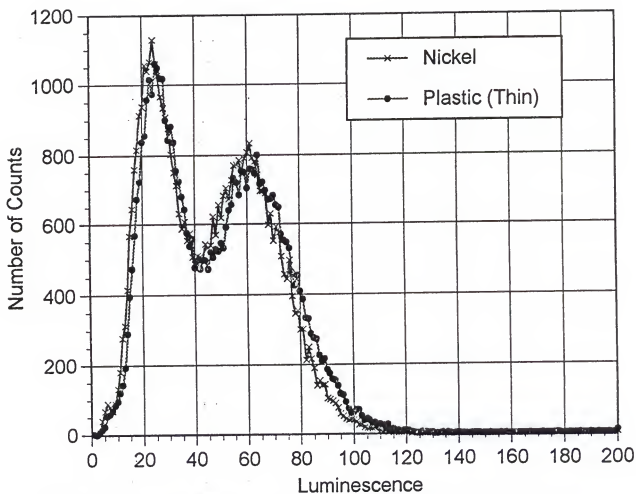
Figure 4-8: Luminescence spectra of TFD-3 for Ni foil and Plastic$_{thin}$ film.
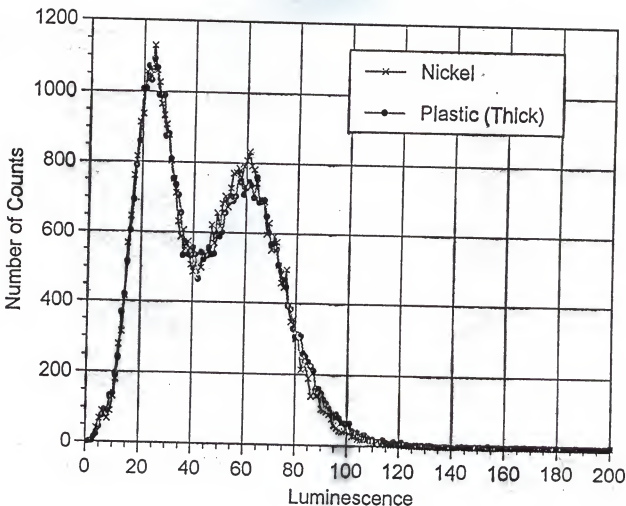
Figure 4-9: Luminescence spectra of TFD-3 for Ni foil and Plastic$_{thick}$ film.

63.3 MeV for the Ni and Pl_{thick} films, respectively. The particle energies exiting TFD-3 were 55.7 and 52.7 MeV for the Ni and Pl_{thick} films, respectively. Although the energies were significantly lower for the Pl_{thick} film, the luminescence peaks were virtually identical (23.9 vs 23.7 for Ni).

The high energy, light mass (M_L) peak energies entering TFD-3 were 89.6 and 91.3 MeV for the Ni and Pl_{thin} films, respectively. The energies leaving TFD-3 were 78.0 and 79.8 MeV for the Ni and Pl_{thin} films, respectively. Therefore, the energies were slightly higher for the plastic film. The luminescence output was significantly higher for the Pl_{thin} film (channel number 61.7 for the Pl_{thin} film and channel number 58.6 for the Ni foil). Since the particle energy at this peak were slightly higher for the plastic film, the difference in luminescence is not necessarily the effect of the charge state.

The M_L peak energies entering TFD-3 were 89.6 and 88.4 MeV for the Ni and Pl_{thick} films, respectively. The particle energies exiting TFD-3 were 78.0 and 77.0 MeV for the Ni and Pl_{thick} films, respectively. Although the energies were slightly lower for the Pl_{thick} film, the luminescence peaks were virtually identical (channel number 58.6 for the Ni foil and channel number 59.0 for the Pl_{thick} film). This result, in addition to the Pl_{thin} film run, indicates a charge state effect for the M_L peak also. However, it seems like the effect is smaller for this higher

energy peak. The energy and luminescence results for the various films are summarized below:

	Pl(thin)	Pl(thick)	Nickel
$E_{in}(M_H)$ (MeV)	66.4	63.3	67.1
$E_{in}(M_L)$ (MeV)	91.3	88.4	89.6
$E_{out}(M_H)$ (MeV)	55.6	52.7	55.7
$E_{out}(M_L)$ (MeV)	79.8	77.0	78.0
$L(M_H)$	25.4	23.9	23.7
$L(M_L)$	61.7	59.0	58.6

These results are consistent with the theory that there is a higher charge state equilibrium in a plastic film than in a nickel foil. The smaller effect for the high energy peak is most likely due to shell effects [50]. As the fission fragment loses energy, it picks up electrons. These electrons de-excite and fill up the inner electronic shells of the atom. The inner shell electrons will have a much larger ionization potential than the outer shell electrons. This difference is much larger than the difference in the binding energies between a conductor and an insulator. The conductor/insulator effect will therefore be larger for ions that have already filled an inner shell than for those that are in the process of filling one. For the energy range in this work (approximately 0.5 - 1.0 MeV/amu), there is a closed shell of 28 electrons. For this energy range, this shell will be filled at a Z of about 50. As an example, representative elements were chosen for californium fission

fragment peaks. These are the peak elements, barium and
molybdenum. For molybdenum (Z = 42), this shell is not
filled until the ion energy is degraded below roughly 30 MeV
[45]. However, for barium (Z = 56), this shell is filled at
roughly 140 MeV. For the fission fragment energies used,
the 28 electron shell will be filled for the barium ions
immediately while it will not fill for the molybdenum ions
in the films. As a result, the conductor/insulator effect
will be larger for the barium ions. This holds over the Z
range of the light and heavy fission fragments.

Peak Energy Differential Calculations

Using the ion transport code TRIM [60], the energy loss
of ^{144}Ba and ^{106}Mo is modelled in Ni and polyvinyltoluene
(PVT, the bulk material of NE-102). This predicts the lower
energy difference between the two ^{252}Cf peaks in Ni as
compared to PVT. The dE/dx plots for ^{144}Ba and ^{106}Mo are
shown in Figures 4-10 and 4-11. In both plots, the
dE/dx(Ni) data were normalized such that at $E(^{144}Ba) = 80$
MeV, dE/dx(Ni) = dE/dx(PVT). From these plots, it is clear
that the high energy Mo peak has a higher relative dE/dx for
Ni than for PVT. For the low energy peak, below E = 80 MeV
(fragments initial energy), the normalized dE/dx is lower
for Ni than PVT. Therefore, in Ni, the high energy peak
will lose energy at a faster normalized rate than in PVT
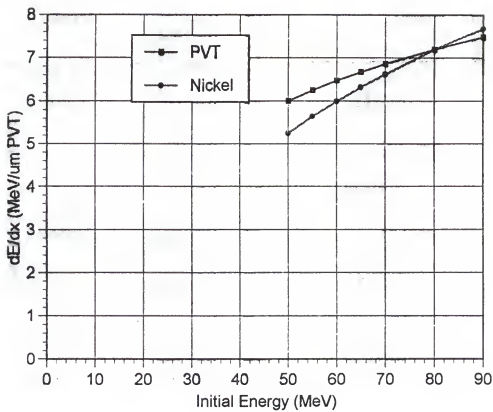
Figure 4-10: Calculated dE/dx data for ^{144}Ba in PVT and Ni.
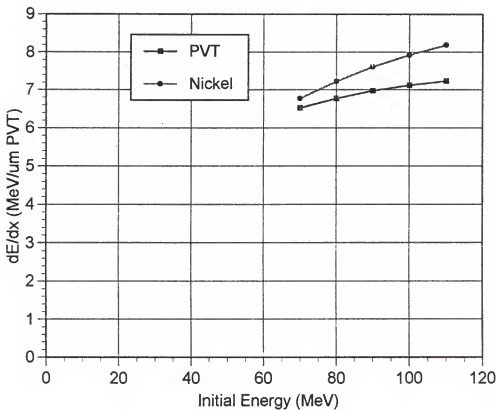
Figure 4-11: Calculated dE/dx data for ^{106}Mo in PVT and Ni.

while the low energy peak will lose energy at a lower rate. This will result in the two ^{252}Cf peaks moving closer together with the nickel foil as related to a comparable thickness of plastic film.

The ion energies as they enter the first film are roughly 80 MeV and 104 MeV for the low and high energy peaks. At this point the Mo dE/dx in PVT is slightly more than 10 % lower than in Ni, while for the low energy peak they are set equal. As the particle energies are degraded, the difference in the dE/dx for the Mo peak decreases for the two materials. However, the difference in the dE/dx increases for the Ba peak at approximately the same rate. As a result, dE/dx(Ni_{High}) - dE/dx(PVT_{High}) decreases with energy loss, while dE/dx(PVT_{Low}) - dE/dx(Ni_{Low}) increases with energy loss such that the sum is fairly constant. For the energy lost in the Ni and plastic films, the overall difference in the normalized dE/dx is between 10 % and 15 %. For an energy loss of 13 MeV, this would result in a decrease in the energy gap between the low and high energy peaks of 1.3 to 1.95 MeV for the Ni foil as compared to the plastic film. The measured difference was roughly 3.0 MeV.

Instead of using Bragg additivity rules (sum the stopping powers of all the constituent target elements), TRIM uses a system of cores and bonds. In a compound, stopping power is determined separately for inner shell electrons (cores) and for various chemical bonds (C-H, C-C, C=C, etc) [61]. The compound stopping power is thus the sum of the

stopping powers of the cores and bonds. To test the difference between this method and the standard Bragg rule, runs were made for PVT and an equivalent combination of C and H atoms. The results are shown in Figures 4-12 and 4-13.The C + H runs predict a stopping power roughly 10 % lower than for PVT. Therefore, using the traditional Bragg additivity rule can lead to a significantly different predicted energy loss.

While little data exists on the charge state equilibrium of ions passing through non-metal foils, there is a larger body of data existing on energy loss rates of particles passing through elements. Since the ion's charge state will have an effect on the energy loss rate, it is useful to investigate the energy loss rate of the ion in different media. In this way, an estimation of a difference in charge state can be made.
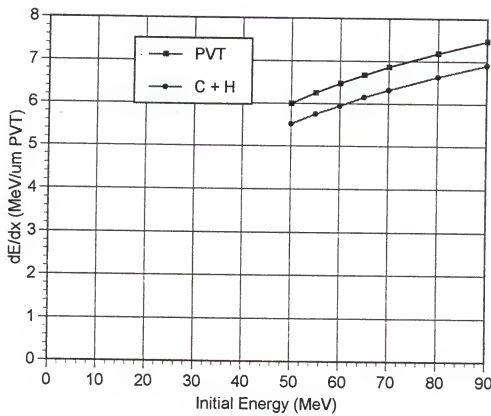
Figure 4-12: Calculated dE/dX for ^{144}Ba in PVT and C+H.
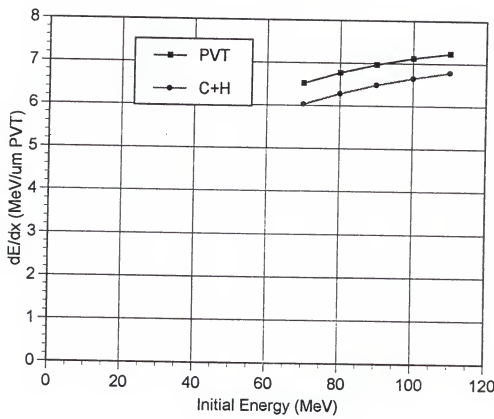
Figure 4-13: Calculated dE/dX for ^{106}Mo in PVT and C + H.

CHAPTER 5

DISCUSSION AND CONCLUSION

The results obtained by the multiple thin-film scintillator detection system will be compared with another Z-identification system. Then the results of this research will be summarized. Finally, there will be a discussion of future work.

Comparison of Results

The results obtained in this work are compared to another Z-identification system. In order for this comparison to be valid, the other system must perform particle identification over the appropriate energy and mass range (for ^{252}Cf fission fragments).

The comparable system employs a dE-E_R detector telescope in coincidence with a high-purity germanium (HPGE) detector [49]. The detector telescope consists of a 10 cm long chamber filled with P-10 gas at a pressure of 110 torr (corresponding to an energy loss of roughly 70 % for fission fragments), with the fragments stopping in an SBD. ^{252}Cf fission fragments were used for the heavy ion source. Since gamma rays tend to be emitted in the same direction as that of the particle, the HPGE detector is placed in the opposite direction of the SBD. In this way, the HPGE detector

162

detects the gammas from the complementary fission fragments.
The k X-ray peaks were used for particle discrimination. By
using the dE and E_R data, the particle Z can be approximated
using the Bethe energy loss expression. A simplified
version is shown below:

$$\frac{dE}{dx} = 3.072 * 10^{-4} \frac{Z_{eff}^2 Z_M}{\beta^2 A_M} \ln\left(\frac{m_e v^2}{I}\right)$$

Z_{eff} is the effective nuclear charge, β is v/c, Z_M and A_M
are the medium atomic number and charge respectively, m_e is
the electron rest mass, and I is mean excitation energy of
the electrons in the medium. Z_{eff} was determined
empirically for these experiments and fitted to be:

$$Z_{eff}/Z = 1 - (a_0 + a_1/E) \exp(-b_0 V_R + b_1 V_R^2)$$
$$V_R = V/(V_0 Z^{2/3})$$
$$a_0 = 1.005, \ a_1 = 1.296, \ b_0 = 0.988, \ b_1 = 0.218$$

The Z value is then calculated for the events from the k X-
ray peaks and compared with the expected Z ($Z_{exp} = 98 - Z(X-$
ray)). Using this procedure, the dE-E_R-X-ray system yielded
an overall Z resolution of 1.8 charge units as compared to
2.1 charge units for the multiple thin film system.

While the dE-E_R-X-ray system did give a better overall
charge resolution, the addition of the HPGE detector in

163

coincidence resulted in a decrease in the count rate to roughly 1/36 the SBD count rate. Also, the HPGE detector requires the use of liquid nitrogen. Therefore, with this system, the addition of the HPGE detector was instrumental in increasing the system resolution at the cost of a significant decrease in count rate and a more complex system relative to the multiple thin-film scintillator detection system.

Summary and Conclusion

The multiple thin-film scintillator detection system was designed, built and tested with ^{252}Cf fission fragments. A method for the calculation of the fragment's nuclear charge (Z) was determined, yielding a charge resolution of 2.1 charge units. The utility of the system was then tested for the measurement of charge state effects of fission fragments passing through nickel foils and plastic films.

In the development of the system, two types of scintillator films were tested to determine their applicability. NE-102 (which contains only 2 - 3 % primary scintillator, para-terphenyl) and pure p-terphenyl. After testing the scintillation outputs of various thicknesses of both films, it was determined that NE-102 gave a scintillation output roughly twice that of p-terphenyl. This was due mainly to the self-absorption of the p-

terphenyl and the high efficiency of energy transfer from the bulk material of NE-102 to the primary scintillator.

The multiple thin-film scintillator detection system was then assembled and calibrated with ^{252}Cf fission fragments. Initially, three films were used in series, but it was determined that using two films would yield a better overall resolution. The distance between films 1-2 and 2-3 was not far enough to give a good TOF resolution. However, removing the second film would give a loss in luminescence resolution. The decrease in luminescence resolution was minor compared to the increase in TOF resolution. The TOF, luminescence, and energy reading were then calibrated to yield their data in appropriate units. A method was then determined that would combine these measurements into an algorithm for the Z calculation of individual fission fragments. The Z resolution was determined to be 2.1 charge units. This differs from previous research in that the nuclear charge is determined as opposed to the mass.

The multiple thin film system was then used to determine whether there is a difference in the ionic charge state of fission fragments after passing through a nickel film or plastic foil. Since luminescence is dependent on the transiting particles ionic charge state, for particles of equivalent energy and Z, a difference in luminescence would be the result of a different ionic charge. This was measured by matching the particle energies entering and exiting the foils. By observing the luminescence output, it

was learned that the ionic charge state of fission fragments is lower after passing through a nickel foil than a plastic film with equivalent energy loss. It was concluded that the reason for this was that the fragments gain electrons more readily from the conductor medium of the nickel foil than from the insulator medium of the plastic film due to the lower ionization potential in a metal.

This system has many functions as a general purpose charged particle detection system. It is inexpensive and portable, with fairly simple electronic equipment. The variety of parameters employed (TOF, energy, and luminescence) permits a flexibility that enables the measurement of other variables. An example of this is the measurement of charge state equilibrium.

Future Work

The tests demonstrating that the charge state equilibrium of particles transiting the medium is dependent on the type of medium opens up an entirely new area of research. It has been previously demonstrated that there is a difference in charge state equilibrium between particles traversing a solid or a gas. This was attributed to the lower interaction rate of ions traveling through a gas. However, the difference in charge state between the nickel foil and plastic film was attributed to the lower ionization potential in the nickel.

To prove this hypothesis, a series of tests should be run using a variety of different media (conductor, semiconductor, insulator) of varying ionization potentials. In order to perform these tests, an accelerator would be required for the source of various monoenergetic particles of a certain charge state. The scintillator films would need to be calibrated for ions of different Z, energy, and charge state. Once the scintillator response has been calibrated, the accelerated ions would then be passed through a medium before striking the scintillator. The calibrated scintillation output would then yield the ion's charge state.

Scintillator films are a very good choice to perform this research for several reasons. First, the scintillation output is dependent on the particles charge state. Also, they are easily constructed and don't require much ancillary equipment. Finally, their thin size and lack of detector window yields a luminescence signal before the particles re-equilibrate to a different charge state.

This section will provide a brief description and a printout of each code. The three codes are MODE 50 (MD50), 11GROUP, and ANALYSIS.

The codes can be executed in one of two ways. By going into the Quick Basic program and linking with libraries, programs can be edited and run without compiling. This is done by going to the AD16 directory and entering the command QB/L CIO16. This runs quick basic and links it with the CIO16 libraries. Once inside, basic programs can be opened, edited, and run. The other way to run a basic program is to create an executable file. This is also done within the quick basic program. After the executable file is created, it can be run from DOS by simply typing in the name of the file.

Appendix A1: MODE 50 Data Acquisition Code

The data acquisition board came with canned programs to perform various functions. The Mode 50 program (MD50) is a general data acquisition code. The D%(X) variables enable the user to set the program defaults to their needs. D%(0) and D(1) specify the lower and upper channel numbers (Channel 0 - 15). D%(4) sets the number of data points to

acquire (16 for this case, or 1 pass through all the channels). D%(7) and D%(8) set the method of triggering (internal/external) and the voltage level of the trigger.

The data acquisition subroutine is called L times. Therefore, this is the number of fission events that are recorded. After the external trigger is received, a check is made to see if the event was a fission fragment or an alpha particle. A lower level discriminator is set for the SBD signal so that any signals below that level will not be saved. If this criterion is met, then the channel data are saved into the file "DATAFILE". Two channels of the sample-and-hold board were not giving reliable data (channels 2 and 3). In order to conserve space on the hard drive, these channels were not saved. After being saved, the channel data are printed to the screen along with the event number. This aids in setting the trigger levels for the electronics along with giving a record of the progress of the data acquisition.

```
'********************** MODE 50 DATA ACQUISITION
***************

DIM D%(16)
DIM DAT%(1000), CHAN%(1000)  'INTEGER ARRAYS FOR A/D DATA
DIM CHDAT%(100), BIN1(5000), BIN15(5000), DIFF(1000)
COMMON SHARED D%(), CHAN%(), DAT%()
DECLARE SUB CIO16 (MD%, BYVAL DUMMY%, F%)

F$ = "DATAFILE"               'OUTPUT FILENAME
OPEN F$ FOR OUTPUT AS #1

'$DYNAMIC
DIM RAWDAT%(1000)
'$STATIC

'********************** INITIALIZE ********************

        D%(0) = &H300          'CIO16 BASE I/O ADDRESS
        D%(1) = 3              'INTERRUPT LEVEL
        D%(2) = 1              'DMA LEVEL
        MD% = 0
        F% = 0
        CALL CIO16(MD%, VARPTR(D%(0)), F%)
        IF F% <> 0 THEN PRINT "MODE 0 ERROR # "; F%: STOP

'********************** CALL MODE 50 ******************
        FOR L = 1 TO 100000    'L = NUMBER OF EVENTS

        D%(0) = 0              'LOWER CHAN SCAN LIMIT
        D%(1) = 15             'UPPER CHAN SCAN LIMIT (0-15 CH)
        D%(2) = 1              'OVERALL SAMPLING RATE IS 1,105 HZ.
        D%(3) = 105            '1 KHZ + 105 HZ. ASSUMES 1 MHZ CLK
        D%(4) = 16             'COLLECT 16 POINTS
        D%(5) = VARPTR(DAT%(0))   'DATA POINT ARRAY
        D%(6) = VARPTR(CHAN%(0))  'CHANNEL TAG ARRAY
        D%(7) = 1              'TRIGGER externally
        D%(8) = 1              'SET RANGE TO +/- 5 VOLTS
        MD% = 50               'EASY TO USE A/D MODE
        CALL CIO16(MD%, VARPTR(D%(0)), F%)
        IF F% <> 0 THEN PRINT "MODE 50 ERROR # "; F%: STOP

'*************** PRINT DATA TO SCREEN AND SAVE *********
'*** PERFORMS A CHECK TO SEE IF SBD SIGNAL (DAT%(4)) IS
'*** ABOVE A THRESHHOLD AND THAT EVENT WAS TRIGGERED BY
'*** FISSION FRAGMENT

        IF DAT%(4) < 200 THEN J = J - 1
        IF DAT%(4) < 200 THEN GOTO 100

'****** SAVES DATA TO DATAFILE

        FOR I = 1 TO 15        'SKIPS CHANNELS 2 AND 3,
```

```
      IF I = 2 OR I = 3 THEN GOTO 99 'WHICH ARE EMPTY
      PRINT #1, DAT%(I);     'STORES DATA IN "DATAFILE"
99    NEXT I
      PRINT #1,

'****** PRINTS DATA TO SCREEN

      PRINT DAT%(1); DAT%(4); DAT%(5); DAT%(6);
      PRINT DAT%(7); DAT%(8); DAT%(9);
      PRINT DAT%(12); DAT%(13); DAT%(14); DAT%(15), L
100   NEXT L

      CLOSE #1
      END

'***********************************************************
```

A2: 11GROUP Program

This program separates a ^{252}Cf fission fragment
spectrum into 11 groups according to the luminescence
signals. The spectrum is broken up according to the
percentages specified below:

Group	Range (%)
1	0 - 7
2	7 - 18
3	18 - 31
4	31 - 40
5	40 - 46
6	46 - 54
7	54 - 60
8	60 - 69
9	69 - 82
10	82 - 93
11	93 - 100

This is shown graphically, in Figure A1. As can be seen in
the figure, the groups were chosen such that both peaks and
the valley are in their own group. The upper and lower tail
of the spectrum along with the regions between the peaks and
valley are broken up into two regions apiece. If the cutoff
between groups occurs in the middle of a channel, the first
X data points needed to complete the lower group are taken.
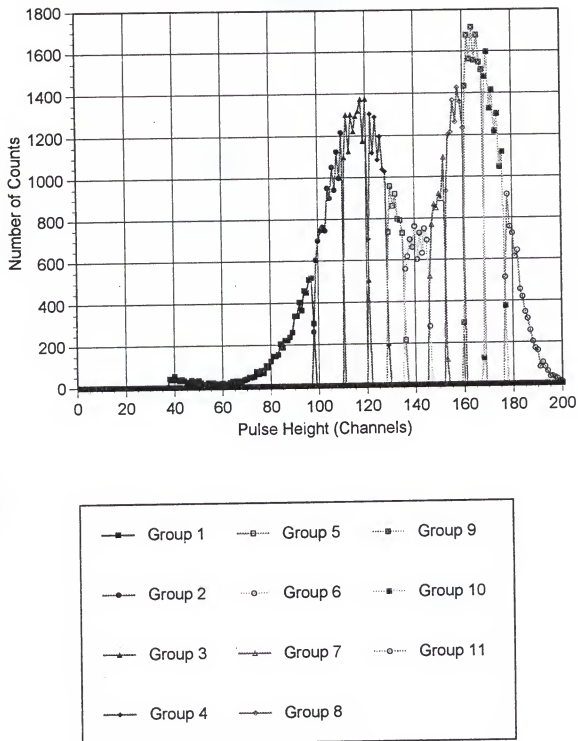
Figure A1: 11 group ^{252}Cf spectrum for SBD.

The rest are placed in the next group. By looking at the 11 group spectrum, any irregularities (usually lower level discriminator set too high) can be seen and corrected or the data is thrown out.

After the energy group cutoff channels have been determined, the data is re-evaluated and each event is assigned a group. Therefore, all data (time-of-flight, residual energy, etc) will have a group assigned to it.

Before the luminescence signals can be separated into groups, they must first be normalized. After they are normalized, a geometric correction value is included for each film. Finally the signals from each film are added to get a summed luminescence.

After all corrections have been made, the film signals are added. The sums are then separated into 11 groups and the group cutoff channels are saved.

Then the data is read again and each event is assigned a group according the previously calculated ranges. At this point the data can be put into 200 channel groups or 200x11 arrays.

```
' THIS PROGRAM SEPARATES A CALIFORNIUM-252 SPECTRUM
' INTO 11 GROUPS ACCORDING TO THE RESIDUAL ENERGY

        OPEN "I", 1, "DATAFILE"   'INPUT FILE WITH RAW DATA
        OPEN "O", 5, "GROUPS"     'OUTPUT FILE WITH GRP RANGES

' DIMENSIONS APPROPRIATE DATA ARRAYS

        DIM DAT(200, 15), CH(16), SBD(200, 15), SUM(4100)
        DIM BIN(4100), SUM3(200), CHN15(201), CHN16(201)
        DIM BIN15(200), BIN16(200), TFD(200), CHN5(201)
        DIM BIN5(200), GRP(12), CHN2(200), CHN7(200)
        DIM CHN8(200), CHN10(200), SUM1(200), SUM2(200)
        DIM BIN2(200), BIN7(200), BIN8(200), BIN10(200)

'****** IMPORTS THE DATA FROM "DATAFILE"

5       FOR I = 1 TO 100       'I*II = NUMBER OF EVENTS
        FOR II = 1 TO 1000
        FOR III = 2 TO 16
        IF III = 3 OR III = 4 THEN GOTO 6   'SKIP CHANNEL 3
                       ' AND 4 BECAUSE THEY ARE EMPTY
        INPUT #1, CH(III)
6       NEXT III

'****** REDUCES DATA TO 200 CHANNELS FROM 4095 AND
'****** NORMALIZES FILM OUTPUTS

        CH2 = CH(2) / 13.64            ' FILM 2
        CH7 = CH(7) / 22.8             ' FILM 2
        CH8 = CH(8) / 24.1             ' FILM 1
        CH10 = CH(10) / 7.16           ' FILM 1
        CH15 = CH(15) / 16.9           ' FILM 3B
        CH16 = (CH(16) + 17) / 9.82    ' FILM 3A

'****** DETERMINES RATIOS AND CALCULATES A GEOMETRIC
'****** CORRECTION VALUE (VL) FOR EACH FILM

        R1 = CH8 / (CH10 + .01)
        IF R1 > 1 THEN R1 = 1 / R1
        R2 = CH2 / (CH7 + .01)
        IF R2 > 1 THEN R2 = 1 / R2
        R3 = CH15 / (CH16 + .1)
        IF R3 > 1 THEN R3 = 1 / R3
        VL1 = .22302 + 3.6672 * R1 - 8.2209 * R1 ^ 2 +
10.608 * R1 ^ 3 - 7.3836 * R1 ^ 4 + 2.107 * R1 ^ 5
        VL2 = .22302 + 3.6672 * R2 - 8.2209 * R2 ^ 2 +
10.608 * R2 ^ 3 - 7.3836 * R2 ^ 4 + 2.107 * R2 ^ 5
        VL3 = .22302 + 3.6672 * R3 - 8.2209 * R3 ^ 2 +
10.608 * R3 ^ 3 - 7.3836 * R3 ^ 4 + 2.107 * R3 ^ 5
```

```
'****** SUMS THE 6 PMT OUTPUT CHANNELS TO 4095 CHANNELS

        SUMALL = INT(((CH2 + CH7) * VL2 + (CH8 + CH10) * VL1
+ (CH15 + CH16) * VL3) * 41 / 6)
        IF SUMALL > 4095 THEN SUMALL = 4095
        BIN(SUMALL) = BIN(SUMALL) + 1
        NEXT II
        PRINT I, "1"
        NEXT I

'****** DETERMINES GROUP CUTOFFS BY INTEGRATING THE CHANNELS
'****** AND COMPARING THE SUM TO PRESET GROUP SIZES

        FOR J = 1 TO 4095
        SUM(0) = 0
        SUM(J) = SUM(J - 1) + BIN(J)
        GRP(0) = 0
        IF SUM(J - 1) <= 7000 AND SUM(J) > 7000
THEN GRP(1) = J
        IF SUM(J - 1) <= 18000 AND SUM(J) > 18000
THEN GRP(2) = J
        IF SUM(J - 1) <= 31000 AND SUM(J) > 31000
THEN GRP(3) = J
        IF SUM(J - 1) <= 40000 AND SUM(J) > 40000
THEN GRP(4) = J
        IF SUM(J - 1) <= 46000 AND SUM(J) > 46000
THEN GRP(5) = J
        IF SUM(J - 1) <= 54000 AND SUM(J) > 53000
THEN GRP(6) = J
        IF SUM(J - 1) <= 60000 AND SUM(J) > 59000
THEN GRP(7) = J
        IF SUM(J - 1) <= 69000 AND SUM(J) > 69000
THEN GRP(8) = J
        IF SUM(J - 1) <= 82000 AND SUM(J) > 82000
THEN GRP(9) = J
        IF SUM(J - 1) <= 93000 AND SUM(J) > 93000
THEN GRP(10) =J
        GRP(11) = 4095
        NEXT J

'****** SAVES GROUP CHANNEL RANGES

        FOR KK = 1 TO 11
        PRINT #5, GRP(KK);
        NEXT KK
        CLOSE #1
        CLOSE #5

'****** OPENS "DATAFILE" AND READS DATA

        OPEN "I", 4, "DATAFILE"
10      FOR L = 1 TO 100
        FOR LL = 1 TO 1000
```

```
        FOR J = 2 TO 16            'SKIPS CH 1 (EMPTY)
        IF J = 3 OR J = 4 GOTO 11  'SKIPS CH 3 AND 4
        INPUT #4, CH(J)
11      NEXT J

'****** REDUCES 4095 CHANNEL DATA TO 100 CHANNELS

        CH5 = INT((CH(5)) / 11.67)    ' SBD
        CH2 = CH(2) / 13.64           ' FILM 2
        CH7 = CH(7) / 22.8            ' FILM 2
        CH8 = CH(8) / 24.1            ' FILM 1
        CH10 = CH(10) / 7.16          ' FILM 1
        CH15 = (CH(15)) / 16.93       ' FILM 3B
        CH16 = (CH(16) + 17) / 9.82   ' FILM 3A
        CH6 = CH(6) / 41          'TOF 1B-3B
        CH9 = CH(9) / 41          'TOF 1-2
        CH13 = CH(13) / 41        'TOF 1A-3A
        CH14 = CH(14) / 41        'TOF 2-3

'** CALCULATES THE GEOMETRIC CORRECTION VALUE FOR EACH FILM

        R1 = CH8 / (CH10 + .01)
        IF R1 > 1 THEN R1 = 1 / R1
        R2 = CH2 / (CH7 + .01)
        IF R2 > 1 THEN R2 = 1 / R2
        R3 = CH15 / (CH16 + .01)
        IF R3 > 1 THEN R3 = 1 / R3
        VL1 = .22302 + 3.6672 * R1 - 8.2209 * R1 ^ 2 +
10.608 * R1 ^ 3 - 7.3836 * R1 ^ 4 + 2.107 * R1 ^ 5
        VL2 = .22302 + 3.6672 * R2 - 8.2209 * R2 ^ 2 +
10.608 * R2 ^ 3 - 7.3836 * R2 ^ 4 + 2.107 * R2 ^ 5
        VL3 = .22302 + 3.6672 * R3 - 8.2209 * R3 ^ 2 +
10.608 * R3 ^ 3 - 7.3836 * R3 ^ 4 + 2.107 * R3 ^ 5

'****** PERFORM CHECKS TO SEE IF DATA IS OUT OF RANGE

        IF CH15 > 200 THEN GOTO 20
        IF CH16 > 200 THEN GOTO 20
        IF CH5 > 200 THEN GOTO 20

'****** SUMS THE 3 FILM DATA INTO 4095 AND 200 CHANNELS

        SUM123 = INT(((CH2 + CH7) * VL2 + (CH8 + CH10) * VL1
+ (CH15 + CH16) * VL3) * 41 / 6)
        RAW = ((CH2 + CH7) * VL2 + (CH8 + CH10) * VL1 +
(CH15 + CH16) * VL3) / 3
        RAW123 = INT(RAW)
        IF SUM123 > 4095 THEN SUM123 = 4095
        IF RAW123 > 200 THEN RAW123 = 200
```

```
'****** CALCULATES THE MASS BASED ON EMPIRICALLY DERIVED
'****** FORMULA

        M = 168.6 - 1.082 * RAW + .00305 * RAW * RAW
        IF M > 200 THEN M = 200
        MASS = INT(M)

'****** PUTS DATA INTO 200 GROUP BINS

        BIN5(CH5) = BIN5(CH5) + 1
        BIN15(CH15) = BIN15(CH15) + 1
        BIN16(CH16) = BIN16(CH16) + 1
        TFD(RAW123) = TFD(RAW123) + 1
        TOT3 = INT(.5 * (CH15 + CH16) * VL3)
        RAW3 = INT(.5 * (CH15 + CH16))

'****** DETERMINES GROUP NUMBER (1 - 11) FOR EACH DATA POINT

        FOR LLL = 1 TO 11
        IF SUM123 <= GRP(LLL) AND SUM123 > GRP(LLL - 1) THEN
GP = LLL
        NEXT LLL

'****** PUTS DATA INTO 2 DIMENSIONAL ARRAY

        DAT(RAW123, GP) = DAT(RAW123, GP) + 1
        SBD(CH5, GP) = SBD(CH5, GP) + 1
20      NEXT LL

'****** SAVES DATA INTO FILE "11GRP.INP"

        PRINT L, "2"
        NEXT L
        CLOSE #4
        OPEN "O", 2, "11GRP.INP"
        FOR J = 1 TO 200
        PRINT #2, J; BIN5(J); BIN15(J); BIN16(J); TFD(J);
'1-D DATA
        FOR I = 1 TO 11
        PRINT #2, DAT(J, I);          '2-DIMENSIONAL DATA
        NEXT I
        FOR II = 1 TO 11
        PRINT #2, SBD(J, II);
        NEXT II
        PRINT #2,
        NEXT J
        CLOSE #2
        END
```

A3: ANALYSIS Program

This program reads the raw data from the file "DATAFILE" and calculates the nuclear charge and other parameters. With slight modifications, this analysis program will output the various data channels for a constant nuclear charge, residual energy, or other parameter.

After reading the raw data, each channel is normalized according to previously determined factors (see chapter on data calibration). Then the geometric factors were calculated and included in the summed luminescence signals. From the summed luminescence, an estimated fragment mass and nuclear charge (Z) were determined from empirical formulas. using the estimated mass, the residual energy is calculated using Schmitt's formula.

Using Z as a starting estimate of the nuclear charge, two modifications are made to take the residual energy and time-of-flight (TOF) into account. First, the E_r and TOF are plotted vs. Z. Then a function is fit to this data to correlate these variables (determine $E_r(Z)$ and $TOF(Z)$). These functions result in an estimate of an energy and time from Z. A ΔZ is calculated by taking a difference between the estimated and measured values and dividing by the standard deviation. The ΔZ is then appropriately added or subtracted to Z and a new nuclear charge is determined. This is done first with the residual energy and then with the time-of-flight to determine the final nuclear charge Z".

After Z" is calculated, individual parameters are discretized. In this way, "slices" of data (for example Z"=42) can be analyzed by simply passing over this section if the criterion (Z <> 42) is not met. This is the method used to investigate the uncertainty of Z and Z".

For the 2-dimensional data arrays, the 200 channel data was collapsed to 100 channels. Typically, only 70 channels were saved. This reduced the data arrays to a size that could be handled by the graphing program without a significant loss of resolution.

After all parameters have been discretized, they are saved in various output files. "ENERGY" saves all 1-dimensional parameters. "ZDATA" saves only those parameters used in the Z, Z', and Z" calculations. "TWODIM" saves the three 2-dimensional data arrays. Any combination of variables can be included in the arrays.

The "ANALYSIS" code is given in the following pages.

```
'****** ANALYSIS PROGRAM FOR THE CALCULATION OF NUCLEAR
'****** CHARGE AND OTHER PARAMETERS

'****** OPENS DATA FILE AND DIMENSIONS APPROPRIATE ARRAYS

        OPEN "I", 1, "DATAFILE"      'OPENS FILE WITH RAW DATA
        DIM DAT(200), CH(16), SBD(200), SUM(4100), BIN(4100)
        DIM SUM3(200), CHN15(201), CHN16(201), BIN15(200)
        DIM BIN16(200), TFD(200), CHN5(201), BIN5(200)
        DIM GRP(12), SUM1(200), SUM2(200), MAS(200)
        DIM CHN2(200), CHN7(200), CHN8(200), CHN10(200)
        DIM BIN2(200), BIN7(200), BIN8(200), BIN10(200)
        DIM VEL1(200), VEL2(200), ENG1(200), ENG2(200)
        DIM TWOD1(70, 70), TWOD2(70, 70), TWOD3(70, 70)
        DIM T13A(200), T13B(200), T13SUM(200)
        DIM FILM1(200), FILM3(200), ENGR(200), FILM1A(200)
        DIM FILM1B(200), FILM3A(200), FILM3B(200)
        DIM ZINIT(200), ZPRIME1(200), ZPRIME2(200)
        DIM ZENGR(200), ZT13SUM(200)

'****** IMPORTS DATA FROM L*LL EVENTS

10      FOR L = 1 TO 100
        FOR LL = 1 TO 1000          ' IMPORTS CHANNEL DATA
        FOR J = 2 TO 16             ' FROM EACH EVENT
        IF J = 3 OR J = 4 GOTO 11   ' CHANNELS 3 AND 4 ARE
        INPUT #1, CH(J)             ' EMPTY
11      NEXT J

'****** NORMALIZES 4095 CHANNEL DATA TO FIT 200 CHANNELS

        CH2 = CH(2) *1.2 / 13.64          'FILM 2B
        CH5 = INT(CH(5) / 11)             'SBD
        CH7 = CH(7) * 1.8 / 22.8          'FILM 2A
        CH8 = CH(8) / 24.1                'FILM 1B
        CH10 = CH(10) / 7.16              'FILM 1A
        CH15 = (CH(15)) / 16.9            'FILM 3B
        CH16 = (CH(16) + 17) / 9.82       'FILM 3A
        CH6 = ABS((CH(6) / 41) * .619 + .3)      'TOF 1B-3B (NS)
'       CH9 = CH(9) / 10.25                      'TOF 1-2
        CH13 = (.619 * CH(13) / 41 + 5.6)        'TOF 1A-3A (NS)
'       CH14 = (((CH(14) / 20.5) - 50) * 2)      'TOF 2-3

'****** DETERMINES THE RATIO OF THE TWO SIGNALS FROM EACH
'****** FILM AND APPLIES A CORRECTION VALUE TO ACCOUNT
'****** FOR GEOMETRIC EFFECTS

        R1 = (CH7) / (CH2 + .01)     'RATIO FOR 1ST FILM
        IF R1 > 1 THEN R1 = 1 / R1   '0.01 ADDED IN CASE
        R2 = CH8 / (CH10 + .01)      'DENOMINATOR IS 0
        IF R2 > 1 THEN R2 = 1 / R2   '2ND FILM
        R3 = CH15 / (CH16 + .1)      '3RD FILM
        IF R3 > 1 THEN R3 = 1 / R3
```

```
        VL1 = .22302 + 3.6672 * R1 - 8.2209 * R1 ^ 2 +
10.608 * R1 ^ 3 - 7.3836 * R1 ^ 4 + 2.107 * R1 ^ 5
        VL2 = .22302 + 3.6672 * R2 - 8.2209 * R2 ^ 2 +
10.608 * R2 ^ 3 - 7.3836 * R2 ^ 4 + 2.107 * R2 ^ 5
        VL3 = .22302 + 3.6672 * R3 - 8.2209 * R3 ^ 2 +
10.608 * R3 ^ 3 - 7.3836 * R3 ^ 4 + 2.107 * R3 ^ 5

'****** SUMS ALL 3 FILMS, INCLUDING THE GEOMETRIC FACTORS
'****** VL1, VL2, VL3: RAW=200 GROUPS, SUM123=4095 GROUPS

        SUM123 = INT(((CH2 + CH7 - 2) * VL2 +  (CH15 + CH16)
* VL3) * 41 / 4)
        RAW = ((CH2 + CH7 - 2) * VL2  +  (CH15 + CH16) *
VL3) / 2
        RAW123 = INT(RAW)
        IF SUM123 > 4095 THEN SUM123 = 4095
        IF RAW123 > 200 THEN RAW123 = 200
        IF RAW > 200 THEN RAW = 200

'****** ESTIMATES MASS AND Z FROM TFD SIGNALS ACCORDING TO
'****** EMPIRICALLY DERIVED FORMULA

        Z = 69.31 - .3666 * RAW + .0008512 * RAW * RAW
        M = 176.4 - .8963 * RAW + .001971 * RAW * RAW

        ZZ = INT(Z)

'****** CALCULATES RESIDUAL ENERGY ACCORDING TO
'****** SCHMITT'S FORMULA

        ER1 = ((.5036 + .000749301# * M) * CH5 + 4.45 +
.01029 * M)

        ER = INT(ER1)

'****** ESTIMATES RESIDUAL ENERGY FROM Z DATA BASED ON
'****** EMPIRICAL FORMULA

        ERZ = 286.36 - 9.739 * Z + .1633 * Z * Z - .001118 *
Z * Z * Z

'****** CALCULATES ΔZ1 BASED ON DIFFERENCE BETWEEN ESTIMATED
'****** RESIDUAL ENERGY AND MEASURED ENERGY DIVIDED BY THE
'****** STANDARD DEVIATION

        DELTAZ1 = ((ERZ - ER1) / 5)
        Z2 = Z + DELTAZ1
        ZZP1 = INT(Z2)
        ERZZ = INT(ERZ)

'****** CALCULATES ΔZ2 BASED ON DIFFERENCE BETWEEN ESTIMATED
'****** TOF AND MEASURED TOF DIVIDED BY THE STANDARD
'****** DEVIATION, DETERMINES FINAL Z"
```

```
        TME = (2 * (CH6 + CH13))          '4 * TIME
        TSM = INT(TME)                    'AVERAGED TIME

'****** CHECK TO SEE IF BOTH TOF MEASUREMENTS ARE WITHIN
'****** EXPERIMENTAL ERROR

        IF CH6 / (CH13 + .01) > 1.2 OR CH6 / (CH13 + .01) <
.8 THEN GOTO 20
        IF TSM > 200 THEN TSM = 200

'****** TIME ESTIMATE BASED ON Z' DATA

        TIMEZ = ABS(-20.1 + 5.531 * Z2 - .1225 * Z2 * Z2 +
.001246 * Z2 * Z2 * Z2)
        DELTAZ2 = 20 * ((TME - TIMEZ) / TME)
        ZZP2 = INT(Z2 + DELTAZ2)          'Z'
        TIMEZZ = INT(TIMEZ)

'****** THE NEXT SECTION DISCRETIZES THE VARIOUS PARAMETERS
'
'****** BY ADDING LINES SIMILAR TO THE NEXT 2 LINES, AN
'****** ANALYSIS CAN BE MADE OF Z" = 42 AND 79 < ER < 81
'        IF ZZP2 <42 OR ZZP2 > 42 GOTO 20
'         IF ER > 81 OR ER < 79 GOTO 20
        FLM1A=INT(CH10)
        FLM1B=INT(CH8)
        FLM3A=INT(CH16)
        FLM3B=INT(CH15)
        FILM1A(FLM1A)=FILM1A(FLM1A) + 1
        FILM1B(FLM1B)=FILM1B(FLM1B) + 1
        FILM3A(FLM3A)=FILM3A(FLM3A) + 1
        FILM3B(FLM3B)=FILM3B(FLM3B) + 1
        TM13 = INT(CH13)
        TM6 = INT(CH6)
        T13A(TM13) = T13A(TM13) + 1
        T13B(TM6) = T13B(TM6) + 1
        T13SUM(TSM) = T13SUM(TSM) + 1
        IF TIMEZ > 200 THEN TIMEZ = 200

        IF CH15 > 200 THEN CH15=200
        IF CH16 > 200 THEN CH16=200
        IF CH5 > 200 THEN CH5=200

        IF CH8 > 200 THEN CH8 = 200
        IF CH10 > 200 THEN CH10 = 200

        FLM1 = ABS(INT((CH7 + CH2 - 2) * VL1))
        FLM3 = INT((CH15 + CH16) * VL3)
        IF FLM1 > 200 THEN FLM1 = 200
        IF FLM3 > 200 THEN FLM3 = 200
        FILM1(FLM1) = FILM1(FLM1) + 1
        FILM3(FLM3) = FILM3(FLM3) + 1
```

```
'****** AVERAGES BOTH TOF 1-3 SIGNALS

        TBAR1 = .5 * (CH13 + CH6)


'****** VELOCITY IS DETERMINED BELOW WITH D(1-3) = 30.2 CM

        V13 = 30.2 / (TBAR1)
        V13B = INT(50 * V13)
        IF V13B > 200 THEN V13 = 200

'****** ENERGY EQUATIONS: UNITS ARE E(MeV), M(amu), V(cm/ns)
'****** 1.036 IS THE CONVERSION FACTOR FOR THESE UNITS

        E13 = INT(.5 * 1.036 * M * V13 * V13)
        IF E13 > 200 THEN E13 = 200

        ERB = INT(ER / 2)            'CONVERTS 200 BIN DATA SET
        E13B = INT(E13 / 2)          'TO 100 BINS FOR 2-D ARRAYS
        CH5B = INT(CH5 / 2)          '(200 x 200 IS TOO LARGE FOR
        RAWB = INT(RAW / 2)          'GRAPHING PROGRAM TO HANDLE)
        TIME = INT(TBAR1)
        VEL1(V13B) = VEL1(V13B) + 1
        MASS = INT(M)
        ZB = ABS(ZZP2 - 20)               'ADJUSTS DATA TO FIT INTO
        MB = INT(M / 2) - 20              '70 GROUPS
        LUM = INT(RAW123 / 3)
        TWOD1(TIME, ZB) = TWOD1(TIME, ZB) + 1      '2-D DATA
        TWOD2(ERB, ZB) = TWOD2(ERB, ZB) + 1        'ARRAYS
        TWOD3(LUM, ZB) = TWOD3(LUM, ZB) + 1
        ENG1(E13) = ENG1(E13) + 1            '200 GROUP BINS
        ENGR(ER) = ENGR(ER) + 1
        IF MASS > 200 THEN MASS = 200
        MAS(MASS) = MAS(MASS) + 1
        BIN5(CH5) = BIN5(CH5) + 1
        TFD(RAW123) = TFD(RAW123) + 1

        ZINIT(ZZ) = ZINIT(ZZ) + 1
        ZPRIME1(ZZP1) = ZPRIME1(ZZP1) + 1
        ZPRIME2(ZZP2) = ZPRIME2(ZZP2) + 1
        ZENGR(ERZZ) = ZENGR(ERZZ) + 1
        ZT13SUM(TIMEZZ) = ZT13SUM(TIMEZZ) + 1
20      NEXT LL
        PRINT L,      'COUNTER TO SHOW PROGRESS OF PROGRAM
        NEXT L

'****** OPENS OUTPUT FILE 1 DIMENSIONAL DATA AND STORES DATA

        OPEN "O", 2, "ENERGY"
        FOR J = 1 TO 200
        PRINT #2, J; BIN5(J); TFD(J); ZINIT(J) ;ZPRIME1(J);
        PRINT #2, ZPRIME2(J); ENG1(J); ENGR(J); MAS(J);
        PRINT #2, VEL1(J); T13A(J); T13B(J); T13SUM(J);
```

```
        PRINT #2, FILM1(J); FILM3(J); FILM1A(J); FILM1B(J);
        PRINT #2, FILM3A(J); FILM3B(J)
        NEXT J
        CLOSE #2

        OPEN "O", 4, "ZDATA"
        FOR L = 1 TO 200
        PRINT #4, L; ZINIT(L); ZPRIME1(L); ZPRIME2(L);
        PRINT #4, ENGR(L); ZENGR(L); T13SUM(L);
        PRINT #4, ZT13SUM(L); TFD(L)
        NEXT L
        CLOSE #4

'****** OPENS DATA FILE FOR 2 DIMENSIONAL DATA ARRAYS AND
'****** STORES DATA

        OPEN "O", 3, "TWODIM"

        FOR K = 1 TO 70
        FOR KK = 1 TO 70
        PRINT #3, K; KK; TWOD3(K, KK), TWOD2(K, KK),
        PRINT #3, TWOD3(K, KK)
        NEXT KK
        NEXT K
        CLOSE #3
        END
```

APPENDIX B

DESCRIPTION AND DERIVATION OF SCHMITT'S METHOD FOR SURFACE BARRIER DETECTORS CALIBRATION FOR ^{252}Cf FISSION FRAGMENTS

Schmitt's method [36] of ^{252}Cf fission fragment energy calibration is a direct correlation between fragment pulse height and fragment energy. Extensive studies of various surface barrier detectors with accelerated ions and fission fragments suggested that a general equation of the following form would apply:

A1) $E(M,Ch) = (a + a'M)Ch + b + b'M$

E = Ion Energy

M = Ion Mass

Ch = Channel number for energy signal

In order to solve for the four unknowns (a, a', b, and b'), four equations would be required. Therefore, four signals from ions of known energies and masses are needed. Schmitt chose ^{80}Br and ^{127}I with pulse heights corresponding to the light and heavy fission fragments from a ^{252}Cf spectrum. This is shown in Figure B1 below:
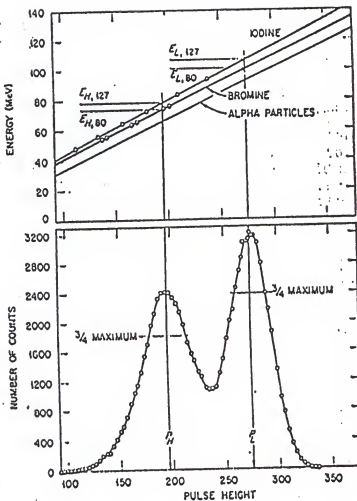
Figure B1: Energy vs pulse height for Br and I ions (top). ^{252}Cf fission spectrum (bottom) [36].

Schmitt measured the Br and I energies for both peaks with several SBD detectors. He then averaged the results and produced the following energies (+/- 0.15 MeV):

$E_{L127} = 107.01$ MeV

$E_{L80} = 100.57$ MeV

$E_{H127} = 78.45$ MeV

$E_{H80} = 73.69$ MeV

where:

E_{L127} = Energy of ^{127}I at the peak channel of the ^{252}Cf light fission fragment (P_L)

E_{L80} = Energy of ^{80}Br at the peak channel of the ^{252}Cf light fission fragment (P_L)

E_{H127} = Energy of ^{127}I at the peak channel of the ^{252}Cf heavy fission fragment (P_H)

E_{H80} = Energy of ^{80}Br at the peak channel of the ^{252}Cf heavy fission fragment (P_H)

2A) $E_{L127} = 107.01 = (a + 127a')P_L + b + 127b'$

3A) $E_{L80} = 100.57 = (a + 80a')P_L + b + 80b'$

4A) $E_{H127} = 78.45 = (a + 127a')P_H + b + 127b'$

5A) $E_{H80} = 73.69 = (a + 80a')P_H + b + 80b'$

Subtracting (3A) from (2A):

6A) $6.44 = 47a'P_L + 47b'$

  $b' = (6.44 - 47a'P_L)/47$

  $b' = 0.1370 - a'P_L$

Subtracting (5A) from (4A):

7A) $4.76 = 47a'P_H + 47b'$

  $b' = (4.76 - 47a'P_H)/47$

  $b' = 0.1013 - a'P_H$

Equating (6A) and (7A):

8A) $0.1370 - a'P_L = 0.1013 - a'P_H$

  $0.03574 = a'(P_L - P_H)$

  $a' = 0.03574/(P_L - P_H)$

Subtracting 127*(3A) from 80*(2A):

9A) $127(100.57) - 80(107.01) = 127(a + 80a')P_L +$

    $127(b + 80b') - 80(a + 127a')P_L - 80(b + 127b')$

  $4211.59 = 47a*P_L + 47b$

  $89.6083 = a*P_L + b$

  $b = 89.6083 - a*P_L$

Subtracting 127*(5A) from 80*(4A):

10A) $127(73.69) - 80(78.45) = 127(a + 80a')P_H + 127(b + 80b') - 80(a + 127a')P_H - 80(b + 127b')$

$3082.63 = 47a*P_H + 47b$

$b = 65.5879 - a*P_H$

Combining (9A) and (10A) gives:

11A) $89.6083 - a*P_L = 65.5879 - a*P_H$

$24.0204 = a(P_L - P_H)$

$a = 24.0204/(P_L - P_H)$

Summarizing equations 11A, 8A, 9A, and 6A:

$a = 24.0204/(P_L - P_H)$

$a' = 0.03574/(P_L - P_H)$

$b = 89.6083 - a*P_L$

$b' = 0.1370 - a'P_L$

It is important to note that this is an empirical relationship resulting from the measurements of accelerated stable nuclei (non-radioactive) and non-attenuated fission

fragments. Significant degradation of the fission fragments may affect the accuracy of this method in that the calibration constants would need to be adjusted.

APPENDIX C

MULTIPLE-PARAMETER SYSTEM CONFIGURATION AND SETTINGS

This section briefly describes the system setup and configuration. The various settings will be covered along with descriptions of the components needed to run the assembly.

In order to acquire multiple parameters simultaneously, two computer boards were integrated into the data acquisition computer. These boards were the CIO-SSH16, a 16 channel sample-and-hold (S/H) board, and the CIO-AD16, analog-to-digital (AD) converter. The AD board was installed in the computer internally and connected to the PC bus interface. The S/H board was external and connected to the AD board via a 37 pin cable. A diagram of the S/H board ia shown in Figure C1. A description of the system follows.

Since the S/H board was external to the computer or other physical support, a box was manufactured for protection and to facilitate the addition of BNC connections. This consists of an aluminum box with appropriate holes cut out for the various connections. By using a conducting material, electromagnetic noise would be reduced in the uninsulated wires internal to the box. To power the board, a 5 V power supply was mounted inside the box to supply the 1 A nominal current. A power switch was
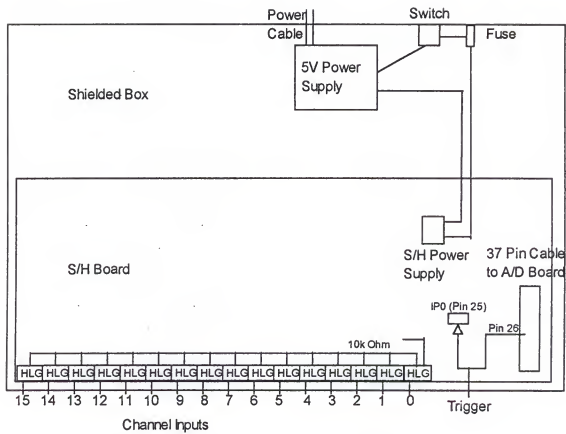
Figure C1: Diagram of S/H board connections.

also included, along with a fuse to prevent a power surge
from burning out the board.

A BNC connection was mounted to the box for each of the
16 channels and for a +5 V trigger source. The board
connections for each terminal consist of a high, low, and
ground screw-pin terminal. Since the signals consist of
0-10 V unipolar (as opposed to -5 V to +5 V bipolar), all of
the low terminals were shorted and connected to the ground
through a 10 kΩ resistor. The high terminals were connected
to the BNC center wire.

The trigger for the board is a +5 V square wave. It is
input to the pin 25 of the 37 pin cable via the #2 screw pin
of the P16 4-pin terminal. The signal is sent to the AD
board where it triggers the S/H chip for channel 0
(contained on the AD board). Channel 0 behaves in a
master/slave manner with the other channels. Therefore,
when channel 0 is acquiring data, channels 1 to 15 are also
acquiring data. The trigger signal connecting channel 0 to
the rest of the channels is sent through pin 26 of the 37
pin cable. The S/H chips acquire data on the downward slope
of the +5 V square wave. After the trigger signal has been
sent to the S/H board and the data acquired, the data is
transferred to the AD board sequentially. It is then
converted to a digital signal and saved. Between the
trigger signal on pin 25 and the return signal on pin 26,
there was a long delay. Since it would not have been
possible to delay all the signals to coincide with the

trigger, an alternate system was set up. The cable wire for pin 26 was cut between the AD and S/H board. The initial trigger signal was then split and sent to the AD board via pin 25 and the S/H board via the open end of pin 26. The signal to the AD board through pin 25 would trigger a delayed channel 0 (which is empty) but the return triggering signal would be prevented from reaching the S/H board. In coincidence with the signal to the AD board, a trigger signal is also sent to the S/H board through the cut pin 26. Therefore, channels 1 to 15 would have been triggered and would be holding the data. The data is transferred after channel 0 has acquired, and digitized by the AD board. This procedure is shown in the Figure C2.

The AD board primarily imports the analog data from the S/H board, digitizes it, and saves it. Since each of the channels of data pass through 1 A/D chip, the channels are imported sequentially from the S/H board. The operation of the board is mainly software controlled. However the gain, range, number of channels, and base address are all set with dip switches. The settings used are 1, 0 to 10 V unipolar, 16 channels, and 300 Hexadecimal respectively.
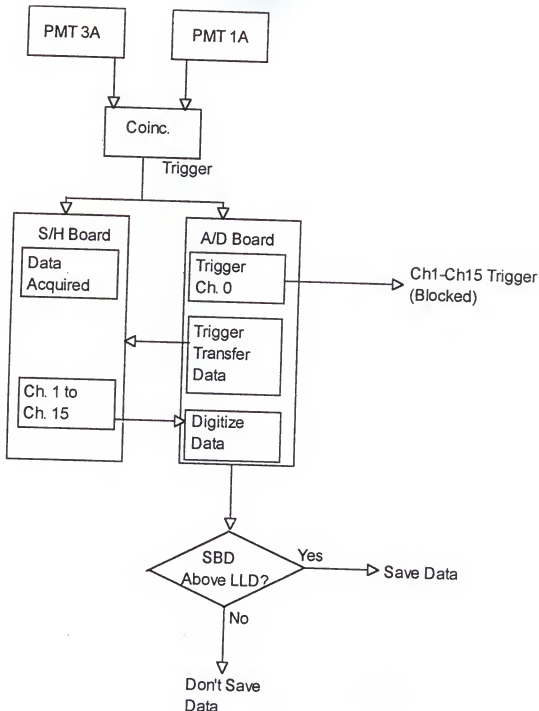
Figure C2: Flow chart of modified triggering system for the
multiple-parameter data acquisition system.

Calibration of the Boards

Sample-and-Hold Board

Since the primary amplifier is on the A/D board, the
only calibration that can be done on the S/H board is the
offset calibration. This can be accomplished in two ways.
In the first method, all three inputs of each channel (high,
low, and ground) are shorted. Then the SSHCAL.EXE program
is run and the offset is adjusted until a reading of 2047
appears. This is repeated for each channel. The offset is
adjusted by turning the screw on the blue trimpot. A
plastic screwdriver is supplied for this purpose. This
method involves removal, or at least an adjustment, of the
three connections for each channel. The following method
requires only a calibrated voltage source and a BNC
connection.

The second method involves connecting a calibrated
voltage signal to the BNC input for each channel. By
applying two calibrated voltages (0 V and a higher signal)
the offset can be adjusted (with the 0 V signal) and the
gain can be verified. After the 0 V signal is connected to
the BNC input, CAL16.EXE is run. The offset is adjusted
until the signal flickers between 0 and 1. This is repeated
for each channel. Then the process is repeated with a
calibrated voltage signal. If the appropriate signal is
registered, then the gain is verified.

A/D Board Calibration

    If the S/H board yielded appropriate zero and gain
signals, no adjustment is necessary on the A/D board.
However, if the A/D board must be calibrated, the procedure
is as follows.

    First, the computer is opened up to allow access to the
A/D board. While running the CAL16.EXE program, connect a
1.22 mV signal (for the 0 - 10 V setup) to pin 37 and ground
pin 19 of the 37 pin cable. Adjust the offset trimpot on
the A/D board until the signal flickers between 0 and 1.
For the gain adjustment, repeat with a calibrated voltage
(close to 10 V) connected to pin 37. Adjust the A/D full
scale trimpot until the appropriate signal results.

Multiple Thin Film System Settings

    For reference, the system diagram is shown again in
Figure C3. The system can be operated with or without
films. If operated without films, the triggering signal
must be changed from the luminescence signals to the SBD
signal. This entails changing several settings. First, the
settings common for both systems will be given. Then the
values that differ will be given for each system.

    The common settings are given below:

   PM High Voltages: -2600 V

    SBD Voltage: 34 V
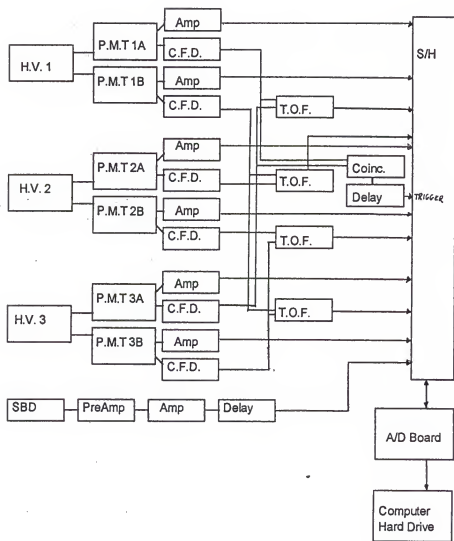
Figure C3: Diagram for multiple scintillator film system

ORTEC 572 AMP's (for PM signals): Gain = 1500

               Delay off

               Shaping Time = 3 μs

    CFD's: 1.3 to 2.0

    TAC's: 0 - 50 ns

    Fast Coincidence: 110 ns

For a luminescence triggered system, typically two luminescence signals are used to trigger fast-coincidence signal. Usually, signals 1A and 3A were used. However, if only one film is in place, then both signals from that film would be used.

    Luminescence triggered system:

    572 AMP (for SBD signal): Gain = 100

        Shaping Time = 2 μs

        Delay off

    427 Delay AMP (SBD signal delay): Delay = 0.25 μs

    427 Delay AMP (trigger delay): Delay = 1.0 μs

For an SBD triggered system, a trigger signal must be sent from the bipolar output of the SBD 572 AMP into a CFD. With a setting of 2.0 to 3.0, any fission fragment should easily trigger the CFD (software check should keep alpha particles from triggering the system). The CFD output is sent to the Fast Coincidence unit. The settings are as follows:

```
572 AMP (for SBD signal): Gain = 100
      Shaping Time = 2 μs
      Delay on
427 Delay AMP (SBD signal delay): Delay = 3.0 μs
427 Delay AMP (trigger delay): Delay = 0.0 μs
```

With the system triggering off of the SBD signal, the timing for the luminescence signals will not coincide with the triggering signal. Therefore, no luminescence signals can be acquired.

BIBLIOGRAPHY

1.   Knoll, G. 1979. Radiation Detection and Measurement.
New York: John Wiley and Sons

3.   Appario, K. 1975. Composition of Cosmic Radiation. New
York: Gordon and Breach Science Publishers

4.   Durrani, S. 1987. Solid State Nuclear Track Detection:
Principles, Methods, and Applications. New York: Pergamon
Press

5.   Bethge, K. 1978. Experimental Methods in Heavy Ion
Physics. Heidelberg, Germany: Springer Verlag

6.   Silicon Charged Particle Radiation Detector Instruction
Manual, EGG ORTEC Manual, 1995

7.   Bromley, D. A. 1985. Treatise on Heavy Ion Science. New
York, NY: Plenum Press

8.   Muga, L., Griffith, G. 1973. Nuclear Instruments and
Methods. 109: 289

9.   Muga, M. L. 1971. Nuclear Instruments and Methods. 95:
349

10. Muga, M. L. 1974. Nuclear Instruments and Methods. 124:
541

11. Batsch, T., Moszynski, M. 1975. Nuclear Instruments and
Methods. 123: 341

12. Muga, M. L., Clem, A., Griffith, G., Plendl, H. S.,
Eaker, R., Holub, R. 1974. Nuclear Instruments and Methods.
119: 255

13. Nicovich, J. M., Clem, A., Muga, L., Plendl, H. 1978.
Nuclear Instruments and Methods. 157: 93

14. Muga, L., Diksic, M. 1974. Nuclear Instruments and
Methods. 122: 553

15. Batsch, T., Moszynski, M. 1974. Nuclear Instruments and
Methods. 125: 231

16. Muga, L., Griffith, G. 1973. Physical Review B. 8: 4069

17. Muga, L. 1972. Nuclear Instruments and Methods. 105: 61

18. Muga, L., Griffith, G., Schmitt, H. W., Taylor, H. E.
1973. Nuclear Instruments and Methods. 111: 581 585

202

19. Muga, L., Griffith, G. 1973. Physical Review B. 9: 3639

20. Muga, L., Burnsed, D. 1975. Review of Scientific Instrumentation. 47: 924

21. Batra, R. K., Shotter, A. C. 1974. Nuclear Instruments and Methods. 124: 101

22. Gelbke, C. K., Hildenbrand, K. D., Bock, R. 1971. Nuclear Instruments and Methods. 95: 397

23. Liden, F., Nyberg, J., Johnson, A., Kerek, A. 1987. Nuclear Instruments and Methods in Physics Research. A253: 305

24. McDonald, W. J., Kilvington, A. I., Batty, C. J., Weil, J. L. 1973. Nuclear Instruments and Methods. 115: 185

25. Milosevich, Z. 1991. University of Florida, PhD Dissertation, Gainesville, Fl.

26. Muga, L., Burnsed, D., Steeger, D. 1972. Nuclear Instruments and Methods. 104: 605

27. Gorbachev, V. M. 1980. Nuclear Reactions in Heavy Elements: A Data Handbook. NY, NY: Pergamon Press

28. Flynn, K. F., Gindler, J. E., Glendenin, L. E. 1975. Journal of Inorganic Nuclear Chemistry. 37: 881

29. Nervik, W. E. 1960. Physical Review. 119: 1685

30. Harbour, R. M., Eichor, M., Troutner, D. E. 1971. Radiochim. Acta. 15: 146

31. Skovorodkin, N. V., al., e. 1973. Atom. Energ. 34: 365

32. Wahl, A. C. 1988. Atomic Data and Nuclear Data Tables. 39: 1

33. Srinivasan, B., Alexander, E. C., Manuel, O. K., Troutner, D. E. 1969. Physical Review. 179: 1166

34. Scintillators for the Physical Sciences, Nuclear Enterprises Manual, Reading, England.

35. RCA Photomultipliers Photocathode Spectral Response Characteristics

36. Schmitt, H. W., Kiker, W. E., Williams, C. W. 1964. Physical Review. 137: 837

37. Wilkins, B., Fluss, M., Kaufman, S., Gross, C., Steinberg, E. 1970. Nuclear Instruments and Methods. 92: 381

38. Finch, E., Asghar, M., Forte, M. 1979. Nuclear Instruments and Methods. 163: 467

39. Finch, E., Asghar, M. e. a. 1977. Nuclear Instruments and Methods. 142: 539

40. Moulton, J., Stephenson, J., Schmitt, R., Wozniak, G. 1978. Nuclear Instruments and Methods. 157: 325

41. Silicon Charged Particle Radiation Detector Instruction Manual, EGG ORTEC, Oak Ridge, TN, 1995

42. Herrmann, R., Cocke, C., Ullrich, J., Hagmann, S., Stoeckli, M., Schmidt-Boecking. 1994. Physical Review A. 50: 1435

43. Nikolaev, V., Dmitriev, I. 1968. Physics Letters. 28A: 277

44. To, R., D. 1979. Nuclear Instruments and Methods. 160: 461

45. Shima, K., Kuno, N., Yamanouchi, M. 1989. Physical Review A. 40: 3357

46. Moak, C., Lutz, H., Bridwell, L., Northcliffe, L., Datz, S. 1967. Physical Review Letters. 18: 41

47. Clark, R., Grant, I., King, R., Eastham, D., Joy, T. 1975. Nuclear Instruments and Methods. 133: 17

48. Brunelle, A., Della-Negra, S., Depauw, J., Joret, H., Le Beyec, Y. 1989. Nuclear Instruments and Methods in Physics Research. B43: 484

49. Rao, M., Biswas, D., Choudhury, R. 1990. Nuclear Instruments and Methods in Physics Research. B51: 102

50. Shima, K., Kuno, N., Kakita, T., Yamanouchi, M. 1988. Physical Review A. 39: 4316

51. Biswas, D., Rao, M., Choudhury, R. 1990. Nuclear Instruments and Methods in Physics Research. B53: 251

52. Bimbot, R. 1992. Nuclear Instruments and Methods in Physics Research. B69: 1

53. Shima, K., Mikumo, T., Tawara, H. 1986. Atomic Data and Nuclear Data Tables. 34: 357

54. Lennard, W., Phillips, D., Walker, D. 1981. Nuclear Instruments and Methods. 179: 413

55. Lennard, W., Jackman, T., Phillips, D. 1981. Physical Review A. 24: 2809

56. Shima, K. 1985. Nuclear Instruments and Methods. B2: 45

57. Knystautas, E., Jomphe, M. 1981. Physical Review A. 23

58. Knystautas, E. 1979. IEEE Transactions of Nuclear Science. 26: 1470

59. Baron, E., Delauney, B. 1975. Physical Review A. 12: 40

60. Ziegler, J. F. 1990. TRIM-90: The TRansport of Ions in Matter, Manual

61. Thwaites, D. 1992. Nuclear Intruments and Methods in Physics Research. B69: 53

BIOGRAPHICAL SKETCH

David Miko was born on August 10, 1966. He was raised in Severna Park, Maryland, a town between Baltimore and Annapolis. He graduated from Severna Park High School and proceeded to Virginia Polytechnic Institute. He received a bachelor degree in electrical engineering from Virginia Tech in 1988. He then attended the University of Florida. At UF, he earned his master's degree in nuclear engineering in 1991. Since then, he has alternated working on a doctorate in nuclear engineering and working at Los Alamos National Laboratory. He has delayed his graduation several years while waiting for the Gators to win their first football national championship.

After graduation, he hopes to perfect "cold fusion" and build the next generation of nuclear reactors in the United States.

I certify that I have read this study and that in my opinion it conforms to acceptable standards of scholarly presentation and is fully adequate, in scope and quality, as a dissertation for the degree of Doctor of Philosophy.
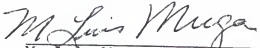
M. Luis Muga, Chairman
Professor of Chemistry

I certify that I have read this study and that in my opinion it conforms to acceptable standards of scholarly presentation and is fully adequate, in scope and quality, as a dissertation for the degree of Doctor of Philosophy.
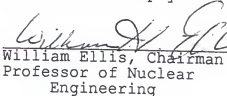
William Ellis, Chairman
Professor of Nuclear
Engineering

I certify that I have read this study and that in my opinion it conforms to acceptable standards of scholarly presentation and is fully adequate, in scope and quality, as a dissertation for the degree of Doctor of Philosophy.
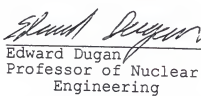
Edward Dugan
Professor of Nuclear
Engineering

I certify that I have read this study and that in my opinion it conforms to acceptable standards of scholarly presentation and is fully adequate, in scope and quality, as a dissertation for the degree of Doctor of Philosophy.
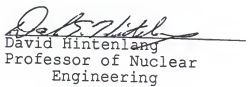
David Hintenlang
Professor of Nuclear
Engineering

I certify that I have read this study and that in my opinion it conforms to acceptable standards of scholarly presentation and is fully adequate, in scope and quality, as a dissertation for the degree of Doctor of Philosophy.
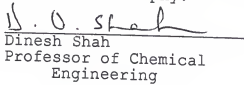
Dinesh Shah
Professor of Chemical
Engineering

I certify that I have read this study and that in my opinion it conforms to acceptable standards of scholarly presentation and is fully adequate, in scope and quality, as a dissertation for the degree of Doctor of Philosophy.

Dinesh Shah
Professor of Chemical
Engineering

This dissertation was submitted to the Graduate Faculty of the College of Engineering and to the Graduate School and was accepted as partial fulfillment of the requirements for the degree of Doctor of Philosophy.

August, 1997

Winfred M. Phillips
Dean, College of
Engineering

Karen A. Holbrook
Dean, Graduate School